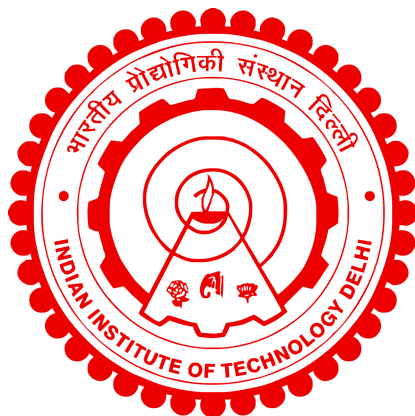


A STUDY ON THE DYNAMICS AND SELF-ASSEMBLY OF ANISOTROPIC PARTICLES

VIKKI ANAND VARMA



DEPARTMENT OF PHYSICS

INDIAN INSTITUTE OF TECHNOLOGY DELHI

FEBRUARY 2024

A STUDY ON THE DYNAMICS AND SELF-ASSEMBLY OF ANISOTROPIC PARTICLES

by

VIKKI ANAND VARMA

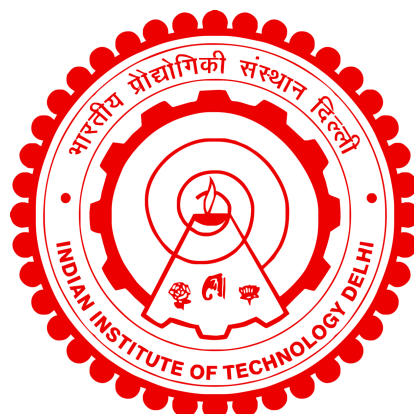
Department of Physics

Submitted

in fulfillment of the requirements of the degree of

Doctor of Philosophy

to the



INDIAN INSTITUTE OF TECHNOLOGY DELHI

FEBRUARY 2024

Dedicated to my uncle and Gurudev Shree Harihar

Certificate

This is to certify that the thesis entitled "**A STUDY ON THE DYNAMICS AND SELF-ASSEMBLY OF ANISOTROPIC PARTICLES**", submitted by **VIKKI ANAND VARMA**, Entry No. **2018PHZ8362** to the Indian Institute of Technology Delhi, for the award of the degree of **Doctor of Philosophy** in **PHYSICS**, is a record of the original, bonafide research work carried out by him under our supervision and guidance. The thesis has reached the standards fulfilling the requirements of the regulations related to the award of the degree.

The results contained in this thesis have not been submitted in part or in full to any other University or Institute for the award of any degree or diploma to the best of our knowledge.

Prof. Sujin B. Babu
Department of Physics,
Indian Institute of Technology Delhi

Acknowledgements

I want to thank my supervisor **Prof. Sujin B. Babu** for his guidance and support. I would also like to thank my mentors **Dr. Isha Malhotra**, and **Dr. Mohd Yasir Khan**. I am thankful to my beloved seniors **Dr. Shahrukh Salim**, **Dr. Vikas Mishra** and **Dr. Harsh Gupta** for consistently supporting me and teaching me philosophy and physics during our badminton games. I am thankful to the members of my SRC committee **Prof. Pradipta Ghosh**, **Prof. Varsha Banerjee**, and **Prof. Vikram Singh**. I would also like to acknowledge my seniors, Yatin Pitkar and Sooryansh Asthana for consistently supporting and caring me. And Simmie, for helping me in and out of the lab. I am thankful to my juniors for their love and support, especially Kritika, Jaskaran, Mintu, and Roshan. I would also like to thank my room partners and friends, Dr. Vimarsh Awasthi, Divyanshu Vikram Singh, Ajay Kumar, Fauzia Khan and Shubham Tiwari. In the end, I would like to thank my robotic friend Om Shankar.

Vikki Anand Varma

Abstract

The thesis primarily focuses on the different aspects of dynamical and structural properties arising mainly due to the shape-anisotropy of the particles within a colloidal system. We studied the diffusivity of the particles in a one-component system. The friction effect dominates the diffusivity of spheroids at lower volume fractions. While at higher volume fractions, it depends upon structural properties like phases and random packing. In the two-component system, the diffusivity of the spheroids has been observed to increase in the presence of spheres as the secondary component. The nematic phases have been observed destroying in the presence of spheres, leading to a fraction of spheres vs volume-fraction phase diagram. Later in the work, we studied the self-assembly of spheroids with directional and limited bonding using patches. We found shape anisotropy working along with the directional bonding, forming a phase-rich system. Within a particular range of anisotropy, the system could lead to the formation of complex structures like a free-standing monolayer. In the later part, we used annular patches to study the cause of disordering arising in constructing a spherical shell. We found that both icosahedral symmetry and disordered shells show the same potential energy. Therefore, due to the lack of the deriving force in an axially symmetric potential, we found the absence of icosahedral symmetry despite the shell's spherical shape. Flexibility in structural rearrangement plays an essential role in forming close spherical shells via the self-assembly approach. However, the shells are ideal for drug delivery due to their large enough size and spherical shape to trap the particles inside.

Contents

Certificate	I
Acknowledgements	II
Abstract	III
Contents	III
List of Figures	IX
Abbreviations	XVII
Symbols	XIX
1 Introduction	1
1.1 Outline of the thesis	7
I Dynamics and phase-behavior in the system of hard-spheroidal colloids	9
2 Brownian motion and diffusion-limited cluster aggregation in colloidal suspension of hard spheroids	11
2.1 Diffusivity and phases in the system of shape-anisotropy hard particles	14
2.1.1 Diffusivity in the presence of obstacles and the effect of confinement	15
2.2 Kinetics of nucleation and aggregation	16
2.2.1 Kinetics of aggregation in a DLCA system of colloids	18
2.3 DLCA system of anisotropic particles	20
2.3.1 Closed system of spherically symmetric structures in the living organism and other non-living colloidal systems.	22

2.4	Anisotropic potential models (Kern-Frenkel potential)	23
3	Simulation methods to calculate dynamics, kinetics, structures, and phase-diagram	25
3.1	Brownian motion: Wiener process and scaling	26
3.1.1	Dynamics and scaling for spheroidal colloids (shape-anisotropic hard-core): With stick boundary condition	29
3.2	Simulation technique: Brownian Cluster Dynamics (NVT)	32
3.2.1	Movement steps	33
3.2.2	Implementation of Rotational movement	36
3.2.3	Cell division of simulation box and periodic boundary condition	38
3.2.4	Interaction between the particles contained within the cell, connected through the periodic boundary condition	39
3.2.5	Spheroids and overlap condition: Ellipsoid contact function . .	39
3.2.6	An efficient method to calculate the overlap of two spheroids .	42
3.3	NPT Simulation	47
3.4	Variable shape simulation method	49
3.4.1	Re-scaling the position of the particles in a floppy box, following the volume movement	51
3.4.2	Lattice reduction technique: Avoiding extreme shape distortion of the simulation box	52
3.5	Floppy simulation method	52
3.6	Prediction of the crystal structures	53
3.7	Calculating cluster size distribution	54
3.7.1	Semi-grand canonical monte-carlo simulation with parallel tempering and umbrella sampling	54
3.7.2	Umbrella sampling	56
3.7.3	Parallel tempering	56
3.8	Calculation of phase-diagram using thermodynamic integration	57
3.8.1	Equation of state for spheroidal colloids	58
3.8.2	Free energy calculation for the fluid regime	59
3.8.3	Free energy of the cluster gas using SGMC	59
3.8.4	Plotting Chemical potential vs pressure for liquid, at constant T	61
3.8.5	Free energy of solid using Einstein crystal method	62
3.8.6	Plotting Chemical potential vs pressure for solid, at constant T	63
3.8.7	Thermodynamic integration using <i>NPT</i> simulation for a one component system	64
4	Enhancement in the diffusivity of Brownian spheroids in the presence of spheres	65
4.1	Introduction	67
4.2	Simulation technique	71

4.3	Results	72
4.3.1	Dynamics of one component spheroids	72
4.3.2	Isotropic-nematic transition in spheroids -spheres binary mixture	78
4.3.3	Dynamics in a two-component system of spheroid-sphere	83
4.4	Discussion and Conclusion	90
 II Kinetics of growth and structural properties of spheroidal-colloids interacting through anisotropic-attractive-potential		
93		
5	Kinetics and phases shown by reversible-aggregation of patchy spheroids	95
5.1	Kinetics in the reversible aggregation of spheroids	95
5.2	Exploring validity of Noro-Frenkel generalized law of corresponding states for anisotropic pair-potential with spheroidal hard-core	96
6	Self-assembly of patchy anisotropic particle forming free-standing monolayer film	101
6.1	Introduction	103
6.2	Simulation method	105
6.2.1	Brownian Cluster Dynamics	106
6.2.2	NPT simulation in a floppy box	107
6.3	Results	108
6.3.1	Structural properties	108
6.3.2	Phase diagram	115
6.4	Discussion and Conclusion	120
7	Breaking the size constraint for nanocages using annular patchy particles	123
7.1	Introduction	125
7.2	Model and Simulation method	127
7.3	Results	129
7.3.1	Structural properties	129
7.3.2	Kinetics of the shell growth	136
7.3.3	Size, Symmetry, and yield of the closed structures	139
7.4	GEMC Simulation in a closed system	147
7.5	Discussion and Conclusion	149
8	Conclusion and future scope	151
8.1	Conclusions	151
8.2	Future scope	153

References	155
-------------------	------------

A List of Publications	187
-------------------------------	------------

List of Figures

1.1	Aggregation of the butter content, observable as a shiny wrinkled layer formed over the surface of cooling hot milk tea.	2
1.2	Schematic of layers in the biological membrane. Image source - Wikipedia	3
1.3	(a–c) Cryo-TEM pictures of parallelogram nanosheets (d) flake crystals (e) lamellar structures, (f–i) Pictures of multilamellar-tubular structures. Image source - Nature publication	5
1.4	Shape anisotropy in interaction as well as hardcore leading to the self-assembly of (a)Spherical shells, (b)films, and (c) Tubular structures.	6
3.1	Brownian motion is shown with different Δt such that $\Delta t_2 = 10 \Delta t_1$. Over a long time period ($t \gg \Delta t$) motion can be observed to be Brownian for both scaled time steps Δt_1 and Δt_2	26
3.2	The relation between applied rotation s'_R to the gained arc length a_R is shown. The slope is equivalent to the $\sqrt{2/3}$ for the small rotations (red line), while for larger rotations, the slope deviates.	35
3.3	L_2 is shown for the two different systems of prolate spheroids ($p = 2$) at $\phi = 0.4$. The red line represents the system with the axis selection in 3D and the black line in the X-Y plane of the rigid body (2D).	36
3.4	ECF shown for different conditions. The blue line shows the corresponding points with the variation of $S(\lambda)$ with λ where $\lambda \in [0, 1]$. Maximum of $S(\lambda)$, corresponds to the point which lies closest to the surface of spheroids, shown with the tip of the arrow.	42
3.5	Rectangular boxes enclosing the particles. Particles can overlap only when the rectangular boxes overlap.	43
4.1	The effect of step size (S_T) of the center of mass of ER with D_T^{\parallel}/D_T^o (circles), D_T^{\perp}/D_T^o (triangles) and the resultant D_T/D_T^o (squares) are shown for ER with $p = 4.0$ at $\phi = 0.5$. The solid lines are fit to the points. The points can be seen converging to a particular value, given by $D_T^{\parallel}/D_T^o \approx 0.46$, $D_T^{\perp}/D_T^o \approx 0.075$, and $D_T^e/D_T^o \approx 0.18$	74
4.2	The MSD of the center of mass of the ER $\langle R^2 \rangle/d^2$ (square) is plotted as a function of t_{Phy}/t_o calculated with $S_T = 0.005$ for $p = 4$ and at $\phi = 0.50$. The MSD is resolved into the parallel (circle) and perpendicular (red points) direction of the director. They converge to a slope of unity as shown by the solid lines.	75

4.3	(a) D_T^{\parallel}/D_T^o (circles), D_T^{\perp}/D_T^o (triangle) and D_T/D_T^o (square) are shown for the different values of p at $\phi = 0.002$. Solid lines represent the analytical diffusion coefficient calculated for the single particle with a constant volume of $\pi/6$ for different values of p . (b) The change in D_R/D_R^o with respect to p is shown for the present work (circle), and analytical calculation from Perrin's factor is shown with solid lines.	76
4.4	Iso-diffusivity lines are shown for different ϕ as a function of the aspect ratio p , where the solid lines and dotted line represent translational and rotational diffusion, respectively. The diffusion coefficients are as indicated in the figure.	77
4.5	Variation in the isotropic-nematic coexistence density ϕ with respect to the fraction of sphere $f^{1.0}$, present in the binary mixture of sphere and prolate $p = 4$ system. The upper and lower tick on the error bar indicate the nematic and isotropic phases, respectively, confirmed by nematic-order-parameter calculation in the simulation.	79
4.6	$g(\hat{n}_I \cdot \hat{n})$ is shown as a function of $\hat{n}_I \cdot \hat{n}$ which is the cosine of the angle made by the director with the symmetry axis of the prolate ellipsoids $p = 4$ at different fractions of spheres as mentioned in the figure.	80
4.7	$g_{P_2}(r)$ is shown as a function of the distance r/d for binary system of spheres and prolate $p = 4.0$, at $\phi = 0.50$, with fraction of sphere as indicated in the figure. The inset shows the $g_2(r)$ calculation for the same configuration as indicated in the figure.	81
4.8	Snapshot of the binary spheroidal-sphere system with increasing fraction of spherical particle from left to right for $\phi = 0.5$, $p = 4.0$ and at (a) $f^{1.0} = 0.0$, (b) $f^{1.0} = 0.12$, (c) $f^{1.0} = 0.27$. The ordered reason (the bounding box) can be seen decreasing with increasing the number of spheres in the system.	83
4.9	(a) D_T/D_T^o shown for the binary system containing particles with sphere $p = 1.0$, prolate $p = 4.0$. The solid symbols represent the diffusion coefficient of only the prolate particles in the binary mixture. The short dashed line represents the diffusion coefficients of only the spherical particles. The fraction of spherical particles is indicated in the figure. (b) D_T/D_T^o is plotted for an oblate $p = 0.25$ and sphere mixture. Where lines show the diffusion coefficient for $p = 0.25$ (solid) and for spheres (short dash), simulated with the fraction of sphere as indicated in the figure.	84
4.10	(a) D_R/D_R^o is shown for the binary system containing both sphere and prolate $p = 4$ particles at different ϕ . The fractions of the sphere are given in the figure. (b) $D_R^{0.25}/D_R^o$ is shown for the binary system containing both sphere and oblate $p = 0.25$ particles at different ϕ . The fractions of the sphere are given in the figure.	85

4.11 (a) D_T^e/D_T^o are shown for the spheres (dashed line) and prolate particle (solid line) with aspect ratio 2.0 at different ϕ in the binary mixture. The fraction of the sphere in the system is shown in the figure. (b) D_R^e/D_R^o is shown for the ellipsoidal particles $p = 2$ in the binary mixture with the fraction of sphere as indicated in the figure.	88
4.12 (a) Snap shot of the monomeric prolate particle with $p = 2$ at $\phi = 0.5$ as obtained from the simulation. (b) The snapshot of a binary mixture of spheres and prolates $p = 2$ with the fraction of sphere $f^{1.0} = 0.40$. In both systems, we do not observe nematic transition.	89
5.1 (a) B_2/B_2^{HS} is shown for different patch angle ω , for a system of prolate spheroidal particles decorated with two patches along the axis of symmetry and aspect ratio $p = 1$ (triangle), 2 (square) and 4(circle) calculated at $k_B T/u_o = 0.114$. (b) B_2/B_2^{HS} is shown for the different shapes of the prolate particles defined by the aspect ratio p of the particle's semi-minor and the major axis length, calculated at different $k_B T/u_o = 0.114$ (lower triangle), 0.123 (square), and 0.144 (circle). Where the patches have constant $\omega = 25^\circ$. Grey circle points show the B_2/B_2^{HS} of the repulsive hardcore part of the particle at different p .	98
5.2 B_2/B_2^{HS} is shown for different $k_B T/u_o$, calculated at $p = 1.5$, $\omega = 25^\circ$ and two different patch ranges $\epsilon = 0.1$ (square) and 0.2(circle). Here, the shape of the particles has been kept similar.	98
5.3 HCP arrangement of spheroids with $p = 1.5$, shown for the two different patch ranges (where patches are attached at the two ends of the particle along the symmetry axis of the particle) (a) $\epsilon = 0.1$, at $k_B T/u_o = 0.1075$ and (cyan spheroids) (b) $\epsilon = 0.2$, at $k_B T/u_o = 0.117$ (green spheroids), as predicted by variable shape simulation methods.	99
6.1 Three bonded ellipsoidal particles are shown. The arrows represent the orientation vectors (\hat{n}), and the white conic section represents the patches.	105
6.2 Unit cell (top row) of different crystal structures as predicted by the floppy simulation and corresponding bulk system (bottom row), with $p = 1.5$ and $\cos(\omega) = 0.9$ (a) Type I crystal (b) Type II crystal and (c) monolayer. (d) Corresponds to the Type-I crystal, at $k_B T/u_o = 0.15$ and $p\sigma^3/k_B T = 0.5$. (e) Type-II crystal at $k_B T/u_o = 0.2$ and $p\sigma^3/k_B T = 10$. (f) The monolayer at $k_B T/u_o = 0.2$ and $p\sigma^3/k_B T = 6$. The corresponding top view of the crystal is shown (g) Type I, (h) Type II, and (i) monolayer. Patches have been shown with white color cones.	109

6.3	The structures predicted by floppy simulation, obtained in the NVT simulation for the system with $p = 1.5$ and $\cos(\omega) = 0.9$. From left to right. Red corresponds to the Type-I crystal, at $k_B T/u_o = 0.15$ and $\phi = 0.55$. Yellow: Type-II crystal at $k_B T/u_o = 0.20$ and $\phi = 0.55$. While blue is the monolayer at $k_B T/u_o = 0.114$ and $\phi = 0.06$. Patches have been shown with white color cones along the \hat{n} of spheroids.	110
6.4	Average bonded nearest neighbor; ZPI shown as a function of time on the left, and the particle fraction with the given number of bonded neighbors, as indicated in the figure, is shown on the right. (a), (b) Type-I crystal at $k_B T/u_o = 0.15$ and $\phi = 0.55$. (c), (d) Type-II crystal at $k_B T/u_o = 0.20$ and $\phi = 0.55$. (e), (f) Monolayer at $k_B T/u_o = 0.114$ and $\phi = 0.06$	112
6.5	Pair correlation function $G(r)$ corresponding to the <i>NVT</i> ensemble (solid line) is compared with the structure predicted by the floppy simulation (dotted line). (a) Type I crystal at $k_B T/u_o = 0.15$ and $\phi = 0.55$ (b) Type-II crystal at $k_B T/u_o = 0.20$ and $\phi = 0.55$. (c) Monolayer at $k_B T/u_o = 0.20$ and $\phi = 0.55$	113
6.6	\bar{q}_6 and \bar{q}_4 have been shown for different structures, indicating the presence of ordered phases obtained in <i>NVT</i> ensembles.	115
6.7	Equilibrium cluster distribution is shown for <i>SGMC</i> calculation (square points) done at $\phi = 0.01$ and temperature $k_B T/u_o = 0.16$ (red squares), 0.123 (blue squares) and 0.114 (black squares) and compared with the <i>NVT</i> (solid lines).	116
6.8	$p - \mu$ curve shown for different phases at $k_B T/u_o = 0.22$. p have been expressed in the unit of $k_B T/d^3$, while μ in the unit of $k_B T$. (a) The intersection point of the two lines shows the coexistence of Type I crystal and fluid. (b) The intersecting line shows the phase coexistence of Type I, Type II, and monolayer crystals.	117
6.9	(a) $p-T$ phase-diagram exhibiting the location of various phases have been shown for the system of spheroids with $p = 1.5$ and $\cos(\omega) = 0.9$. p have been expressed in the unit of $k_B T/d^3$, while $k_B T$ in the unit of u_o . The blue solid line represents the coexistence point among the various phases. (b) $\rho - T$ phase-diagram showing the location of various phases for the system of spheroids with $p = 1.5$ and $\cos(\omega) = 0.9$. ρ have been expressed in the unit of $1/d^3$. The blue solid line represents the coexistence point.	119

- 7.1 (a) Subunits with oblate hardcore (gray color), along with annular patches shown as (black) ring-like structure, and the arrows passing through the symmetry axis of the subunits represent the patch vector. All the subunits represented in grey color have less than 4 bonded neighbors. While red subunits have bonded neighbors < 5 . Cyan and yellow subunits have 5 and 6 bonded neighbors, respectively. (b) Oblate hardcore with annular patch forming mono-dispersed structures with icosahedral symmetry, shown at $k_B T/u_o = 0.115 \Omega^\circ = 60^\circ$, $\epsilon = 0.25$ and $\Delta\omega^\circ = 3^\circ$. Fully evolved closed shell is shown at $k_B T/u = 0.115 \Omega^\circ = 74^\circ$, $\epsilon = 0.25$ and $\Delta\omega^\circ = 3^\circ$, with (c) oblate ellipsoid, (d) prolate ellipsoid and (e) spherical subunits. In these systems, the small disordered clusters (monomers, dimers, trimers) are removed for better visualization. (f) Clusters formed for spherical subunit at, $k_B T/u = 0.137$ for $\Omega^\circ = 79.6^\circ$, $\epsilon = 0.1$ and $\Delta\omega^\circ = 4.5^\circ$, where we can also observe voids at the center of the pentagonally arranged spherical subunits. (g) Very large shells of spherical subunits formed at $k_B T/u = 0.142$ for $\Omega^\circ = 82^\circ$, $\epsilon = 0.4$ and $\Delta\omega^\circ = 3^\circ$ 130

7.2 (a) Different region identified in the $k_B T/u_o - \phi$ plane, obtained in *NVT* ensemble for spherical ($p = 1$) shaped subunits with patch angle $\Omega^\circ = 74$, width $\Delta\omega^\circ = 4.5$ and range $\epsilon = 0.25$. Here **G** (black lower triangle) represents the region having disordered clusters ranging from small (monomers, dimers, etc) to large size clusters. **C** (red circle) represents the region having closed shells coexisting with the small-size clusters (monomers, dimers, trimers). **COD** (pink square) region is dominated by the presence of open shells along with closed shells and disordered clusters. **P** (blue square) region represents percolated clusters. (b) Snapshot for the system at $\phi = 0.4$ and $k_B T/u = 0.18$ (cyan pentagons), where the pink cluster represents a close shell connected through periodic boundary conditions, blue clusters are percolated partially grown shells, green clusters is partially grown shell which is not part of the percolated cluster, and white clusters are the disordered clusters, which are either freely diffusing or trapped inside the shell. (c) A percolated structure of partially grown shells is shown at $\phi = 0.08$ and $k_B T/u = 0.12$ 132

7.3 Probability of distribution of bonds of a subunit $P(n_b)$ and the dashed dotted line are the average bonded neighbors per particles $\langle n_b \rangle$ are shown for the regions (a) **G** at $k_B T/u = 0.24$, $\phi = 0.4$ with $\langle n_b \rangle = 1.2$, (b) **C** at $k_B T/u = 0.16$, $\phi = 0.08$ with $\langle n_b \rangle = 4.7$, (c) **COD** at $k_B T/u = 0.14$, $\phi = 0.08$ with $\langle n_b \rangle = 4.8$, (d) **P** at $k_B T/u = 0.12$, $\phi = 0.08$ with $\langle n_b \rangle = 4.7$ 133

7.6	(a) Radial distribution function $G(r)$ calculated over a closed shell, shown for $\Omega^\circ = 74.12^\circ$ (black), 79.6° (red), 82° (blue) having the same $\Delta\omega^\circ = 3^\circ$ and $\epsilon = 0.4$, corresponding to the different number of subunits for a closed shell as shown in the figure. (b) $G(\theta^\circ)$ the angular distribution of the bonded neighbors for a closed shell with different numbers of subunits as indicated. (c) The distribution of bonded neighbors $P(n_b)$ is calculated over only the subunits that are part of the shell. (d) Subunit number variation in a cluster $\Delta c_s = c_s - \bar{c}_s $ for different Ω° values, where the average number of subunits in a cluster c_s is shown in the figure. (e) Steinhardt order parameter is shown for the shell with the different number of subunits as indicated in the figure. (f) Variation in the yield (color coded) of perfectly closed shell, at different $k_B T/u_0$ for varying Ω° is shown at $\phi = 0.06$, $\epsilon = 0.1$ and $\Delta\omega^\circ = 3^\circ$	140
7.7	(a) $P(r_S)$ is shown for different cluster sizes (obtained by different Ω° value, while keeping the rest of the potential parameters as the same), measured from the center of mass (dotted line) and center of curvature of the shell (solid line). The position of the peak represents the radius of the shell, and the width shows the deviation from the spherical shape. (b) $P(r_S)$ is shown for different $\Delta\omega^\circ$ (calculated at $\Omega^\circ = 74^\circ$ and $\epsilon = 0.25$) values, showing the effect of patch width over the size and shape of the shell. (c) $P(r_S)$ is shown for different hard-core shapes as indicated in the figure, calculated for $\Omega^\circ = 74^\circ$, $\epsilon = 0.25$ and $\Delta\omega^\circ = 3^\circ$. (d) The effect of patch range is shown for different ϵ as shown in the figure at $\Omega^\circ = 74^\circ$ and $\Delta\omega^\circ = 4.5^\circ$. (e) $P(r_S)$ is shown for the system at different ϕ (as indicated in the figure) while keeping all the other parameters the same. (f) The effect of temperature over $P(r_S)$ is shown for the shells obtained by using the same parameters. (g) The ratio r_{cc}/b_l where b_l is the distance of the center of mass of a neighboring subunit for different aspect ratios and diameter of the subunit as indicated in the figure for $\Omega^\circ = 74^\circ$. The solid line is a guide to the eye (h) Effect of Ω° over r_{sp}/b_l , showing the latter dominantly controlled by Ω° . The solid line is given by $\frac{1}{2\cos\Omega^\circ}$	143
7.8	The size of the shells predicted by <i>GEMC</i> (blue triangles) and compared with the same obtained by using <i>NVT</i> (black circles). Where the solid line shows the simple relation $1/2\cos\Omega^\circ$ between the patch angle of ω and the size of the shell.	145
7.9	(a) Variation in N_S and (b) variation in R_S is shown, where red line represents <i>Sphere1</i> and black line represents <i>Sphere2</i> of a particular ensemble. System is kept at $\phi_A = 0.1$, $k_B T/u = 0.14$ having patch properties $\Omega^\circ = 74^\circ$, $\Delta\omega^\circ = 4.5$, $\epsilon = 0.25$ and $p = 1.0$	147

Abbreviations

BCD	Brownian Cluster Dynamics
DLCA	Diffusion Limited Cluster Aggregation
EDBD	Event Driven Brownian Dynamics
ECF	Ellipsoid Contact Function
OBB	Object Bounding Box
ER	Ellipsoid of Revolution
MSD	Mean Square Displacement
KFP	Kern Frenkel Polntential
MD	Molecular Dynamics
MC	Monte Carlo
SGMC	Semi Grand-canonical Monte Carlo
US	Umbrella Sampling
HC	Hard Core

Symbols

k_B	Boltzman constant
T	temperature
p	pressure
ϕ	volume fraction
N	number of particles
d	diameter of sphere
L	simulation box size
\hat{n}	director of spheroids
D_o^T	Translational diffusivity of a single sphere suspended in colloidal solution
D_o^R	Rotational diffusivity of a single sphere suspended in colloidal solution
G_θ	Perrin's friction factor for rotational motion
G_{\parallel}	Perrin's friction factor for translational motion along the director
G_{\perp}	Perrin's friction factor for translational motion perpendicular to the director
γ	Friction coefficient
η	Viscosity
s_T	translational step length
s_R	rotational step length
t_{Phy}	physical time
t_{Sim}	simulation time
t_o	time taken by a single sphere to diffuse through the length of its own diameter
PBC	periodic boundary condition

Chapter 1

Introduction

Colloids are a system of particles, with sizes ranging in micrometer length scale, suspended in a fluid medium. In such a system, suspended particles move freely, performing Brownian motion. In nature, there can be several phenomena where colloids can be observed playing an important role. E.g, soap-bubbles, milk sedimentation, aggregation([fig. 1.1](#)), formation of marine ecosystem [\[1\]](#) [\[2\]](#), water absorption by the grain of soil, crack formation etc[\[3\]](#).

Colloidal systems can also help us to understand the properties, which can be scaled from the macroscopic to the molecular and atomic level [\[4\]](#). Specific of such properties are crystallization, diffusivity, reaction kinetics, etc. [\[5\]](#). Such systems are covered within the broad regime of soft matter, which can be modeled and studied by considering purely physical aspects, e.g., shape, size of the potential distribution, geometrical constraints, etc. It can lead to the specific material and chemical properties revealed at the macroscopic level [\[6\]](#).

The beauty of the colloidal system lies in the classical treatment of its physical nature. Fundamental physical properties like diffusivity and viscosity can be scaled and compared to suit the different systems and establish the dynamics of colloids



FIGURE 1.1: Aggregation of the butter content, observable as a shiny wrinkled layer formed over the surface of cooling hot milk tea.

[7] at different length scales. In this way, complex behavior can be observed and studied even at the macroscopic level while following the classical approach [8].

In many biological cells, particles perform passive diffusion while passing through the membrane (fig. 1.2). Therefore, the study of dynamics in colloids can also provide a great insight into the functioning of the biological systems [9]. Such an understanding can have potential applications in the field of biology. Like targeted drug delivery[10] [11], where drugs are supplied only to the affected areas. Porous materials also provide a great [12] medium to study diffusivity, where particles can get absorbed. The study of transport properties in such a medium can reveal different properties of the materials where gas and liquid, both phases of fluid, can be studied. A study of dynamics can also reveal the dimension of such media [13]. Such a study can shed light on the physics of such a complex system and can be used to predict more accurately and enhance the efficiency of the materials [14].

The diffusivity of the particles depends upon their physical properties like shape, size, mass, etc. Therefore, dynamics can be a tool to predict the shape and size of the

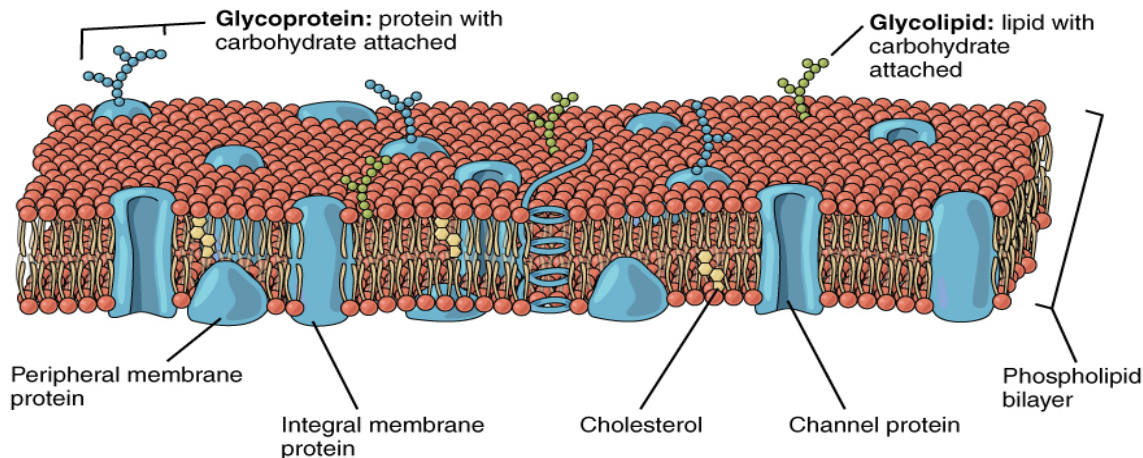


FIGURE 1.2: Schematic of layers in the biological membrane.

Image source - Wikipedia

particles [15]. [16]. In fluid, many works have been done to analytically calculate the effect of shape and size on the transport properties of the colloids and fluid particles. Such works include particles having surfaces defined mathematically, e.g., spheroids and spheres [17]. In fluid within the hydrodynamic limit, particles diffuse faster along the axis with a narrower cross-section [18]. The shape effect dominates the medium, where particles find more confinement or restrictions in the movement [19]. Such mediums include all kinds of porous systems, e.g., biological membranes, cells 1.2, percolated structures, etc. It has been shown that the spheroids diffusing in a 2-D island of obstacles have more diffusivity than the spheres [19]. In this way, we observe that some shapes can be more suitable to diffuse through a particular medium.

Along with the dynamics, shape-anisotropy can lead to phase-rich behavior. Hard-core systems of elongated particles, e.g., spheroids, rods, spherocylinders, have been shown, following the phase transition from isotropic to nematic, which occurs before the arrest of the dynamics leading to the glass transition [20]. Study of the phase behavior of athermal systems, induced by shape-anisotropy, includes both theoretical and experimental approaches [21]. Recently, it was shown experimentally that the

hardcore spheroids go through a new kind of phase transition, known as liquid-glass, which occurs between fluid and glass regime [22]. Particles show frozen dynamics for the orientational degree of freedom despite being able to diffuse translationally without crossing the isotropic-nematic phase boundary. Generally, such dynamics is a characteristic of the nematic phase, where rotation of the particles is restricted to follow the nematic alignment, which leads to the orientational degree of freedom frozen.

Many of the biological systems, including blood flowing in our veins, as well as cells, viruses, and bacteria, fall in the category of colloidal systems. In such a system, inter-particle bonds are often more flexible than the molecular or atomic level system [23]. Particles diffuse and go through the process called self-assembly and form structures that can appear complex at the macroscopic level. The formation of pearl inside scallops and the growth of viruses inside a shell membrane are examples where systems get self-assembled to form mono-dispersed structures like crystals and rods as well as closed systems like spherical shells[24](fig.1.3). Apart from ordered and complex structures, particles can also form disordered aggregates, e.g., blood clotting. Versatility and phase richness comprised by the colloidal system make it an approach of choice for material synthesis [25] through the route of self-assembly and aggregation[26]. Such an approach can come to be more robust as well as more straightforward than the conventional.

Kinetics of aggregation and self-assembly can be observed as being governed by the diffusivity of the suspended particles. This process is called diffusion-limited cluster aggregation (DLCA) [27]. In DLCA systems, bonds are formed instantly when the particle diffuses and comes within the bonding range of other particles. In this way, the dynamical properties like diffusivity and viscosity can be considered a critical factor in deciding the nucleation rate and growth kinetics in the process

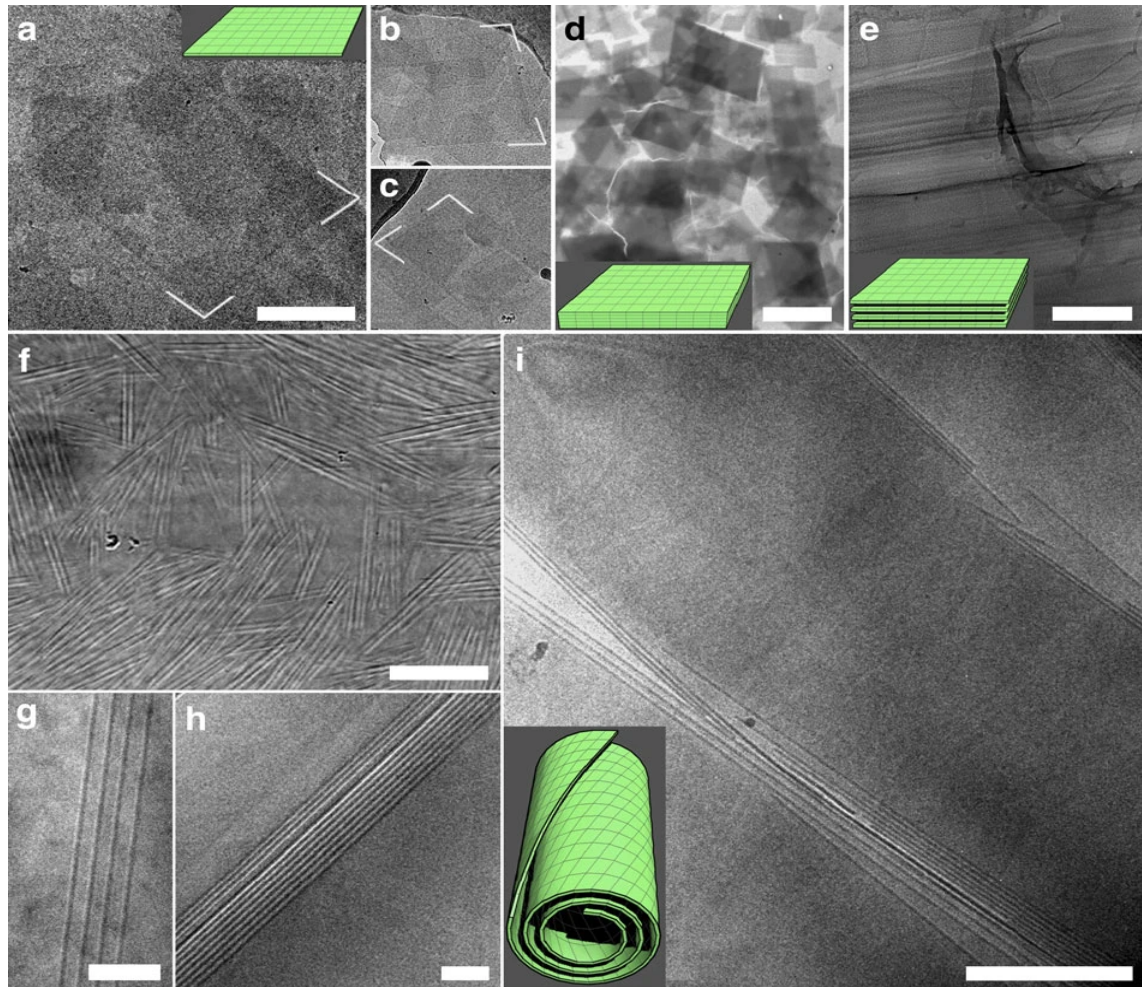


FIGURE 1.3: (a–c) Cryo-TEM pictures of parallelogram nanosheets (d) flake crystals (e) lamellar structures, (f–i) Pictures of multilamellar-tubular structures.
Image source - Nature publication

of aggregation and self-assembly [28]. For such a system (DLCA), shape-anisotropy not only plays a role through its different dynamical properties but also in terms of structural properties (fig. 1.3).

Particle anisotropy can be included in many ways. Introducing the anisotropy in terms of interaction has unraveled the great potential of the self-assembly route. Apart from material synthesis, it also leads us to the new physical properties of such a system [29]. However, most such approaches have been focused on the specific interaction sites attached to the spherical-shaped hardcore potential. The patchy

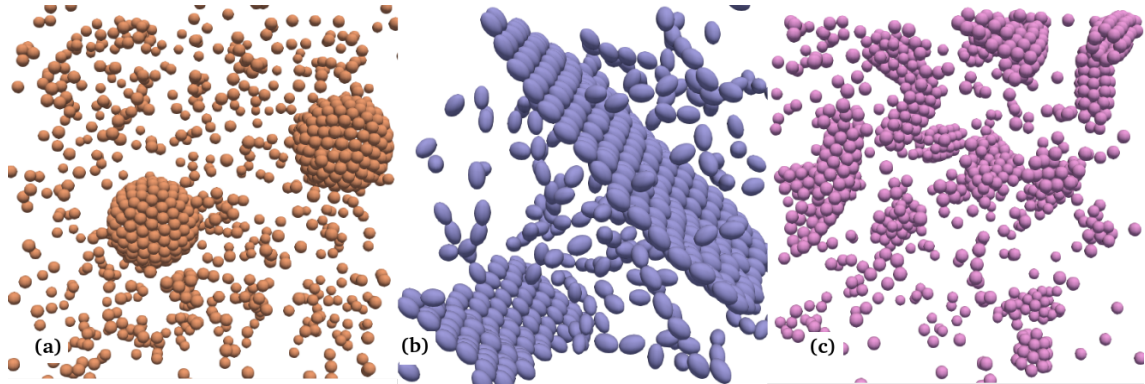


FIGURE 1.4: Shape anisotropy in interaction as well as hardcore leading to the self-assembly of (a)Spherical shells, (b)films, and (c) Tubular structures.

potential is an example of one of the most widely used approaches [30]. This work has been inspired by the same approach while considering anisotropy not only in terms of interaction but also in terms of the shape of the particle (fig. 1.4).

Despite being an essential factor in deciding the dynamical and structural properties, shape-anisotropic particles are less often studied due to the difficulty of implementing the potential distribution in theory and simulation. In the simulation, finding the contact condition for the hardcore becomes computationally expensive.

To consider the effect of shape-anisotropy on the structural and dynamical properties, most of the work has been done while implementing shape-anisotropy in the simplest way. Such a system includes different kinds of shapes like rods, plates, and spheroids [31]. Recently, there has been much work done on the dynamics and phases of such a family of anisotropic hard-core particles. These studies have been done on the phase behavior of the polymorphic system. Such a system also includes the presence of the obstacles and their effect on the dynamics [32].

The present thesis is an effort to study the effect of shape anisotropy on the dynamics and kinetics of the colloidal system, where we consider spheroids the simplest of the anisotropic particle system. The work tries to cover the dynamics of the

spheroidal colloids using the simulation approach. We improvised and used a computationally efficient simulation technique called Brownian cluster dynamics. The one-component and multi-component (binary) systems have been studied and presented as such. Phase behavior in the system of hard-core spheroidal particles has also been studied. After studying the dynamics, the later part of this work deals with the self-assembly of spheroids in a DLCA system. We predicted the phases of spheroids with anisotropic interaction having limited and directional bonding. The last part of the work is dedicated to studying closed structures like spherical shells and cylinders while following the route of DLCA aggregation.

1.1 Outline of the thesis

In Chapter 2, we explain the theory and construction of BCD methodology. We also discuss the improvisation brought in BCD to make it applicable to the spheroidal particle system. We also discuss the kinetics and dynamics of self-assembly.

In Chapter 3, we have explained different simulation techniques and schemes related to calculating kinetics and phases.

In Chapter 4, we report the enhancement in the diffusivity of the spheroids in the presence of spheres.

In Chapter 5, we report the virial coefficient calculated for the patchy spheroids and how it affects the thermodynamic properties differently than the isotropic particle case.

In chapter 6, we report the patchy spheroids leading towards forming a free-standing monolayer. Phase-rich behavior is shown by the elongated particles leading to the 2-D and 3-D crystals.

In Chapter 7, we report breaking the size constraints for the nano-containers using the annular patches.

In Chapter 8, we conclude the presented work.

Part I

**Dynamics and phase-behavior in
the system of hard-spheroidal
colloids**

Chapter 2

Brownian motion and diffusion-limited cluster aggregation in colloidal suspension of hard spheroids

The dynamics of the colloidal suspension are studied while treating the time scale of the fluid response, which is much smaller than that of colloidal particles, which are much heavier and larger than fluid particles. The equation of motion of a single Brownian colloidal particle can be written as,

$$m\dot{\mathbf{v}} = \gamma\mathbf{v} + \xi \quad (2.1)$$

where m is the mass of the particle, $\gamma\dot{\mathbf{v}}$ is the friction term and ξ is the fluctuation due to the solvent. The movement of Brownian particles creates vortices in the surrounding fluid, which decays with time. We call τ_η as the time taken by vortices

to diffuse a distance d , where d is the size of the spherical particle. τ_η is also called viscous relaxation time and can be written as $\tau_\eta = \rho_s d_{sol}^2 / \eta$, where d_{sol} is the size of solvent particles, η , and ρ is the viscosity and solvent density respectively. τ_η ranges between $10^{-10} - 10^{-8}s$. For a time scale $t \gg \tau_\eta$, the influence of colloids on the solvent particles travels infinitely faster and affects the motion of other colloids. The interaction is called hydrodynamic interaction[33]. For a single spherical colloid, the diffusivity is given by the Stokes-Einstein relation as $D_o = k_B T / \gamma$. Where $\gamma = 6\pi\eta d$. The characteristic time for the relaxation of the velocity of a Colloidal particle is known as Brownian relaxation time τ_B . It can be obtained from eq. 2.1 given as $\tau_B = m / 6\pi\eta d$. For $t \gg \tau_B$, the velocity of the Brownian particles equilibrates, where the equipartition theorem can be applied, which gives $v^2 = k_B T / m$.

For the configurational space at a time scale $t \gg \tau_B$, the velocity terms equilibrate and go away. Now the evolution of the probability distribution function $P(\mathbf{r}^N, t)$ can be expressed by using Smoluchowsky equation[33],

$$\frac{\partial P(\mathbf{r}^N, t)}{\partial t} = \sum_{i,j=1}^N \frac{\partial}{\partial \mathbf{r}_i} \mathbf{D}_{i,j} \left\{ \frac{\partial}{\partial \mathbf{r}_j} + \frac{1}{k_B T} \frac{\partial U(\mathbf{r}^N)}{\partial \mathbf{r}_j} \right\} P(\mathbf{r}^N, t) \quad (2.2)$$

Where $\mathbf{D}_{i,j}$ is the diffusivity tensor, $U(\mathbf{r}^N)$ is the inter-particle interaction present due to other colloids in the solvent. At the same time, solvent plays a role only in terms of $\mathbf{D}_{i,j}$. Now we denote t_o as the physical time required for a single particle to diffuse, a distance equal to its own diameter where τ_o can be found off the order of D_o/d^2 . The dynamics defined within the time range $\tau_B \ll t \ll \tau_o$ are called short-time dynamics, where a configuration change becomes non-negligible while playing its role through the term $U(\mathbf{r}^N)$. Diffusivity in the time range is called short-time diffusivity D_S . In the long time limit, $U(\mathbf{r}^N)$ (eq. 2.2) remains constant [33]. For the time range $t \gg \tau_o$, diffusivity is called long time diffusivity D_L . For the volume fraction defined by $\phi = \pi / 6d^3V$, we have long time self diffusivity for

spheres given by Brandon (1994) as $D_L = D_\circ [1 + 2\phi g(2; \phi)]^{-1}$ [16]. $g(2; \phi)$ is the radial distribution function at contact. From Rallison and Hinch (1986), it is shown to be $D_L = D_\circ [1 - 2\phi]$.

Michele et al. (2007)[20] had shown the diffusivity and other self-correlation functions for the fluid of the uni-axial body, where they used event-driven Brownian dynamics simulation. Higher concentration and lower p (close to spherical shape) system lead to the plastic solid. Where $p = a/b$ is the aspect ratio, a, b are the semi-minor and semi-major axis of the spheroid. At higher ϕ and extreme deformation from the spherical shape, the system shows solid. Below the solid regime, elongated particles were found to be following an isotropic-nematic transition.

For the self-diffusivity of spheroids, Bereolos et al. (1993) [17] presented the transport properties calculated using Molecular Dynamics simulation. The result was compared and shown to be consistent with the prediction of Enskog Kinetic theory for anisotropic particles. Although tending towards an infinitely dilute system, the particles show ballistic motion and deviate from the hydrodynamic limit set by the equation $D\eta = C$, known as the Stokes-Einstien product. Where C depends on the slip and stick boundary condition, the deviation from the hydrodynamic limit was also high, at high concentration [17]. Diffusivity of hard-spheroids suspended in the fluid was calculated recently by Marath et al. (2019) [34] implementing hydrodynamic theory by using Langevin equation defined in $6N$ configurational space for a system of N particles. The asymptotic behavior of short-time rotational self-diffusivity D_S^R as well as translational diffusivity D_S^T , close to the extreme deformation ($0 \leq p < \infty$) of the shape, had been shown. Where infinitely thin rods' diffusivity can be shown to diverge. However, in the case of infinitely thin plates, the single particle diffusivity can be seen converging to a particular finite value.

2.1 Diffusivity and phases in the system of shape-anisotropy hard particles

Brenner [35] has given a general relation for the coupling between the translational and rotational diffusivity of the shape anisotropic particles. Yet, due to shape complexity, at high concentrations, it becomes difficult to estimate the diffusivity of the shape-anisotropic particles. Due to this reason, shape anisotropic particles are often treated as spherical, which in some or most cases can not counter the crowding effect or other observed phenomena occurring in the colloidal system [36]. There have been many attempts to estimate the diffusivity of the shape-anisotropic particles using simulations and experiments. For example, particle dynamics modeling methods have been proposed by using different molecular dynamics simulation schemes, e.g., MPCD[37]. Chen et al. used the Doi-Onsager equation [38] of PDF to model the rotational diffusivity of the rods. In the equation of evolution of PDF, they used mean-field torque via MS potential. They have shown the rotational diffusivity by using a tube model, where they construct a tube containing the available volume surrounding the particles. Nematic alignment and diffusivity have been shown. The orientational self-correlation has been shown to decay slowly with increasing shape anisotropy following the isotropic-nematic transition. A sudden jump in order parameters shows a first-order phase transition. The role of shape anisotropy in a porous medium becomes very important, as a particle with directionality can cross through the narrow channel. It has been shown that in a porous medium with an increasing aspect ratio, the diffusivity increases and then stagnates as we increase the same further [39]. The diffusivity has been shown to increase with increasing porosity [40]. The diffusivity decreases with the increase of volume fraction, but the decrease is not as dominant as shown for the non-porous medium. Tracer diffusivity

has been calculated for the system with varying temperatures[41]. Memory effects in the diffusivity have arisen due to the varying temperature. For the different temperature profile shapes, the diffusivity correction shows that the oblate has more correction than the prolate. The diffusivity of cuboids has also been calculated [42, 43]. Where cuboids have been shown following the Fickian dynamics in the short time range and Gaussian dynamics in the long time range. Diffusivity has shown to be minimal for the particle shape showing the biaxial nematic phase. The diffusivity of the spheroids, cuboids, and cubes are also studied using the Gaussian random walk technique [44]. Simple cubic cubes have been shown to have maximum diffusivity in the high-concentration regime compared to other shapes and lattice arrangements. Apart from theoretical, there have been several experimental works[45]. Mainly, such work includes a high frame-rate camera as a tool to measure the mean-square-displacement (MSD)[46, 47, 48]. Other methods are also devised to calculate the short-time diffusivity, like diffusive wave spectroscopy[49]. For example, the diffusivity of the germanium hard nano-wire has been estimated by using such method [50] where they have shown the particle size distribution and the corresponding translational and rotational MSD.

2.1.1 Diffusivity in the presence of obstacles and the effect of confinement

There has been much work done on the dynamics of passive particles in the presence of immobile obstacles[51, 52, 53, 54, 55]. These works include the study of both spherical and shape anisotropic particles in the presence of immobile point particles. Shape-anisotropy of rods has been shown to lead to the increase in diffusivity with increasing obstacle density[53]. Recently, it has been shown that the collision

enhances the diffusivity in the system where particles can diffuse in a specific manner[56]. Diffusivity in the presence of periodic arrangement of the obstacle is greater than the random arrangement[57], where the diffusivity has been calculated using a random lattice model. Segregation of protein present in the cell has been explained by diffusivity through the barrier on the lipid layers or membrane[58]. Where the presence of a barrier leads to slow diffusivity, resulting in the observed segregation. A study on the diffusion done for 2D surface, using an arrangement of 2x2 checkers cross board as obstacles, shows the critical behavior in the transport properties of the particles [59], apart from obstacle diffusion. There have been done many studies on the transport properties of the system with a planer (2d) and cylindrical (1D) confinement. Water molecule confined in a carbon nanotube is shown to diffuse slower with increasing the confinement [60]. Water molecule confined within carbon nano-sheets shows a similar trend[61]. For the polymer with flexible bonds, there can be observed change in the shape as reported using the blobs theory[62] where shape-anisotropy plays an important role. For example, the diffusivity of DNA increases with increasing the slit height working as a confinement[63].

2.2 Kinetics of nucleation and aggregation

From the classical theory of nucleation, one can write the rate equation as [64],

$$\frac{\delta N_c(s, t)}{\delta t} = N_c(s - 1, t)I_{s-1} + N_c(s + 1, t)R_{s+1} - N_c(s, t)I_s - N_c(s, t)R_s \quad (2.3)$$

We can assume the cluster is changing by adding and removing one particle, with a forward and backward rate of I and R , respectively.

For the flux J through the size s we can write a current given as,

$$J(s + \frac{1}{2}, t) = N_c(s, t)I_s - N_c(s + 1, t)R_{s+1} \quad (2.4)$$

We can write the rate in terms of flux as,

$$\frac{\delta N_c(s, t)}{\delta t} = J(s - \frac{1}{2}, t) - J(s + \frac{1}{2}, t) \quad (2.5)$$

For all sizes and time, the flux becomes equal in the case of steady-state [64]. The desired properties we seek in experiment and theory are the nucleation rate corresponding to the state. Such an assumption also makes the problem solvable. Now, a recursion relation is defined as,

$$f_{s+1} = \frac{I_s}{R_{s+1}} f_s \quad (2.6)$$

such that $f_1 = 1$

Now using eq.2.3, 2.4 and 2.5, it can be written as,

$$\frac{J}{I_s f_s} = n_c(s)/f_s - n_c(s + 1)/f_{s+1} \quad (2.7)$$

Now summing this equation for the maximum cluster size s_{max} we have,

$$J \sum_{s=1}^{s_{max}} \frac{1}{I_s f_s} = n_c(1) - \frac{n_c(s_{max})}{f_{s_{max}}} \quad (2.8)$$

Now, from the definition of f_s , it can be written as,

$$f_s = \prod_1^{s-1} \frac{I_s}{R_{s-1}} \quad (2.9)$$

In the stable crystal phase, the forward rate is greater than the backward. It would lead to f_s being ≥ 1 and increasing with an increase in s . Therefore, for sufficiently large s_{max} , we would have the second term in equation 2.7 vanishing. Now we can write,

$$J = n(1) \left(\sum_{s=1}^{\infty} \frac{1}{I_s f_s} \right) \quad (2.10)$$

This expression can give us nucleation rate in terms of I_s and f_s , where these quantities can be defined in terms ΔG [64].

For the aggregation kinetics, we have the rate given by [65]

$$\begin{aligned} \frac{\partial N_c(s)}{\partial t} = & \frac{1}{2} \sum_{i+j=s} K_{i,j} N_c(s) + \sum_{l=1+s}^{\infty} (1 + \delta_{s,l-s}) Y_{l-s,s} N_c(l) \\ & - \sum_{i=1}^{\infty} K_{s,i} N_c(s) N_c(i) - \sum_{i=1}^{s/2} Y_{i,j} N_c(s) \end{aligned} \quad (2.11)$$

Where $K_{i,j}$ is the cluster's aggregation rate with size i, j . $Y_{i,j}$ is the rate dissociation of cluster in size i and j . These rates can be defined infinitely [65]. However, for specific processes, it can be defined according to convenience. For example, $Y_{i,j} = 0$ for all the irreversible processes.

2.2.1 Kinetics of aggregation in a DLCA system of colloids

For the attractive square well potential, we follow the DLCA aggregation procedure. In this procedure, particles satisfying bonding conditions form bonds with probability $\alpha = 1$ following each simulation step. After bond formation, we implement the bond-breaking measures on all the already bonded particles. Bond breakage occurs with the probability β_{bb} .

The total configuration can be expressed in terms of the possibility of the formation and breakage of a bond, which is given as $\alpha + \beta_{bb}$. Now the probability of finding a bond P can be calculated as, $P = \frac{\alpha}{\alpha + \beta_{bb}}$. For DLCA, $\alpha = 1$, therefore we have [66],

$$P = \frac{1}{1 + \beta_{bb}} \quad (2.12)$$

The system achieves equilibrium after sweeping all the particles with bond and formation movement in multiple simulation steps. Let us consider N_{ct} as the total number of contacts satisfying the bonding condition. If N_{bo} is the total number of bonds, on average, out of all the contacts of interest. We can express P as ,

$$P = \frac{N_{bo}}{N_{ct}} \quad (2.13)$$

Let us consider ΔH as the energy difference between a bonded and free contact, which can be an enthalpy difference in this case. From the Boltzmann distribution we have,

$$\frac{N_{bo}}{N_{ct} - N_{bo}} = e^{-\beta\Delta H} \quad (2.14)$$

If $-u_\circ$ is the bond energy or energy difference between bonded and free contact. We can express free energy difference between N_{bo} bonds among all the N_{ct} contacts as,

$$\beta N_{bo} u_\circ = \beta\Delta H + \beta T\Delta S \quad (2.15)$$

where $\beta T\Delta S$ is the entropy difference caused due to N_{bo} bonds out of N_{ct} contacts, given as,

$$\beta T\Delta S = \ln \left\{ \frac{N_{ct}!}{(N_{ct} - N_{bo})! N_{bo}!} \right\} \quad (2.16)$$

From 2.12, 2.13, 2.14 and 2.16 we have,

$$P = 1 - e^{\beta u_o} \quad (2.17)$$

From eq. 2.12 and 2.17 we have,

$$\beta_{bb} = \frac{1}{[1 - e^{\beta u_o}]} - 1 \quad (2.18)$$

where βu_o is a positive number for attractive potential. In BCD, we implement β_{bb} calculated by using the equation mentioned above.

To calculate the kinetics, we start the simulation with a random distribution of particles within the simulation box. We plot ZPI as the number of bonded neighbors averaged over all the particles.

$$ZPI(t) = \frac{1}{N} \sum_{i=0}^N n_b^i(t) \quad (2.19)$$

The average cluster size is given by,

$$C_l = \frac{\sum m N_m}{\sum N_m} \quad (2.20)$$

where N_m is the total number of clusters with size m , while m is the total number of monomers.

2.3 DLCA system of anisotropic particles

Colloidal particles are different and similar in many ways from their atomic and molecular system. For example, colloids have an elastic constant much smaller than

an atomic or molecular level. Their interaction range is also much smaller than their atomic and molecular counterpart in comparison to their particle size. Apart from these differences, there are some similarities. Like, both colloidal and atomic systems can go through nucleation and crystallization. However, atomic crystals have more mechanical strength in comparison to their colloidal counterparts[67].

In colloidal systems, there can be introduced bond directionality using patches[68]. Therefore, we can have a limited number of bonds and valency defined (e.g., engineered particles using coarse graining technique) even for the colloids. In this way, we introduce anisotropy in the colloidal system in terms of the shape of attractive potential. Such a system has attracted researchers since the beginning of the field due to its versatile structural and dynamical behavior and being both explanatory as well as applicable in nature [69, 70]. In the colloidal system, entropy plays an important role [68, 71]. Therefore, a change in the shape of a particle or attractive potential can lead to a radical change in phase as well as dynamical behavior [72, 73]. Janus spheroids have been shown aggregating and forming globular structure[74]. Specific prolate particles have been shown to be forming tubular structures. There are many methods proposed to prepare such particles with specific shapes [75], which can be used in the field of fabrication of nano-devices. It also has a potential application in the field of targeted disease treatment and drug delivery [76, 77]. There have been many studies done on the DLCA of isotropic as well as anisotropic potential[78, 79]. But most of the work, specifically in simulation, includes spheres [80]. In the simulation, computational efficiency associated with the overlap condition of complex shapes leads to adopting the spherical-shaped coarse-grained model of the colloids, which may not show the effect arising due to anisotropic hard-core. In this thesis, we try to focus on this part and study the DLCA system of anisotropic particles. Where we introduce not only the anisotropy in terms of attractive potential but also

the particles' shape. Introducing shape anisotropy leads us to the self-assembled specific mono-dispersed 3d structures. The introduction of geometric constraint can also be observed to form structures like free-standing monolayers, which is discussed in the later chapters of the thesis.

2.3.1 Closed system of spherically symmetric structures in the living organism and other non-living colloidal systems.

There are plenty of examples of closed structures present in nature, e.g., viruses, cells, and nano-cages of protein [81]. These nano-cages depict specific spherical symmetry, e.g., icosahedral, dodecahedral. As like in the case of 3d crystals, the stability of these structures has been found to be dependent upon the type of symmetry present in the system [82]. The effect of physical conditions on the stability of closed structures can give us great insight into the behavior of biological entities like viruses. For example, nature is abandoned by small-size viruses. Most of these viruses have some spherical symmetry. For icosahedra symmetry, we can have $10n^2 + 2$ number of vertices, where n is the total number of sections over the edge of the icosahedra. This relation gives the allowed number of particles assembled with icosahedral symmetry as 12, 42, 92, 162, etc. The closed structures with these specific numbers of particles are more stable. In this way, these studies not only provide us with an understanding but also inspire the field of material synthesis. For peptides, it has been shown that the aromatic compound self-assembles to form nano-cages [83]. These cages have trapping properties that can be used for sensing hazardous materials [84]. The approach of colloidal self-assembly has been used for the fabrication of photonic crystals [85]. The theoretical work done on the study

of the closed structures is focused on the kinetics and symmetry [86]. These works include colloids with specific shapes forming highly directional bonds [87, 88]. In the presented thesis, we have taken spherical particles with annular patches, which is an axially symmetric potential. We found that the icosahedral structure is not the only minimum potential energy configuration in the closed system, having spherical constituent particles with axially symmetric potential. The details of the work are discussed in the later chapters.

2.4 Anisotropic potential models (Kern-Frenkel potential)

Since the introduction of the shape-anisotropic patchy-potential [89], having the property of strong directional bonding, we have plenty of work done in such a system. The use of square well potential has become the choice of researchers due to its simplicity when applied to any MC scheme, including BCD. As, in this kind of potential, we have bond forms as long as the particle comes within the range of the square well potential[90]. While a patch is defined using a patch vector \hat{n} with respect to the bond vector $\mathbf{r}_{i,j}$, having patch angle ω , given as,

$$\chi_{i,j} = \begin{cases} 1 & \hat{\mathbf{r}}_{ij} \cdot \hat{\mathbf{n}}_i \geq \cos(\omega) \\ 0 & Otherwise \end{cases} \quad (2.21)$$

To relate the potential with pressure and other thermodynamic properties, the radial distribution function calculated at equilibrium can be used [89]. One can also perform an NPT or GCMC scheme to implement pressure and chemical potential directly into the system, which can be applied to the calculation of the phase diagram,

as discussed in the next chapter. Experimentally, we can decorate the particles' surface with hydrophobic and hydrophilic properties, making them interact attractively only on one side. Such particles are modeled in the category of Janus particles [91]. A particle can be decorated with patches on its poles, often referred to as patchy particles or two-patch model [92]. In one patch model, particles interact only with one patch[93]. In the multiple patch models, we have many patches decorated on the surface of the spheres [94]. Such models have been observed to show interesting and unique thermodynamic and structural properties. Giving us a new insight into the versatility of the system. For example, patchy particles with a reduced number of bonds lead to the liquid state and then to the vanishing packing fraction, which is not observable for the isotropic potential [95]. In the presented thesis, we have used patchy particles having a spheroidal hardcore, while the two patches are defined at both ends along the symmetry axis of spheroids. We also used a single patch model, termed annular patches. The details of the structure, kinetics, and thermodynamics of these systems are discussed in the later part of the thesis.

Chapter 3

Simulation methods to calculate dynamics, kinetics, structures, and phase-diagram

This thesis aims to study the kinetics and structural properties in the DLCA system of anisotropic pair-potential, where we explore the effect of interaction leading to limited and directional bonding. To calculate the kinetics of aggregation of spheroids, we improvised and used BCD. All the *NVT* ensemble calculations presented in this work have been done while using BCD. This chapter explains the further construction of BCD done for the aggregation study. In the later part of the chapter, we discuss the other ensembles, e.g., *NPT* and floppy simulation, to calculate and predict structural properties. We also give details about *SGMC* simulation to calculate cluster size distribution and free energy. In the last part of the chapter, we discuss the methods used in this work to draw the corresponding phase diagram.

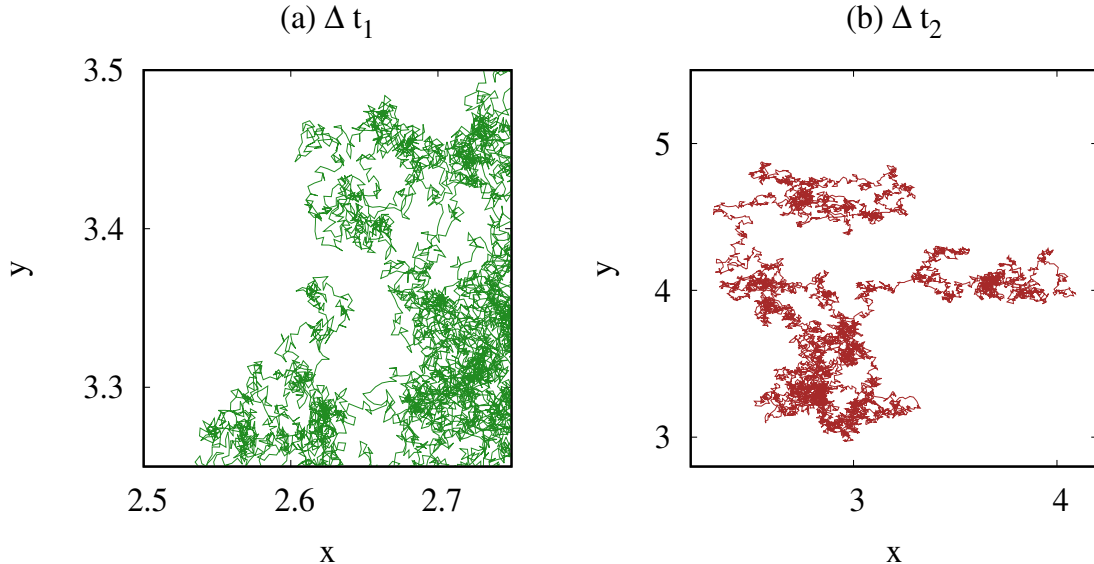


FIGURE 3.1: Brownian motion is shown with different Δt such that $\Delta t_2 = 10 \Delta t_1$. Over a long time period ($t \gg \Delta t$) motion can be observed to be Brownian for both scaled time steps Δt_1 and Δt_2 .

3.1 Brownian motion: Wiener process and scaling

One of the characteristics of Wiener processes is the self-similarity. This property can be used for the purpose of scaling, as shown in the figure.

The trajectory of a particle, going through Brownian motion, while obtained at times separated with a fixed time interval Δt gives the same trajectory for different values of Δt (fig. 3.1). As discussed in the previous section (sec. 2), for the $t \gg \tau_B$, we have velocity relaxed and can be expressed as $v = k_B T / m$. Now, we can choose an Δr such that $r = v\Delta t$ where v can have any random direction. The choice of Δt can be anything for the diffusivity of single spheroids suspended in the fluid with infinite volume. But for a finite v and ϕ , we can not choose Δt larger than an appropriate value [96] as a particle can face the cage effect in the presence of other Brownian particles. Putting it randomly at a position far from the initial can lead to a nonphysical condition.

In this case, diffusivity becomes smaller than the single particle diffusion. Although, for a sufficiently small Δt regime, the movement remains Brownian. From the Stokes-Einstein relation, we have,

$$D_T = \frac{k_B T}{3\pi\eta d} \quad (3.1)$$

Where D_T is the translational diffusivity of spheres.

$$D_R = \frac{k_B T}{\pi\eta d^3} \quad (3.2)$$

Where D_R is the rotational diffusivity of spheres.

Now, for a single spherical particle suspended in fluid, we can write,

$$\langle \mathbf{R}^2 \rangle = |\sum \mathbf{v}\Delta t|^2 = S_1^2 + S_2^2 + S_3^2 \dots + 2\mathbf{S}_1 \cdot \mathbf{S}_2 + 2\mathbf{S}_1 \cdot \mathbf{S}_3 + 2\mathbf{S}_1 \cdot \mathbf{S}_4 + \dots \quad (3.3)$$

Let us define $\mathbf{v}\cdot\Delta t = \mathbf{S}_T$, with S_T being the translational step generated randomly with random orientation to mimic the Brownian process. If we keep the length of S_1, S_2, \dots same and equal to S_T , while keeping the direction of the vector random, the above equation can be rewritten as,

$$\langle \mathbf{R}^2 \rangle = t_{sim} S_T^2 \quad (3.4)$$

Where t_{sim} is the number of times a particle's position, incremented through the step length \mathbf{S}_T , known as simulation time. It can also be written as,

$$\langle \mathbf{R}^2 \rangle = t_{sim} S_T^2 = 6D_T t \quad (3.5)$$

For a short time, we have the orientation vector of the particle \mathbf{n} , performing Brownian motion over the surface of the sphere with radius n . We can write,

$$\langle |\mathbf{n} - \mathbf{n}_0|^2 \rangle = n^2 4D_R t = t_{sim} S_R^2 \quad (3.6)$$

Now, we define t_\circ as the time taken by a single spherical particle to diffuse through a length equal to its own size d . From equ. 3.5 we have,

$$t/(d^2/D_T) = t_{sim} S_T^2 / d^2 = t_{phy}/t_\circ \quad (3.7)$$

Where $d^2/D_T = t_\circ$. In this way, we establish the relation between physical time t_{phy} and simulation time t_{sim} .

Now to scale energy stored between translational and rotational degrees of freedom.

We can use equ. 3.1 3.2, where dynamics is scaled for a time $t_{phy} \gg \tau_B$. We get,

$$D_R = 1/2t_\circ \quad (3.8)$$

Using equ.3.5 and 3.6, we have step lengths scaled as [97],

$$S_R^2 = 2 S_T^2 \quad (3.9)$$

On the basis of scaling, we can mimic the dynamics of the particles performing Brownian motion while suspended in fluid.

3.1.1 Dynamics and scaling for spheroidal colloids (shape-anisotropic hard-core): With stick boundary condition

In BCD, the particle's center of mass undergoes a translation with constant step size S_T in a random direction [97] as discussed in the previous section. When S_T is small, the random walk of the center of mass of a sphere can be approximated to a diffusion problem [98]. For a single sphere, the relation between the physical time t_{Phy} and the simulation time t_{Sim} is given by

$$\frac{\langle R^2 \rangle}{d^2} = t_{Sim} \frac{S_T^2}{d^2} = 6D_T^\circ \frac{t_{Phy}}{t_0}. \quad (3.10)$$

where $\langle R^2 \rangle$ is the mean square displacement of the sphere's center of mass. t_0 is defined as the time a single sphere takes to travel its own diameter d , such that $D_T^\circ = 1/6$ is the translational diffusion coefficient of a single sphere. In the present work, the simulation time is defined as $\frac{t_{Phy}}{t_0} = t_{Sim} \frac{S_T^2}{d^2}$ as we have considered all the ellipsoids to have a volume equal to a sphere with $d = 1$.

The ellipsoid will also undergo a random rotation along the symmetry axis. Along the other two perpendicular axes to the symmetry axis, no rotation is undertaken as it is symmetric. The random rotation of the tip of the unit vector \hat{n} along the symmetry axis of ER will perform a two-dimensional random walk on the surface of a sphere with a step size S_R , similar to rotation done for spherical patches [99, 100]. When the step size is small, it will undergo rotational diffusion with a diffusion coefficient D_R . In the limit $D_R t \ll 1$,

$$\langle (\hat{n}(t) - \hat{n}(0))^2 \rangle = t_{Sim} \frac{S_R^2}{d^2} = 4D_R^\circ \frac{t_{Phy}}{t_0}. \quad (3.11)$$

where D_R° is the rotational diffusivity of the vector, and we can show that $\sqrt{2}S_T = S_R$ [99].

For a spherical particle, we know from the Stokes-Einstein relation for diffusion D_T , and D_R are related to the friction coefficient as [101],

$$D_T = \frac{k_B T}{\gamma} \quad (3.12a)$$

$$D_R = \frac{k_B T}{\gamma_\theta} \quad (3.12b)$$

where k_B is the Boltzmann constant, T is the temperature. γ and γ_θ are the friction coefficient for the translational and rotational diffusion, respectively, given by

$$\gamma = 6\pi\eta \frac{d}{2} \quad (3.13a)$$

$$\gamma_\theta = 6\eta V^\circ \quad (3.13b)$$

where η is the viscosity of the solvent, and V° is the volume of the particle.

For the asymmetric ellipsoidal particle, the diffusion coefficient D_T is resolved along the parallel and perpendicular plane of the symmetry axis as

$$D_T = \frac{2}{3}D_T^{\parallel} + \frac{1}{3}D_T^{\perp} \quad (3.14)$$

D_T^{\perp} is the diffusion coefficient in the perpendicular direction of the symmetry axis, D_T^{\parallel} is the diffusion coefficient parallel to the symmetry axis.

The change in D_T and D_R for an ellipsoidal particle compared to a spherical particle can be expressed in terms of the friction coefficient γ and γ_θ given by [102]

$$\gamma^{\perp or \parallel} = 6\pi\eta b G_T^{\perp or \parallel} \quad (3.15a)$$

$$\gamma_\theta = \eta V^o G_\theta \quad (3.15b)$$

where b is the length of the semi-minor axis and G is the Perrin friction factor [103, 104]. G measures the deviation in friction coefficient when the particle deviates from spherical to ellipsoidal shape. G_θ gives the deviation in the rotational friction coefficient. G_T^\parallel and G_T^\perp for the translational friction coefficient along the parallel and perpendicular direction of the symmetry axis, respectively. For the stick boundary condition at the surface of spheroids, the factor G [103, 105], for the prolate case $p > 1$ is given as,

$$G_T^\parallel = \frac{4}{3} \left[\frac{p}{(1-p^2)} + \frac{2p^2-1}{(p^2-1)^{3/2}} \ln(p + \sqrt{p^2-1}) \right]^{-1} \quad (3.16a)$$

$$G_T^\perp = \frac{8}{3} \left[\frac{p}{(p^2-1)} + \frac{2p^2-3}{(p^2-1)^{3/2}} \ln(p + \sqrt{p^2-1}) \right]^{-1} \quad (3.16b)$$

$$G_\theta = \frac{2(p^4-1)}{3p} \left[\frac{(2p^2-1)}{\sqrt{p^2-1}} \ln(p + \sqrt{p^2-1}) - p \right]^{-1}. \quad (3.16c)$$

For the oblate case, $p < 1$,

$$G_T^\parallel = \frac{4}{3} \left[\frac{p}{(1-p^2)} + \frac{1-2p^2}{(1-p^2)^{3/2}} \arccos(p) \right]^{-1} \quad (3.17a)$$

$$G_T^\perp = \frac{8}{3} \left[\frac{p}{(p^2-1)} + \frac{3-2p^2}{(1-p^2)^{3/2}} \arccos(p) \right]^{-1} \quad (3.17b)$$

$$G_\theta = \frac{2(p^4-1)}{3p} \left[\frac{(2p^2-1)}{\sqrt{1-p^2}} \arccos(p) - p \right]^{-1} \quad (3.17c)$$

The parameter $G \rightarrow 1$, as the aspect ratio $p \rightarrow 1$, which corresponds to a sphere.

We have kept S_T constant in the present work. To incorporate the effect of anisotropic diffusion, we have introduced 2 different step sizes, along the parallel direction S_T^{\parallel} and along the perpendicular direction S_T^{\perp} of the symmetry axis. The diffusion of ER along the direction parallel to the symmetry axis was compared with that of a sphere with the same volume, along with the equation. 3.10, it can be shown $D_T^{\parallel}/D_T^{\circ} = (S_T^{\parallel})^2/S_T^2$. Combining eq. 3.10, 3.12 and 3.14 the relation between the transitional and rotational step size of the ER compared to a sphere of the same volume can be calculated by

$$\frac{S_T^{\perp,\parallel}}{S_T} = \sqrt{\frac{d}{2bG_T^{\perp or \parallel}}} \quad (3.18a)$$

$$\frac{S_R^e}{S_T} = \sqrt{\frac{2}{G_\theta}} \quad (3.18b)$$

In the simulation, we fixed the step size $S_T^2 = \frac{2}{3} (S_T^{\parallel})^2 + \frac{1}{3} (S_T^{\perp})^2$, similarly the step size for rotational diffusion is calculated from the equation. 3.17b.

3.2 Simulation technique: Brownian Cluster Dynamics (NVT)

BCD is an MC technique that incorporates the concept of physical time in terms of simulation time, as explained in the sec 3.1. In BCD, we start the simulation by randomly distributing particles within the simulation box with sides connected through the periodic boundary conditions. A simulation time is defined as the $2N$ steps. Where in each step, we randomly select a particle and either translate or rotate it with equal and half probability. In this way, we ensure at least one rotational and

one translational step is performed on every particle in each simulation step. The movement steps are explained below.

3.2.1 Movement steps

For the translational step, we randomly generate direction in 3D given by the expression,

$$\begin{aligned}\theta &= \cos^{-1}(1 - 2 \text{rand}_1) \\ \phi &= 2\pi \text{rand}_2\end{aligned}\tag{3.19}$$

where rand_1 , rand_2 are the random numbers generated uniformly within the range $[0, 1]$. We move the particle with a fixed step length s_T given by the expression-

$$\mathbf{r} = \mathbf{r}_i + S_T (dx \hat{i} + dy \hat{j} + dz \hat{k})\tag{3.20}$$

where, $dx = \sin(\theta)\cos(\phi)$, $dy = \sin(\theta)\sin(\phi)$, $dz = \cos(\theta)$. To rotate the particle, we take the particle's frame of reference. We define the particle's orientation by a unit vector \hat{n} . Where \hat{n} is aligned in the z-direction. We rotate the director of the particle by randomly choosing the direction of the rotation vector within the xy-plane of the rigid body. Here, we do not strictly follow the detailed balance, as the particle will always go in rotational or translational movement with a fixed non-zero step length (s_T and s_R)[\[106, 107\]](#). Despite this fact, it leads to a correct kinetic and dynamic evolution.

It can be shown as follows. Let us say we choose the rotation axis in all the (3D) directions with respect to the rigid body instead of choosing it randomly from the $x - y$ plane (where in the rigid body frame z-axis aligns with the symmetry axis).

This method of generation of the rotation axis will lead to cases where some rotation axes will be chosen along the symmetry axis of the body. In all such cases, the tip of the orientation vector (lying along the symmetry axis) will perform zero movement on the surface of the sphere having a unit radius. Movement of the tip will be maximum in the case of the rotation axis chosen in the $x - y$ plane of the rigid body. In this way, we see that rotational movement s_R varies from a maximum assigned value s'_R to 0. It will lead to the reduction in rotational MSD . However, the relation between the gained arc length s_R and applied rotational step length s'_R can be expressed as follows,

$$s_R = \sin^{-1} \{ \sin(s'_R) \sin(\theta) \} \quad (3.21)$$

Where θ is the angle between the symmetry axis of the rigid body and the axis of rotation. To compensate for the lowered value of MSD , we can choose the higher s'_R , which can lead to the same rotational MSD . For this purpose, we calculate a_R root of the average of the square of s_R gained by applied s'_R , which is given as,

$$a_R = \sqrt{\langle s_R^2 \rangle} \quad (3.22)$$

s_R (eq. 3.21) is a function of θ (polar angle) (for a fixed s'_R); the angle between the rotation axis and the tip of the orientation vector, aligned parallel to the body axis. Average is taken over distribution of θ , which is given as $\frac{1}{2} \sin\theta$ if all the axes of rotations are equally probable (distributed in 3D). $\langle s_R^2 \rangle$ is given as,

$$\langle s_R^2 \rangle = \frac{1}{2} \int_0^\pi s_R(\theta)^2 \sin\theta d\theta = \frac{1}{2} \int_0^\pi [\sin^{-1} \{ \sin(s'_R) \sin\theta \}]^2 \sin\theta d\theta \quad (3.23)$$

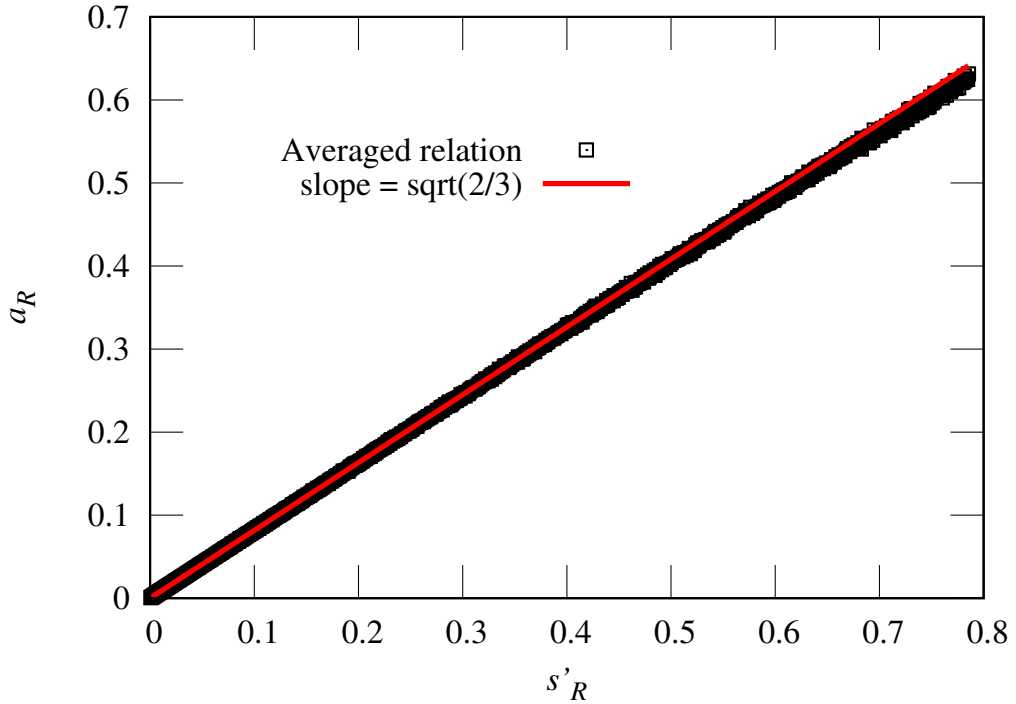


FIGURE 3.2: The relation between applied rotation s'_R to the gained arc length a_R is shown. The slope is equivalent to the $\sqrt{2/3}$ for the small rotations (red line), while for larger rotations, the slope deviates.

Fig 3.2 shows the variation of a_R with respect to the applied step length s'_R . Where we find that a_R (the root mean square of the s_R ; gained arc length) comes to be around $\sqrt{2/3}$ times smaller than applies step s'_R for smaller values of applied rotational step length (when $s'_R < 0.5$). In this way, s'_R multiplied by a factor of $\sqrt{3/2}$ can give the desired a_R as if the rotation was done by choosing the axis of rotation randomly within the plane perpendicular to the particle's symmetry axis (see fig.3.2). Now, to show the evolution of the system as being free of the requirement of strict detailed balance we took two systems; one with rotation performed by choosing the axis randomly in the $x - y$ plane and the other by choosing the axis in all directions with respect to the rigid body. We calculated L_2 given by,

$$L_2(t) = \left\langle \frac{1}{2} \{3\cos^2(\theta(t)) - 1\} \right\rangle \quad (3.24)$$

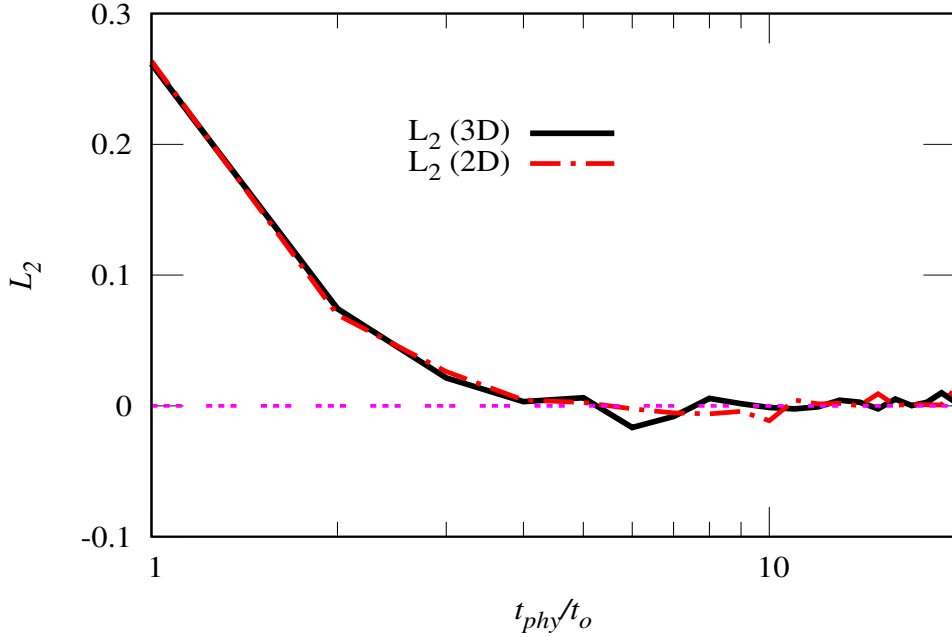


FIGURE 3.3: L_2 is shown for the two different systems of prolate spheroids ($p = 2$) at $\phi = 0.4$. The red line represents the system with the axis selection in 3D and the black line in the X-Y plane of the rigid body (2D).

where $\theta(t)$ is the angle between the two different orientations of the director of the same spheroid, measured after time interval t .

We took a system of spheroids with $p = 2.0$ and at $\phi = 0.4$. It shows the same evolution of L_2 (see Fig 3.3) and $D_R/D_R^\circ = 0.45$.

3.2.2 Implementation of Rotational movement

The tip of the unit vector moves over the sphere's surface through the step length s_R . Now, the rotated vector is brought back into the laboratory frame. To rotate the vector, we use quaternion. For the rotation of a vector through the angle, θ , around an axis defined as $x\hat{i} + y\hat{j} + z\hat{k}$. The transformation performed over \hat{n}_i , initial

orientation of the particle is given as,

$$\hat{n} = \hat{T}(x\hat{i} + y\hat{j} + k\hat{k}, \theta)\hat{n}_i \quad (3.25)$$

where \hat{n} is the final orientation of the director. While \hat{T} is the transformation matrix defined as,

$$\hat{T} = \begin{bmatrix} 1 - 2(w_j^2 + w_k^2) & 2(w_i w_j - w_k w_t) & 2(w_i w_k + w_j w_t) \\ 2(w_i w_j + w_k w_t) & 1 - 2(w_i^2 + w_k^2) & 2(w_j w_k - w_i w_t) \\ 2(w_i w_k - w_j w_t) & 2(w_j w_k + w_i w_t) & 1 - 2(w_i^2 + w_j^2) \end{bmatrix} \quad (3.26)$$

where $w_t = \cos(\theta/2)$, $w_i = -\sin(\theta/2)x$, $w_j = -\sin(\theta/2)y$ and $w_k = -\sin(\theta/2)z$.

Rotational mean-square displacement (MSD_R) can be calculated by adding the rotational $\hat{\omega}$ vector (representing rotational angular velocity) and averaging over all the particles. It can be expressed as [108]

$$\Phi(\tau) = \int_0^\tau \hat{\omega}(t) dt \quad (3.27)$$

where $\tau = 1/S_T^2$. $|\Phi(\tau)| = S_R$.

$$MSD_R(t) = \langle |\Phi(\tau + t) - \Phi(\tau)|^2 \rangle \quad (3.28)$$

Rotational diffusivity D_R is given as,

$$MSD_R = 4Dt \quad (3.29)$$

3.2.3 Cell division of simulation box and periodic boundary condition

We divide the simulation box into n_b number of blocks in each direction. Such that each block has size $b_l : \sigma \leq b_l \leq 2\sigma$. Choosing the size within the given limit ensures that each particle interacts only with the nearby cells. In this way, a particle's interaction is counted only with the particles falling within the range of first neighbor cells, counted as 3^{dim} where dim is the dimension of the system. For a cubic simulation box with size L . The number of blocks is defined as $n_b = \text{floor}(L/\sigma)$. *floor* gives the highest integer value, less than (L/σ) . Therefore, the block length is given as $b_l = L/n_b$. In this way, the simulation box with volume L^3 gets divided into n_b^3 number of cells.

The periodic boundary condition is implemented as,

$$\begin{aligned} x > L : \quad x &= x - L \\ x < 0 : \quad x &= x + L \\ n'_b > n_b : n'_b &= n'_b - n_b \\ n'_b < 1 : n'_b &= n'_b + n_b \end{aligned} \tag{3.30}$$

where n'_b is the current block number. n_b is the total number of blocks on each side, with the first block counted as 1.

3.2.4 Interaction between the particles contained within the cell, connected through the periodic boundary condition

Along all the three orthogonal axes of the box, n_b^{th} cell is connected with the 1st cell through PBC. The distance between the particles within the cell, connected through PBC, is given as,

$$x_i - x_j : \quad x_i - x_j = \begin{cases} x_i - x_j + L & x_i - x_j < 0 \\ x_i - x_j - L & x_i - x_j > 0 \end{cases} \quad (3.31)$$

where x_i and x_j are the positions of the particles within the cells i and j, connected through the PBC. All the pairwise interactions are calculated while considering the inter-particle distance resulting after applying PBC.

3.2.5 Spheroids and overlap condition: Ellipsoid contact function

The shape and size of a spheroid are defined by the aspect ratio $p = a/b$, where a is the length of the major axis, also the axis of symmetry. b is the length of the minor axis. We consider the orientation \hat{n} of the particle, [109] along the symmetry axis of the particle. We define a spheroid as,

$$\mathbf{A} = \begin{bmatrix} \mathbf{u}_i & \mathbf{u}_j & \mathbf{u}_k \end{bmatrix} \begin{bmatrix} \frac{a}{2}^{-2} & \frac{b}{2}^{-2} & \frac{b}{2}^{-2} \end{bmatrix} \begin{bmatrix} \mathbf{u}_i & \mathbf{u}_j & \mathbf{u}_k \end{bmatrix}^T \quad (3.32)$$

where \mathbf{u}_i s are the orthogonal vectors along the three body axes of the spheroid. The inverse of the 3x3 matrix can be written as,

$$\mathbf{A}^{-1} = \begin{bmatrix} \mathbf{u}_i & \mathbf{u}_j & \mathbf{u}_k \end{bmatrix} \begin{bmatrix} \frac{a^2}{2} & \frac{b^2}{2} & \frac{b^2}{2} \end{bmatrix} \begin{bmatrix} \mathbf{u}_i & \mathbf{u}_j & \mathbf{u}_k \end{bmatrix}^T \quad (3.33)$$

For any spheroids defined as, A and B , the object function $S(\mathbf{R}, A, B)$ [110] is defined as,

$$S = \lambda(1 - \lambda)\mathbf{R}^T [(1 - \lambda)\mathbf{A}^{-1} + \lambda\mathbf{B}^{-1}]^{-1}\mathbf{R} \quad (3.34)$$

where \mathbf{R} is the vector pointing from the center of mass of spheroid \mathbf{A} to spheroid \mathbf{B} . The ellipsoid contact function (ECF) is defined as,

$$ECF = \{max \quad S(\lambda) \quad | \quad \lambda \in [0, 1]\} \quad (3.35)$$

\S can be rewritten as,

$$S = \lambda(1 - \lambda)\mathbf{R}^T \mathbf{G}^{-1} \mathbf{R} \quad (3.36)$$

where \mathbf{G} is defined as,

$$\mathbf{G} = [(1 - \lambda)\mathbf{A}^{-1} + \lambda\mathbf{B}^{-1}] \quad (3.37)$$

Where $\mathbf{G}^{-1}\mathbf{R}$ is given as the characteristic vector of the equation,

$$\mathbf{G}\mathbf{x} = \mathbf{R} \quad (3.38)$$

We calculate the value of $x = \mathbf{G}^{-1}R$ by using the Gaussian elimination method. We use an iterative method to find out the ECF following the eq. 7.2. Another way is

to calculate the derivative of S given as,

$$S' = (\mathbf{G}^{-1}R)^T [(1 - \lambda)^2 \mathbf{A}^{-1} - \lambda^2 \mathbf{B}^{-1}] (\mathbf{G}^{-1}R) \quad (3.39)$$

The bisection method can be used while considering $\lambda = 0, 1$ as an initial value and locating the zero of the function $S'(\lambda)$. We take the corresponding λ to find the ECF by putting it into equ. 3.35. The overlap condition for the two spheroids with any shape is given as,

$$ECF = \begin{cases} < 1 & \text{overlapping} \\ = 0 & \text{touching surfaces} \\ > 1 & \text{non-overlapping} \end{cases} \quad (3.40)$$

ECF can also be written as,

$$ECF = R^2 \{ \max S(\lambda, \mathbf{A}, \mathbf{B}, \hat{R}) \mid \lambda \in [0, 1] \} \quad (3.41)$$

In this way, the value of λ depends just on the orientation of spheroids relative to \hat{R} .

To calculate the particles laying within the range of ϵ , defined as the distance between the surfaces of spheroids, we calculate the ECF as,

$$ECF = (R - \epsilon)^2 \{ \max S(\lambda, \mathbf{A}, \mathbf{B}, \hat{R}) \mid \lambda \in [0, 1] \} \quad (3.42)$$

ECF: Condition for Overlap

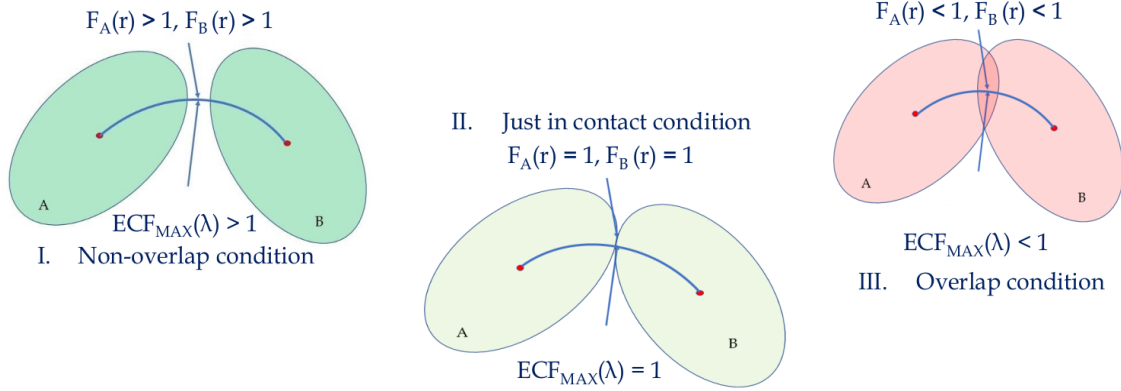


FIGURE 3.4: ECF shown for different conditions. The blue line shows the corresponding points with the variation of $S(\lambda)$ with $\lambda \in [0, 1]$. Maximum of $S(\lambda)$, corresponds to the point which lies closest to the surface of spheroids, shown with the tip of the arrow.

The condition is given as,

$$ECF = \begin{cases} < 1 & \text{within the range} \\ = 0 & \text{just in range} \\ > 1 & \text{out of the range} \end{cases} \quad (3.43)$$

The above condition can be used for the square well potential to check that the particle is within the range of interaction.

3.2.6 An efficient method to calculate the overlap of two spheroids

As discussed in the previous section, it is not possible to calculate the exact value of ECF . It can be calculated only near the exact value by using various numerical schemes to find the maxima of the function $S(\lambda, \mathbf{R}, \mathbf{A}, \mathbf{B})$ with respect to λ . We

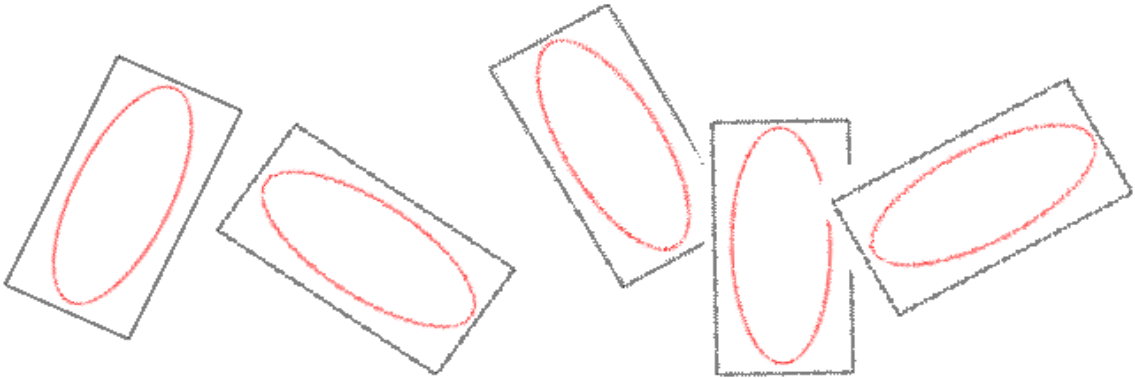


FIGURE 3.5: Rectangular boxes enclosing the particles. Particles can overlap only when the rectangular boxes overlap.

apply *ECF* only if the distance between spheroids $R^2 < (a + a')^2$, while a and a' is the length of the semi-major axis of spheroids A and B . We also used *OBB* object bounding box [111]. Where *OBB* is defined in such a way that it envelopes the whole particles in a parallelopiped (shown in Fig 3.5) for a 2-D system, where the particle is enclosed in a rectangular box).

Let us take two spheroids defined as

$$\mathbf{A} = \begin{bmatrix} \mathbf{u}_i & \mathbf{u}_j & \mathbf{u}_k \end{bmatrix} \begin{bmatrix} \frac{a}{2}^{-2} & \frac{b}{2}^{-2} & \frac{b}{2}^{-2} \end{bmatrix} \begin{bmatrix} \mathbf{u}_i & \mathbf{u}_j & \mathbf{u}_k \end{bmatrix}^T \quad (3.44)$$

$$\mathbf{B} = \begin{bmatrix} \mathbf{w}_i & \mathbf{w}_j & \mathbf{w}_k \end{bmatrix} \begin{bmatrix} \frac{a'}{2}^{-2} & \frac{b'}{2}^{-2} & \frac{b'}{2}^{-2} \end{bmatrix} \begin{bmatrix} \mathbf{w}_i & \mathbf{w}_j & \mathbf{w}_k \end{bmatrix}^T \quad (3.45)$$

Now we define a vector, with components as,

$$\begin{aligned} V_i &= \mathbf{R} \cdot \mathbf{w}_i \\ V_j &= \mathbf{R} \cdot \mathbf{w}_j \\ V_k &= \mathbf{R} \cdot \mathbf{w}_k \end{aligned} \quad (3.46)$$

and a matrix

$$\mathbf{M} = \begin{bmatrix} \mathbf{u}_i \cdot \mathbf{w}_i & \mathbf{u}_j \cdot \mathbf{w}_i & \mathbf{u}_k \cdot \mathbf{w}_i \\ \mathbf{u}_i \cdot \mathbf{w}_j & \mathbf{u}_j \cdot \mathbf{w}_j & \mathbf{u}_k \cdot \mathbf{w}_j \\ \mathbf{u}_i \cdot \mathbf{w}_k & \mathbf{u}_j \cdot \mathbf{w}_k & \mathbf{u}_k \cdot \mathbf{w}_k \end{bmatrix} \quad (3.47)$$

$$\mathbf{M}_a = |\mathbf{M}| \quad (3.48)$$

We define two vectors again as,

$$\begin{aligned} r_i^A &= a/2, r_i^A = b/2, r_i^A = b/2 \\ r_i^B &= a/2, r_i^B = b/2, r_i^B = b/2 \end{aligned} \quad (3.49)$$

Now we define two scalar quantities, s_1 and s_2 , as,

$$\begin{aligned} i \ s_1 &= r_i^A \\ s_2 &= r_i^B \ \mathbf{M}_a(i, i) + r_j^B \ \mathbf{M}_a(i, j) + r_k^B \ \mathbf{M}_a(i, k) \end{aligned} \quad (3.50)$$

The boxes are overlapping for the condition,

$$i \ s_1 + s_2 < \text{abs}(V(i)) \quad (3.51)$$

The other conditions with redefined s_1 and s_2 is given as,

$$\begin{aligned} i \ s_1 &= r_i^A \ \mathbf{M}_a(i, i) + r_j^A \ \mathbf{M}_a(i, j) + r_k^A \ \mathbf{M}_a(i, k) r_i^A \\ s_2 &= r_i^B \end{aligned} \quad (3.52)$$

The boxes are overlapping for the condition,

$$i \ s_1 + s_2 < \text{abs}(\mathbf{V} \cdot \mathbf{M}(i)) \quad (3.53)$$

The rest of the condition is summarized as different combinations of extension of the boxes in all three directions,

$$\begin{aligned} s_1 &= r_j^A \ \mathbf{M}_a(k, i) + r_k^A \ \mathbf{M}_a(j, i) \\ s_2 &= r_j^B \ \mathbf{M}_a(i, k) + r_k^B \ \mathbf{M}_a(i, j) \end{aligned} \quad (3.54)$$

$$\text{abs}(\mathbf{V}_k \cdot \mathbf{M}(i, i) - \mathbf{V}_j \cdot \mathbf{M}(k, i)) < s_1 + s_2 \text{ overlapping}$$

$$\begin{aligned} s_1 &= r_j^A \ \mathbf{M}_a(k, j) + r_k^A \ \mathbf{M}_a(j, j) \\ s_2 &= r_i^B \ \mathbf{M}_a(i, k) + r_k^B \ \mathbf{M}_a(i, i) \end{aligned} \quad (3.55)$$

$$\text{abs}(\mathbf{V}_k \cdot \mathbf{M}(j, j) - \mathbf{V}_j \cdot \mathbf{M}(k, j)) < s_1 + s_2 \text{ overlapping}$$

$$\begin{aligned} s_1 &= r_j^A \ \mathbf{M}_a(k, k) + r_k^A \ \mathbf{M}_a(j, k) \\ s_2 &= r_i^B \ \mathbf{M}_a(i, j) + r_j^B \ \mathbf{M}_a(i, i) \end{aligned} \quad (3.56)$$

$$\text{abs}(\mathbf{V}_k \cdot \mathbf{M}(j, k) - \mathbf{V}_j \cdot \mathbf{M}(k, k)) < s_1 + s_2 \text{ overlapping}$$

$$\begin{aligned} s_1 &= r_i^A \ \mathbf{M}_a(k, i) + r_k^A \ \mathbf{M}_a(j, k) \\ s_2 &= r_j^B \ \mathbf{M}_a(j, k) + r_k^B \ \mathbf{M}_a(j, j) \end{aligned} \quad (3.57)$$

$$\text{abs}(\mathbf{V}_i \cdot \mathbf{M}(k, i) - \mathbf{V}_k \cdot \mathbf{M}(i, i)) < s_1 + s_2 \text{ overlapping}$$

$$\begin{aligned} s_1 &= r_i^A \mathbf{M}_a(k, j) + r_k^A \mathbf{M}_a(i, j) \\ s_2 &= r_i^B \mathbf{M}_a(j, k) + r_k^B \mathbf{M}_a(j, i) \end{aligned} \quad (3.58)$$

$abs(\mathbf{V}_i \cdot \mathbf{M}(k, j) - \mathbf{V}_k \cdot \mathbf{M}(i, j)) < s_1 + s_2$ overlapping

$$\begin{aligned} s_1 &= r_i^A \mathbf{M}_a(k, k) + r_k^A \mathbf{M}_a(i, k) \\ s_2 &= r_i^B \mathbf{M}_a(j, j) + r_j^B \mathbf{M}_a(j, i) \end{aligned} \quad (3.59)$$

$abs(\mathbf{V}_i \cdot \mathbf{M}(k, k) - \mathbf{V}_k \cdot \mathbf{M}(i, k)) < s_1 + s_2$ overlapping

$$\begin{aligned} s_1 &= r_i^A \mathbf{M}_a(j, i) + r_j^A \mathbf{M}_a(i, i) \\ s_2 &= r_j^B \mathbf{M}_a(k, k) + r_k^B \mathbf{M}_a(k, j) \end{aligned} \quad (3.60)$$

$abs(\mathbf{V}_j \cdot \mathbf{M}(i, i) - \mathbf{V}_i \cdot \mathbf{M}(j, i)) < s_1 + s_2$ overlapping

$$\begin{aligned} s_1 &= r_i^A \mathbf{M}_a(j, j) + r_j^A \mathbf{M}_a(i, j) \\ s_2 &= r_i^B \mathbf{M}_a(k, k) + r_k^B \mathbf{M}_a(k, i) \end{aligned} \quad (3.61)$$

$abs(\mathbf{V}_j \cdot \mathbf{M}(i, j) - \mathbf{V}_i \cdot \mathbf{M}(j, j)) < s_1 + s_2$ overlapping

$$\begin{aligned} s_1 &= r_i^A \mathbf{M}_a(j, k) + r_j^A \mathbf{M}_a(i, k) \\ s_2 &= r_i^B \mathbf{M}_a(k, j) + r_j^B \mathbf{M}_a(k, i) \end{aligned} \quad (3.62)$$

$abs(\mathbf{V}_j \cdot \mathbf{M}(i, k) - \mathbf{V}_i \cdot \mathbf{M}(j, k)) < s_1 + s_2$ overlapping

Whenever we encounter particles not overlapping in any of the above-mentioned conditions, we have the *OBBs* of the two particles not overlapping. For example, two particles can have the same position along one axis, but they will not overlap if they are far from the length of their diameter along any of the remaining axes of the laboratory frame.

To calculate equilibrium pressure, we used a *NPT* ensemble. The details of the simulation technique are given in the next section.

3.3 NPT Simulation

To perform the NPT simulation, we start with a low-volume fraction [109]. We randomly distribute the particles within the simulation box, having a random orientation. The volume change step in each simulation step follows the movement step. For the movement step, we randomly chose the particles and translated them with the step length laying between $0 - s_T$, where s_T can be changed during the simulation such that the movement follows the acceptance of more than 30%. If it rises above forty percent, we increase the value of s_T through 5%. If the acceptance falls below 30%, we decrease s_T through 5%. The movement step is accepted according to the rule,

$$\exp(-\beta\Delta E) \quad (3.63)$$

where ΔE is the change in energy resulting due to movement. We follow a similar approach for the rotational step. Where each simulation step is followed by both translation and rotational steps performed over each particle on average. Following the particle movement, we do the volume change.

For the volume movement, we change the edge with the length v_{step} , such that,

$$V_n = \exp(\ln V_o \pm v_{step}) \quad (3.64)$$

Where v_{step} varies during the simulation run to optimize the movement's acceptance as it has been explained for the particle movement. For the volume change, we

scale the length of the box and shift the PBC accordingly. n_b as well as b_l is also calculated again following the sec. 3.2.2, according to L' , the changed edge length.

For $L' = V_n^{1/3}$, length scaling factor S_f is given as,

$$S_f = \frac{L'}{L} \quad (3.65)$$

For each x_i , position of the i^{th} particles are re-scaled as according to the new volume,

$$x'_i = S_f x_i \quad (3.66)$$

The acceptance probability is chosen as,

$$\exp\left(-(\Delta E + \frac{P}{k_B T}(V_n - V_o) - (N + 1) \ln(\frac{V_n}{V_o}))\right) \quad (3.67)$$

where ΔE is the change in energy after the volume movement. N is the total number of particles. In the case of rejection followed by equ. 3.67, lengths are scaled back by following the equation,

$$L' = L/S_f \quad (3.68a)$$

$$x'_i = x_i / S_f \quad (3.68b)$$

Now n_b and b_l are also changed to the previous value. Particles are reallocated in the cell each time we change n_b and b_l .

3.4 Variable shape simulation method

In the variable shape simulation method, we take only a few particles falling within the range 2 – 12 [112]. We define the box vector,

$$\mathbf{V}_B = \begin{bmatrix} \mathbf{b}_1 & \mathbf{b}_2 & \mathbf{b}_3 \end{bmatrix} \quad (3.69)$$

where $\mathbf{b}_x, \mathbf{b}_y, \mathbf{b}_z$ are the three edges of the box not necessarily orthogonal. In this way, we have the freedom to change both shapes as well as the size of the box.

The position of the particles within the distorted coordinate is defined as \mathbf{r}_n^f for the n^{th} particle. Within the distorted co-ordinate, we define the edge vectors \mathbf{V}_B^f given as,

$$\mathbf{V}_B^f = \begin{bmatrix} \mathbf{b}_1^f & \mathbf{b}_2^f & \mathbf{b}_3^f \end{bmatrix} = \begin{bmatrix} |\mathbf{b}_1| & 0 & 0 \\ 0 & |\mathbf{b}_2| & 0 \\ 0 & 0 & |\mathbf{b}_3| \end{bmatrix} \quad (3.70)$$

We define \hat{V}_B as,

$$\hat{V}_B = \begin{bmatrix} \hat{b}_1 & \hat{b}_2 & \hat{b}_3 \end{bmatrix} \quad (3.71)$$

Position of the particles within the laboratory frame \mathbf{r}_n can be written as,

$$\mathbf{r}_n = \hat{V}_B \cdot \mathbf{r}_n^f \quad (3.72)$$

. \mathbf{r}_i^f is written as,

$$\mathbf{r}_n^f = \hat{V}_B^{-1} \cdot \mathbf{r}_n \quad (3.73)$$

Inter-particle interaction is calculated using \mathbf{r}_n . At the same time, the periodic boundary condition is applied over \mathbf{r}_m^f .

The periodic boundary condition is implemented as,

$$x_n^f : \quad x_n^f = \begin{cases} x_n^f - |\mathbf{b}_1| & x_n^f > |\mathbf{b}_1| \\ x_n^f + |\mathbf{b}_1| & x_n^f < 0 \end{cases} \quad (3.74)$$

Interaction between the particles n, m , connected through periodic boundary condition is $x_n^f - x_m^f$.

$$x_n^f - x_m^f : \quad x_n^f - x_m^f = \begin{cases} x_n^f - x_m^f + |\mathbf{b}_1| & x_n^f - x_m^f < 0 \\ x_n^f - x_m^f - |\mathbf{b}_1| & x_n^f - x_m^f > 0 \end{cases} \quad (3.75a)$$

Such a periodic boundary condition is called the shifted periodic boundary condition or simply *SPBC*. In the variable shape simulation method, we do not use any cell division of the box. As there are only a few particles, the calculation of interaction on each particle does not lead to any loss of computational efficiency.

We perform volume movement in the same way as we do in *NPT* simulation. We generate a random vector $\mathbf{v} = v_{step}(x_v \hat{i} + y_v \hat{j} + z_v \hat{k})$ with random orientation and size. Where the length of the vector is taken within the range $[0, v_{step}]$. We randomly select any vector among all the three $\mathbf{b}_1, \mathbf{b}_2, \mathbf{b}_3$ and do the volume movement following the equation,

$$\mathbf{b} = \mathbf{b} + \mathbf{v} \quad (3.76)$$

where new box vector is defined as, \mathbf{V}'_B and the new volume is calculated as,

$$V_n = |\mathbf{V}'| \quad (3.77)$$

While the previous volume is given as $V_o = |\mathbf{V}|$. Now, we follow the same acceptance rule as given in the *NPT* simulation section. The position of the box is re-scaled within the distorted coordinate.

3.4.1 Re-scaling the position of the particles in a floppy box, following the volume movement

Box vector defined in distorted coordinate \hat{V}_B^f , will not change with the shape change as it is defined along the edge of the box itself. Although the edge length will change from $|\mathbf{b}|$ to $|\mathbf{b}'|$, as in the case of normal *NPT* simulation (constant shape simulation). S_f is defined as,

$$S_f = \mathbf{b}'/\mathbf{b} \quad (3.78)$$

where the volume movement is performed over any randomly chosen $\mathbf{b} : \mathbf{b} \in \mathbf{b}_1, \mathbf{b}_2, \mathbf{b}_3$. For each x_n^f , position of the n^{th} particles are re-scaled as according to the new volume,

$$x_n'^f = S_f \ x_n^f \quad (3.79)$$

All the positions \mathbf{r}_n in the laboratory frame are calculated again by using $\mathbf{r}_n'^f$ with the help of eq. 7.1.

3.4.2 Lattice reduction technique: Avoiding extreme shape distortion of the simulation box

A cell of a crystal can be represented an infinite way. In some cases, the shape is represented as distorted enough to bring unnecessary complications. We use the lattice reduction technique to avoid counting the same crystal structure multiple times. For the lattice reduction, we minimize the surface formed by the lattice vector $\mathbf{b}_1, \mathbf{b}_2, \mathbf{b}_3$ as well as keep the angle between the lattice vectors constant. We chose the vector among the given twelve vectors such that it has a minimum surface. New vectors are again generated by using the previously generated vector as the initial vector.

$$\begin{aligned} & \{\mathbf{b}_1 \pm \mathbf{b}_2, \mathbf{b}_2, \mathbf{b}_3\} \quad \{\mathbf{b}_1 \pm \mathbf{b}_3, \mathbf{b}_2, \mathbf{b}_3\} \\ & \{\mathbf{b}_1, \mathbf{b}_2 \pm \mathbf{b}_1, \mathbf{b}_3\} \quad \{\mathbf{b}_1, \mathbf{b}_2 \pm \mathbf{b}_3, \mathbf{b}_3\} \\ & \{\mathbf{b}_1, \mathbf{b}_2, \mathbf{b}_3 \pm \mathbf{b}_1\} \quad \{\mathbf{b}_1, \mathbf{b}_2, \mathbf{b}_3 \pm \mathbf{b}_2\} \end{aligned} \tag{3.80}$$

In this way, we have similar crystal structures represented as the unit cell, with shapes having minimal distorted form. To prevent the box from extreme deformation, we also impose restrictions over the angle formed between the individual \mathbf{b} . The angle is always kept within the range $[30^\circ, 150^\circ]$. Box edge lengths $|\mathbf{b}|$ are always kept more than the particles' size.

3.5 Floppy simulation method

A floppy simulation method is similar to the variable shape simulation method, where we change the shape of the box along with the volume. We apply the shifted periodic boundary condition in the same way as has been discussed in the previous section. However, due to the large number of particles, we used cell division methods

to increase the computational efficiency. While the cell is defined within the distorted co-ordinate of the box such that,

$$n_b^1 = \text{floor}(\mathbf{b}_1/\sigma) \quad (3.81\text{a})$$

$$b_l^1 = \mathbf{b}_1/n_b^1 \quad (3.81\text{b})$$

In the liquid state, to avoid extreme distortion, we impose restrictions over the angle between the axes as well as the length, as discussed in the previous section. To simplify the crystal structure, we use the lattice reduction technique. Generally, we take the structure in bulk form from the variable shape simulation methods and put the crystal inside an appropriate box with the same shape and size. Now, we simulate the system at constant pressure and temperature to check its stability. Floppy simulation can also be used to calculate the free energy of the crystal structure, as discussed in the next chapter.

3.6 Prediction of the crystal structures

We start the variable shape simulation method at low pressure. The pressure slowly increases with the simulation time. While temperature is kept constant, in this way, we can achieve high pressure of up to $P/k_B T = 200$ for a particular temperature. We extend the unit cell to verify the crystal structures along all three box edges. Then, we calculate $g(r)$. Potential energy is also calculated. Calculating the Strienhardt parameter, q_6 , and q_4 can also confirm crystal structures.

Once all the crystals predicted by Variable shape simulation methods are distinguished, we take the bulk crystal structure and check the stability of the structure by putting the same into a floppy simulation box.

Once we have a phase confirmed for stability by doing a floppy simulation, we can take the same $V - T$ value corresponding to the $p - T$ point and run a BCD (NVT). In some cases, we start with a seed, especially if the system is unable to overcome meta-stability. In this way, we predict structures and calculate the stability as well as the kinetics of the system.

3.7 Calculating cluster size distribution

In the case of a limited number of bonding achieved by using patches, the kinetics gets slower due to confined bonding volume caused by directionality. In such a case, it can take an indeterminate time for a NVT ensemble to reach equilibrium, which can bring uncertainty in the cluster size distribution even if the system is left to simulate for a prolonged time to achieve equilibrium [113]. For the case, we used semi-grand-canonical simulation; *SGMC* as explained [113]. The details of the simulation are given in the section below.

3.7.1 Semi-grand canonical monte-carlo simulation with parallel tempering and umbrella sampling

At high temperatures and low pressure, cluster gas formation occurs within the fluid regime of the system. Specifically, patchy particles that have low β_{att} and the attractive part of the second virial coefficient, even at low temperatures, can get stuck in the meta-stable state. In such a case, calculating the cluster size distribution can not generate accurate results while using NVT simulation. For this purpose, we use a semi-grand canonical ensemble.[113] To simulate the system, we take the system at a particular chemical potential $\mu/k_B T$, temperature $k_B T/u$, and pressure

$P/k_B T$, where u is the bond energy of a single bond. We randomly select the particle and put a new particle in the surroundings within the bond $d < r < d + \epsilon$ range. Where d is the hardcore range and ϵ is the softcore attractive potential range. If the inserted particle falls within the range of more than one particle, then the step is rejected with the probability $1/c$, where c is the number of particles falling within the range of the bond of the particle being inserted. Particle deletion also takes place by randomly choosing the particle. In this way, we change the cluster size. The acceptance rule for the particle insertion and deletion is given by,

$$\begin{aligned} & \text{acceptance}(c_S \rightarrow c_S + 1) \\ &= \min \left[\frac{c_S}{(c_S + 1)\Lambda^3} v \exp [-\beta(U(\mathbf{r}^{c_S+1}, \hat{n}^{c_S+1}) - U(\mathbf{r}^{c_S}, \hat{n}^{c_S}) - \mu)], 1 \right] \end{aligned} \quad (3.82)$$

$$\begin{aligned} & \text{acceptance}(c_S + 1 \rightarrow c_S) \\ &= \min \left[\frac{(c_S + 1)\Lambda^3}{c_S} \frac{v}{c_S} \exp [-\beta(U(\mathbf{r}^{c_S}, \hat{n}^{c_S}) - U(\mathbf{r}^{c_S+1}, \hat{n}^{c_S+1}) - \mu)], 1 \right] \end{aligned} \quad (3.83)$$

where v is the volume of the shell chosen to insert the particle, for the c_S cluster size it would be $n c_S$, which eventually appears in the acceptance criteria of the semi grand canonical insertion step (see eq. 3.83 and 3.82). To remove the biases in the insertion due to the overlap of the insertion regions, we reject an insertion step with a probability $\frac{k-1}{k}$. Such that the insertion point is shared by the insertion region of the k number of particles. All the movements leading to the breakage of the cluster in smaller sizes are not allowed. Deletion and insertion leading to the breakage of clusters are also not allowed. In this way, we simulate individual clusters placed

within the simulation box, kept at constant volume and temperature. In SGMC simulation, the probability of finding a cluster of size c_S^m and c_S^n is given as,

$$\frac{p(c_S^m)}{p(c_S^n)} = \frac{Z_m}{Z_n} e^{[(\mu(m-n))]} \quad (3.84)$$

3.7.2 Umbrella sampling

Umbrella sampling is a useful technique where we take samples from the region that is relevant to the average calculation of the quantity [109]. All the sample space is divided into small windows. We simulate each window simultaneously such that the system must lie within the window, including the boundary of the window. After simulating each window, we compile all the windows to generate the final data. The process can be understood better with the example of its application in SGMC simulation. We simulate many clusters simultaneously and independently from each other within the same simulation box. We make the window in terms of cluster size c_S , where it is allowed to vary the size within the range $[c_S, c_S + 1]$. The compilation of the results obtained from the different bins has been discussed in the latter section, where we calculate cluster size distribution as well as the free energy of a system at a particular temperature and ϕ .

3.7.3 Parallel tempering

In parallel tempering[109], we simulate the same system at different temperatures simultaneously and independently of each other. We exchange the temperature of the systems following some acceptance rule. In this way, we try to go in high-energy regions so that the system can cross the energy barrier or meta-stability. Such a

scheme is useful for umbrella sampling, where it can be applied in each system simulating different windows.

For example, we keep a copy of the same cluster at different temperatures independent of each other. We do not leave the window for any system placed at different temperatures. We exchange the temperature of the clusters having the same size. The acceptance rule is given as,

$$\text{acceptance}(\beta \rightarrow \beta')$$

$$\min [1, \exp [(\beta' - \beta)(U - U')]] \quad (3.85)$$

Or in terms of the number of bonds n_b it can be written as,

$$\text{acceptance}(\beta \rightarrow \beta')$$

$$\min [1, \exp [(\beta' - \beta)(n_b - n'_b)]] \quad (3.86)$$

The two systems are running at temperatures β and β' , scaled with the bond strength u .

3.8 Calculation of phase-diagram using thermo-dynamic integration

To compute the phase diagram, we need to know the chemical potential of different phases defined in $p - T$ diagram. There are various schemes for calculating μ ; a

few of them are discussed in the following section. Once we can find out μ , the coexistence point can be defined as (p, T) where different phases have the same μ .

3.8.1 Equation of state for spheroidal colloids

There are no analytical expressions for the equation of state for the system of spheroids, as it is given in the case of spheres. Though one can write the same in terms of Virial expansion given as,

$$P = \rho + \sum_n B_n \rho^n \quad (3.87)$$

Where B_n are virial coefficients. For the isotropic case, we have B_n given by,

$$B_n = \frac{1-n}{n!V(4\pi)^n} \int \dots \int F_n d\hat{n}_1 d\hat{n}_2 \dots d\hat{n}_n d\mathbf{r}_1 d\mathbf{r}_2 \dots d\mathbf{r}_n \quad (3.88)$$

where F_n is the Mayer-f function given as,

$$F_n = \sum_{\{\ast\}} \prod_{i < j}^n f_{1,j} \quad (3.89)$$

where $\{\ast\}$ indicates sum over all star-integrals.

Now the free energy and chemical potential are given by Onsager and shown as [114],

$$\frac{F}{Nk_B T} = \ln(\Lambda^3 \rho) - 1 + \sigma(\psi) + \sum_{n=2}^{\infty} \frac{1}{(n-1)} B_n \rho^{n-1} \quad (3.90)$$

$$\frac{\mu}{k_B T} = \ln(\Lambda^3 \rho) + \sigma(\psi) + \sum_{n=2}^{\infty} \frac{n}{(n-1)} B_n \rho^{n-1} \quad (3.91)$$

In the case of the isotropic phase, we have $\sigma(\psi) = 0$.

3.8.2 Free energy calculation for the fluid regime

We used thermodynamic integration to calculate the free energy of the fluid phase [115]. We look for a single point (P, T) in the phase diagram corresponding to the fluid phase. We calculate the average ϕ for such a system. NVT simulation is done at the corresponding constant $\phi(N, V)$ and T .

The free energy of the fluid is given by,

$$\frac{F}{Nk_B T} = f_{HC}/Nk_B T + \int_0^{\beta'} \langle u \rangle_{VT} d\beta \quad (3.92)$$

where HC is the hard core contribution to the free energy corresponding to the isotropic orientation of spheroids[116],

$$\frac{f_{HC}}{Nk_B T} = \ln(\Lambda^3 \rho) - 1 + \sum_{n=2}^{\infty} \frac{1}{(n-1)} B_n \rho^{n-1} \quad (3.93)$$

where ρ is the number fraction. B_n is the n^{th} virial coefficient computed by using MC integration, up to five terms.

To compute the integral given in the equation, 3.92, we run several NVT system, at different value of β . We use numerical integration like the Trapezoidal rule to compute the integral.

3.8.3 Free energy of the cluster gas using SGMC

We used semi-Grand canonical Monte Carlo (SGMC) [117, 118] simulation to compute the free energy of the cluster gas at very low ρ and $pd^3/k_B T$ regime. In this simulation, we treat fluid as the gas of clusters of size n . The total number of

particles N is given by,

$$N = N_1 + 2N_2 + 3N_3 + \dots \quad (3.94)$$

where N_1, N_2, \dots are the number of clusters with size 1, 2, ... respectively. It can be rewritten as,

$$\rho = \rho_1 + 2\rho_2 + 3\rho_3 + \dots \quad (3.95)$$

where ρ_1, ρ_2, \dots are the number fraction of the cluster of size n .

Free energy of the cluster gas is given by,

$$\frac{A}{Nk_B T} = \frac{1}{N} \sum_{n=0}^{\infty} N_n \left[\ln N_n - 1 - \ln(Z_n) + \frac{f_{HE}}{k_B T} \right] \quad (3.96)$$

where f_{HE} is the hard core contribution to the free energy given as,

$$\frac{f_{HE}}{k_B T} = \sum_{n=2}^{\infty} \frac{1}{(n-1)} B_n \rho^{n-1} \quad (3.97)$$

Z_n is the partition function for a cluster of size n . It can be written as,

$$Z_n = \frac{1}{(4\pi)^n \lambda^{3n} n!} \iint e^{-\beta U(\mathbf{r}^n, \Omega^n)} d\mathbf{r}^n d\Omega^n \quad (3.98)$$

To compute Z_n , we used SGMC simulation as discussed in the section 3.7.1. For efficiency, we performed umbrella sampling, wherein, in each window, the number of particles could be either n or $n+1$. Particle deletion and insertion were done to keep the cluster inside the corresponding window. P_{n+1}, P_n [119] is the probability of finding a cluster of size $n+1$ and n respectively within each window and is related to the partition function as

$$\frac{P_{n+1}}{P_n} = \frac{Z_{n+1}}{Z^n} e^{\beta \mu} \quad (3.99)$$

where $e^{(\beta\mu)}$ is the fugacity. ρ_n is given by,

$$\rho_n = \frac{\rho_1^n}{Z_1^n} Z_N \quad (3.100)$$

Z_1 can be computed as $Z_1 = \Lambda^3 V$. Using eq. 3.99 we computed ρ_n/ρ_1^n . In this way, we express each term in eq. 3.95, in terms of ρ_1 . Using the plot between ρ vs. ρ_1 we computed the desired value of ρ_1 for a particular fixed value of ρ . Finally, by using eq. 3.96 and 3.97, we computed the free energy of the cluster gas distribution.

3.8.4 Plotting Chemical potential vs pressure for liquid, at constant T

Following the free energy calculation discussed in the previous section. We compute chemical potential following the equation,

$$\frac{\mu}{k_B T} = \frac{F}{N k_B T} + \frac{P}{k_B T \rho} \quad (3.101)$$

To compute $\mu - P$, we use the integral given as,

$$\frac{\mu}{k_B T} = \frac{\mu_{P'}}{k_B T} + \int_{P'}^P \frac{1}{\rho'(P')} dP' \quad (3.102)$$

Where P' is the initial pressure. We keep on changing P on both sides of the value of P' and get the plot for the $\mu - P$ within the desired range. To compute the integral, we get the equation of state at a particular T by running several NPT simulations at different P . We use least square curve fitting to fit a curve over $P - V$ for the particular T . We integrate 3.102 using the $P - V$ curve.

3.8.5 Free energy of solid using Einstein crystal method

We used the Frenkel-Ladd method to calculate the free energy of the solid phases, and the monolayer [120, 121]. We generated the configuration using the floppy box method, thereby defining the corresponding Einstein crystal. The effective potential can be expressed as,

$$U_{effective} = \lambda U_{sol} + (1 - \lambda)(U_{sol} + U_{et} + U_{eo}) \quad (3.103)$$

where, U_{sol} is the potential defined by eq. 7.2, which corresponds to the present model. U_{et} and U_{eo} is given by,

$$U_{et} = \lambda \frac{1}{N} \sum_{i=0}^N (r_i - r_{oi})^2 \quad (3.104)$$

with $(r_i - r_{oi})$ being the displacement of i^{th} particle from the equilibrium position and λ is the spring constant.

$$U_{eo} = \lambda \frac{1}{N} \sum_{i=0}^N (1 - \cos(\theta_i)) \quad (3.105)$$

where θ_i is the orientation of the i^{th} particle measured from the equilibrium orientation.

The free energy of the solid phase is given by,

$$\frac{A}{Nk_B T} = U_{tr} + U_{or} + \Delta U_\lambda + U_{Lattice} \quad (3.106)$$

where U_{tr} and U_{or} [122] is the translational and orientational energy corresponding to the ideal Einstein crystal.

$$U_{tr} = -\frac{1}{N} \ln \left[\left(\frac{1}{\Lambda_{tr}} \right)^{3N} \left(\frac{\pi}{\beta \lambda_{max}} \right)^{3(N-1)/2} (N)^{3/2} \left(\frac{V}{N} \right) \right] \quad (3.107)$$

where $\Lambda_{tr} = h/\sqrt{2\pi k_B T}$, $\beta = 1/k_B T$.

$$U_{or} = -\ln \frac{1}{\Lambda_{or}} \frac{1 - e^{-2\beta \lambda_{max}}}{2\beta \lambda_{max}} \quad (3.108)$$

where $\Lambda_{or} = h^2/(8\pi^2 I k_B T)$, the choice of Λ_{or} and Λ_{tr} is arbitrary and is related to each other by expression $\Lambda_{tr}\Lambda_{or} = d^3$.

ΔU can be computed as,

$$\Delta U = \int_0^{\lambda_{max}} \left\langle \frac{dU_{et}}{d\lambda} \right\rangle d\lambda + \int_0^{\lambda_{max}} \left\langle \frac{dU_{eo}}{d\lambda} \right\rangle d\lambda \quad (3.109)$$

$U_{Lattice}$ is the potential energy corresponding to the Hamiltonian in the absence of the reference potential.

3.8.6 Plotting Chemical potential vs pressure for solid, at constant T

We use the same method to plot $\mu - P$ as given for the fluid phase. However, it remains nearly the same for a small range of change of P . Therefore, we don't need to find the equation of state for a solid in most cases. However, in such a case, accuracy can be compromised if ρ of the crystal phase changes drastically with the change of P . For the system, we need to run the NPT simulation at different P by putting the crystal in a floppy box and applying the shifted boundary condition.

3.8.7 Thermodynamic integration using *NPT* simulation for a one component system

Once we find the coexistence point by plotting $\mu - P$ graph for different phases at the same temperature T . We use the calculated (P, T) value as the initial point to get the phase lines by applying Gibbs-Duham integration or simply GD integration.

$$\frac{dp}{dt} = \frac{1}{T} \frac{h_I - h_{II}}{v_I - v_{II}} \quad (3.110)$$

where h_I , h_{II} and v_I , v_{II} are the molar enthalpy and volume per particle of the two phases, respectively. We simultaneously simulate two phases across the line and generate the line of coexistence. We keep on changing P, T on the line following eq. 3.110, while solving by using R-K-four method.

Chapter 4

**Enhancement in the diffusivity of
Brownian spheroids in the
presence of spheres**

Abstract

In the present study, we have extended the simulation technique Brownian cluster dynamics (BCD) to analyze the dynamics of the binary mixture of hard ellipsoids and spheres. The shape-dependent diffusional properties have been incorporated into BCD using Perrin's factor and compared with the analytical results of a one-component ellipsoidal system. We have investigated pathways to enhance the diffusivity of spheroids in the binary mixture by manipulating the phase behavior of the system by varying the fraction of spheres in the binary mixture. We show that at low volume fraction, the spherical particles have a higher diffusion coefficient than the ellipsoids due to the higher friction coefficient. However, at a higher volume fraction, we show that the diffusion coefficient of the ellipsoids increases irrespective of the aspect ratio due to the anisotropic shape.

4.1 Introduction

Colloidal systems have been investigated for over a century, as these systems can mimic atomistic phenomena and can also be tracked on a single particle scale owing to their micro-meter size. The system of spherical particles has been one of the most extensively studied systems, both experimentally and theoretically. The phenomena being investigated include transient clustering, jammed system, crystal formation etc [123, 124, 125, 126, 127, 128, 129, 130]. Recent experimental advancements have made it possible to synthesize colloids of different shapes [131, 132, 133, 134]. Among these particles the anisotropic ellipsoidal colloidal particle has attracted a lot of interest [135, 136, 137, 138, 139, 140, 132, 133, 141]. These ellipsoidal particles display a wide variety of phases which include nematic phase, crystallization, smectic phase, etc [142, 143]. Recently, the dynamics of hardcore ellipsoidal particles have revealed 2 types of glass transition, repulsive glass in terms of translation [144], and orientational or liquid glass in terms of rotational jamming [135]. To simulate the liquid glass, the ellipsoidal particles have been simulated by introducing a rough wall in the system to avoid isotropic-nematic transition.

In simulations, the binary system containing hard spheroids has been studied extensively. However, most of these works are focused on the study of phase behavior related to nematic ordering. These studies include the binary system of hard rods-spheroids and spheroids-plates. The binary system of spheres and spheroids, with the combination of different shapes and sizes, has been analyzed by using density functional theory. In this work, we have considered the binary system of colloids with spheres and spheroids. We used BCD to study the diffusivity of the binary colloidal system, both in dilute and high concentration limits up to the nematic phase. Our study includes the binary system of spheres mixed with spheroids, showing

a transition from an isotropic phase to a nematic-isotropic phase for the spheroid particles.

To study the phase properties and dynamics by simulation a variety of techniques have been proposed which include molecular dynamics [143, 145, 20, 146], Monte-Carlo method [147, 139, 148], Langevin dynamics [127, 96] etc. The Brownian cluster dynamics(BCD) is a simulation technique primarily developed to study the structure, kinetic and dynamical properties of the system undergoing both reversible and irreversible aggregation on a lattice [149, 150], later extending it to off-lattice spherical particles with isotropic square well potential for monomeric (with only one type of particle) [151, 152, 129, 153, 154] and binary colloidal systems [155, 156]. Recently, BCD was modified to simulate spherical patchy particles [99, 100, 157, 158] using the Kern-Frenkel potential [147]. Spherical particles were used extensively in these simulation models as it is computationally easy to check the overlap condition due to its symmetry. BCD has the advantage that it can simulate the dynamics of clusters in two ways: by individual monomer diffusion within the bonds, which is also known as the Rouse model, and by diffusing the center of mass of the cluster with a diffusion coefficient inversely proportional to the cluster radius known as Zimm dynamics. It was already shown that the structure, kinetics, and dynamics of BCD with the Rouse model agree with Event-driven Brownian dynamics (EDBD) for the case of square-well potential [97]. BCD later incorporated the patchy particle model, and the method was validated by showing the correct static and dynamic properties of a single polymer chain [99]. The aggregation of the lysozyme protein was mimicked using spherical particles with 2 patch irreversible bonds with an overlapping isotropic reversible square well potential [100, 157]. Glucose isomerase protein was successfully modeled by making the patches reversible along with the isotropic square-well potential using BCD [158]. It was also shown that introducing

a particle with specific interaction sites leads to either enhancement or retardation in the aggregation rate of the cylindrical clusters [157], which is considered **to be** the reason for Alzheimer's disease.

In the present work, we have extended BCD to include hard spheroids. Within the given framework of BCD, we study the dynamics of the system by defining the physical time as equal to the time taken by a particle to diffuse its own diameter in the infinitely dilute limit (diffusion of single particles suspended in the fluid). In BCD, we do not solve the equation of motion. Instead, the particles are moved in a random direction with a fixed translational and rotational step length. We mimic the diffusive motion of a single spheroid by implementing the friction coefficient in terms of translational and rotational step length. We have considered the shape-dependent friction of spheroids given by Perrin's factor [103] for the slip boundary condition. This way, we have presented a relative analysis of the diffusivity of the colloidal suspension. More insights about the simulation technique have been given in the later section. Initially, we studied the system with only one kind of particle (monomeric). The diffusion coefficient of a single ellipsoid obtained using BCD agrees with the analytical calculation. The iso-diffusivity curve for both prolate and oblate ellipsoids at different volume fractions shows the swallow-like shape for the translational component as predicted by event-driven Brownian dynamics simulation. For the one-particle system, at higher concentrations, the translational diffusivity of the colloidal spheroids increases with shape anisotropy when compared to the same volume fraction of spheres. At low concentrations, translational-diffusivity of the spheroids has been found to decrease with increasing shape anisotropy of the particles. On the other hand, rotational diffusivity has been found to decrease with increasing shape-anisotropy in both the higher and lower concentrations. In the binary mixture of

spheres and spheroids, we found Perrin's friction factor playing an essential role behind the observed enhancement in the translational diffusivity of the spheroids, with an increasing fraction of spheres. At high concentrations, the diffusivity of spheroids has been found to decrease as we increase the fraction of spheres. On the other hand, the rotational diffusivities have been found to increase as we increase the fraction of spheres in both high and low-concentration regimes. Here, we found that the destruction of nematic ordering around spheres plays an essential role in the observed decrease in translational diffusivity of spheroids at high concentrations. Spheroids around the spheres get stuck due to the local disorder despite having the presence of global nematic ordering. For the rotational diffusivity, we observed a minute enhancement until the nematic order parameter of the system became lower than its defined isotropic-phase limit. The rotational diffusivity is enhanced significantly as the system tends towards the isotropic phase, with more and more spheres in the system. For the spheroid having a shape less deformed from the shape of spheres, we have not observed any nematicity. The translational diffusivity of such spheroids has been found to depend on the packing at higher concentrations. Meanwhile, we do not observe any change in the rotational diffusivity for the same spheroids at the same concentration as we increase the fraction of spheres in the system.

The paper is arranged as follows: in section 6.2, we give a detailed explanation regarding the inclusion of asymmetrical particles into the simulation technique Brownian cluster dynamics. We also explain how we have incorporated the friction equation derived by Perrin et al. [103], thereby setting the definition of time. In section 6.3, we have discussed the effect of step size to mimic Brownian dynamics as well as compared the result of monomeric ellipsoidal particles to the analytical equation derived by Perrin et al. for the single particle diffusion. The shape of the iso-diffusivity lines of BCD and EDBD shows a similar trend both for translational and rotational

diffusion. We have shown that the translational diffusivity in a binary system consisting of sphere and ellipsoidal particles for both prolate and oblate depends on the aspect ratio, and the rotational diffusion depends on the nematic transition. The size of the nematic clusters has also been approximately calculated [159]. We have also reported a nematic to isotropic transition for different fractions of the sphere as a function of volume fraction in a binary system. This is followed by the conclusion in the section 4.4.

4.2 Simulation technique

We have modified BCD to incorporate spheroid (prolate and oblate) particles. Dynamics is discussed in the section 3.8.1 of chapter 2. Here, we give a brief detail about the simulation technique. We define a spheroid by the aspect ratio $p = a/b$, where a and b are the lengths of the semi-major (symmetry axis) and semi-minor (perpendicular to the symmetry axis) axes, respectively. We represent an ellipsoid of revolution (ER) with the orientation of a unit vector \hat{n} , along the symmetry axis and the center of mass position vector. In the present work, we have considered $N = 600$ particles in a cubic simulation box of size L , with periodic boundary conditions [160]. The ellipsoids with different p considered in the present work have the same volume, which is equal to the volume of a sphere with diameter $d = 1$, such that $d = (ab^2)^{1/3}$. The corresponding volume fraction is defined as $\phi = N \frac{\pi d^3}{6L^3}$.

As the initial configuration, we create a random distribution of both the position and orientation of the ellipsoidal particle. We randomly select $2N$ ER for the movement step. The selected particle either undergoes a translational or rotational displacement in a random direction, with a probability of half. This ensures that the translational and rotational motion of ellipsoids happens in an uncorrelated manner

[97, 99]. The rotational, as well as translational displacement of ellipsoids happens in a random direction with a predefined step length. Each movement process is followed by an overlap condition applied to check the overlap of the hard-core ellipsoidal particles. The movement step is only accepted if there is no overlap with other ellipsoidal particles.

For calculating the overlap condition of the ellipsoidal particles, we define a rectangular box enclosing the ER, with length and breadth twice the semi-major and semi-minor axis, respectively. If the oriented bounding box (OBB) [161] of two adjacent ellipsoids overlap, then we employ the method of ellipsoidal contact function (ECF)[110] to verify the overlap of the particles. After we have attempted to translate or rotate $2N$ particles, we increment the simulation time t_{sim} by one unit, which is the number of times we have attempted to translate and rotate all the particles in the system.

To achieve a particular volume fraction, ϕ , with the random initial condition, we distribute 600 particles in a large simulation box or, in other words, at very low ϕ . We progressively reduce the size of the simulation box from all sides gradually till the desired ϕ is achieved. During each compression step, we relax the system before we undertake the next compression procedure.

4.3 Results

4.3.1 Dynamics of one component spheroids

In BCD, step size plays a major role in deciding the correct dynamics of the system. The step size has to be small to attain the correct diffusion coefficient. Large step sizes lead to a lot of rejection in the movement step due to the overlap condition,

which leads to the diffusion coefficient being smaller than the expected value. To understand the effect of step size S_T we have calculated the long-time diffusion coefficient $D_T/D_T^o = \frac{\langle R^2 \rangle/d^2}{t_{Phy}/t_0}$ for the prolate ellipsoidal particle in $\phi = 0.5$ and $p = 4$, with respect to step size as shown in Fig. 4.1. The mean square displacement (MSD) is defined as $\langle R^2 \rangle = \frac{1}{N} \sum_{i=1}^N (r_i(t) - r_i(0))^2$ where r_i is the position of the center of mass of the ellipsoidal particle as a function of time. In Fig. 4.1, we observe that D_T/D_T^o increases with reducing step size and converges to 0.18. The distance between the ellipsoids in the equilibrium configuration for $\phi = 0.5$ is very small. The step size we choose should be less than the nearest neighbor distance between particles for a particular ϕ . For step sizes larger than the inter-particle distance, there will be more rejections in the movement step due to the collision with the nearby ellipsoidal particle. Thus, the center of mass of many particles will not be able to diffuse, leading to D_T/D_T^o smaller than the expected value. To avoid this problem, if we continue to reduce S_T , the physical time over which we can probe our system will also reduce according to the equation. 3.10. As a compromise, we have chosen a step size whose diffusion coefficient is accurate within 10% of the real value, where the step size $S_T = 0.005$ is kept constant for all the systems reported in the present work, irrespective of the aspect ratio. We observe that the long-time diffusion coefficient D_T^{\parallel}/D_T^o and D_T^{\perp}/D_T^o follow the same trend as the center of mass diffusion coefficient for the oblate and prolate particles.

In Fig. 4.2, we have plotted the mean square displacement of the prolate ER as a function of time at $\phi = 0.5$, aspect ratio $p = 4$, and step size $S_T/d = 0.005$. We also plotted the MSD along the parallel $\langle R_{\parallel}^2 \rangle$ and $\langle R_{\perp}^2 \rangle$ perpendicular to the symmetry axis of the ellipsoids as a function of time. We know that in the case of molecular dynamic simulation, short-time dynamics always lead to ballistic motion, but in the case of BCD, even the short-time dynamics undergo Brownian motion.

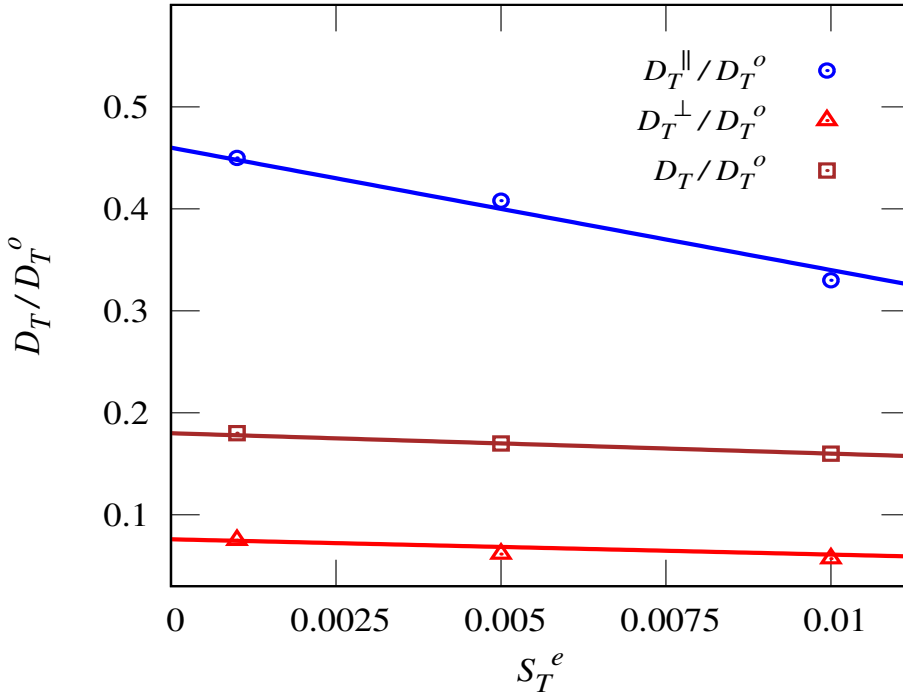


FIGURE 4.1: The effect of step size (S_T) of the center of mass of ER with D_T^{\parallel}/D_T^o (circles), D_T^{\perp}/D_T^o (triangles) and the resultant D_T/D_T^o (squares) are shown for ER with $p = 4.0$ at $\phi = 0.5$. The solid lines are fit to the points. The points can be seen converging to a particular value, given by $D_T^{\parallel}/D_T^o \approx 0.46$, $D_T^{\perp}/D_T^o \approx 0.075$, and $D_T^e/D_T^o \approx 0.18$.

This can be observed in Fig. 4.2, as the slope of MSD remains unity even for short-time diffusion. After a long time $t_{Phy}/t_0 > 8$, the MSD again attains a slope of unity but with a slightly smaller diffusion coefficient due to the hindrance of the other ellipsoidal particles, as the volume fraction is finite. We also observe that the MSD along the perpendicular direction to the symmetry axis diffuses slower than the parallel direction, as the friction coefficient along the perpendicular direction is larger compared to the parallel direction.

We know that the diffusion of the ellipsoidal particle should depend on the geometry of the particle. At a lower volume fraction $\phi = 0.002$, the number of collisions with neighboring particles will be minimal, and the ellipsoidal particle will diffuse like

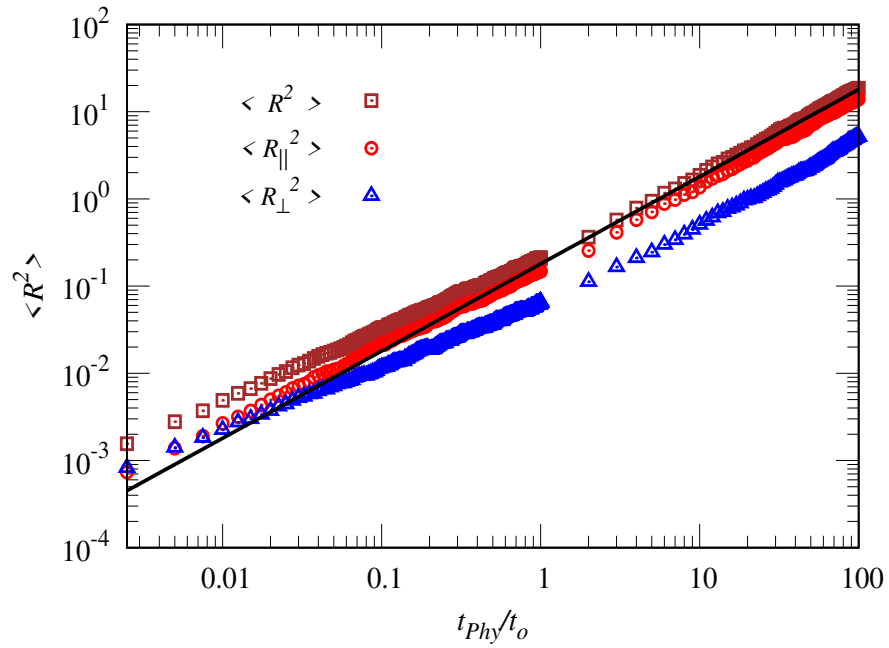


FIGURE 4.2: The MSD of the center of mass of the ER $\langle R^2 \rangle/d^2$ (square) is plotted as a function of t_{Phy}/t_o calculated with $S_T = 0.005$ for $p = 4$ and at $\phi = 0.50$. The MSD is resolved into the parallel (circle) and perpendicular (red points) direction of the director. They converge to a slope of unity as shown by the solid lines.

a single non-interacting ER. In Fig. 4.3(a) we have plotted $D_T^{\parallel}/D_T^{\circ}$, D_T^{\perp}/D_T° and D_T/D_T° for $\phi = 0.002$, as a function of the aspect ratio p , as obtained from the simulation. It is compared with the analytical equation of the single ER diffusion coefficient calculated using equation 3.16, 3.17, and 3.18, and we observe good agreement with the simulation result for infinite dilution. We also observe that D_T/D_T° decreases with increasing shape anisotropy of the ER, as the friction coefficients for prolate and oblate particles increase along the perpendicular and parallel direction according to eq. 3.17. In Fig. 4.3(b), we have plotted the rotational diffusion coefficient for both prolate and oblate ellipsoidal particles. We calculate the mean squared angular displacement of the ellipsoidal particle $\langle \theta_1^2 \rangle$, where θ_1 is defined as the angle formed by the symmetry-axis of the ER between a movement step. The movement of the symmetry axis being 2 dimensional, we have defined the rotational diffusion as $D_R/D_R^{\circ} = \frac{\langle \theta_1^2 \rangle}{t_{Phy}/t_o}$. In Fig. 4.3(b), we observe that rotational diffusion is

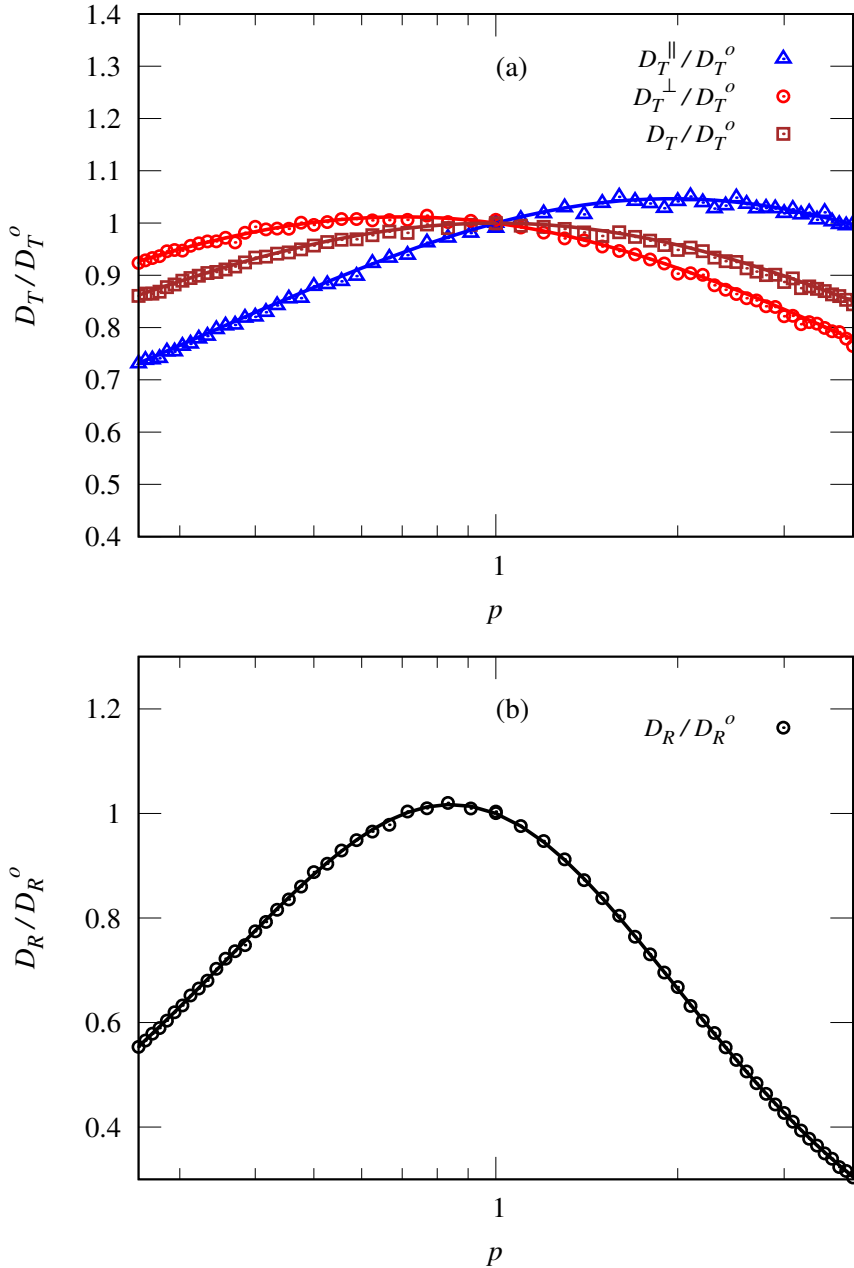


FIGURE 4.3: (a) D_T^{\parallel}/D_T^o (circles), D_T^{\perp}/D_T^o (triangle) and D_T/D_T^o (square) are shown for the different values of p at $\phi = 0.002$. Solid lines represent the analytical diffusion coefficient calculated for the single particle with a constant volume of $\pi/6$ for different values of p . (b) The change in D_R/D_R^o with respect to p is shown for the present work (circle), and analytical calculation from Perrin's factor is shown with solid lines.

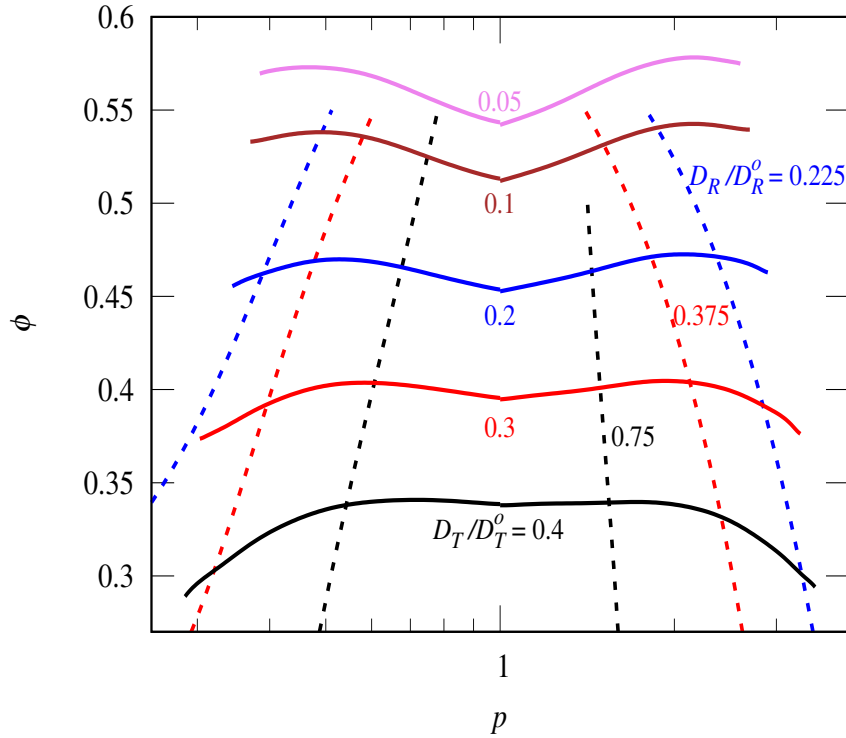


FIGURE 4.4: Iso-diffusivity lines are shown for different ϕ as a function of the aspect ratio p , where the solid lines and dotted line represent translational and rotational diffusion, respectively. The diffusion coefficients are as indicated in the figure.

asymmetric for prolate and oblate ER. The simulation results agree perfectly with the theoretical curve given by the equation. 3.15, 3.16 and 3.17 for infinitely dilute system.

In Fig. 4.4 we have plotted the iso-diffusivity lines for both the translational and rotational components of the ellipsoidal particles. We observed a similar trend as reported by Di Micheal et al. [20] for the diffusion coefficient. The swallow-like shape of the translational iso-diffusivity line, as reported by the event-driven Brownian dynamic method for the fluid of spheroids, is reproduced by the BCD technique as well.

The value of the diffusion coefficient will not match EDBD, as in BCD, we use Perrin's factor to mimic the dynamics, except at $p = 1$, where EDBD and BCD

agree perfectly, as already demonstrated by Babu et al. [97], and reproduced in the present work. The rotational diffusion iso-diffusivity lines show that D_R/D_R° reduces when the aspect ratio or ϕ increases, as reported by Tang et al. [162]. The rotational diffusion coefficient of BCD also follows the isotropic-nematic transition, as shown for the EDBD method [20].

4.3.2 Isotropic-nematic transition in spheroids

-spheres binary mixture

We have already shown that using the BCD method, the dynamics of one-component hard spheroids can be modeled. We now advance the study to binary systems, consisting of a combination of prolate-sphere and oblate-sphere systems. We define the number fraction of one of the components of the binary system as $f^p = n_p/N$ where n_p is the number of spheroids present in the system corresponding to a particular aspect ratio p . The volume fraction of the binary system having N particles, which includes both spheres and spheroids, is calculated as $N/L^3\pi/6$, since the volume of the individual particles is kept equal to a sphere of diameter unity.

We calculate the nematic order parameter S for the binary mixture. S is the largest eigenvalue of the tensor Q defined by

$$Q_{\alpha,\beta} = \frac{3}{2} \frac{1}{N} \sum_i \langle (n_\alpha)_i (n_\beta)_i \rangle - \frac{1}{2} \delta_{\alpha,\beta} \quad (4.1)$$

where $(n_\alpha)_i (n_\beta)_i \in (n_x)_i, (n_y)_i, (n_z)_i$ with $(n_\alpha)_i$ is the component of the orientation of the symmetry axis of ER. Here $S = 0$ means the purely isotropic phase, while $S > 0.3$ represents the nematic phase [20]. In Fig. 4.5 we have plotted the critical value of ϕ , where the transition from the isotropic to nematic phase is observed as a function of the fraction of the sphere in the binary mixture when $p = 4$ for the

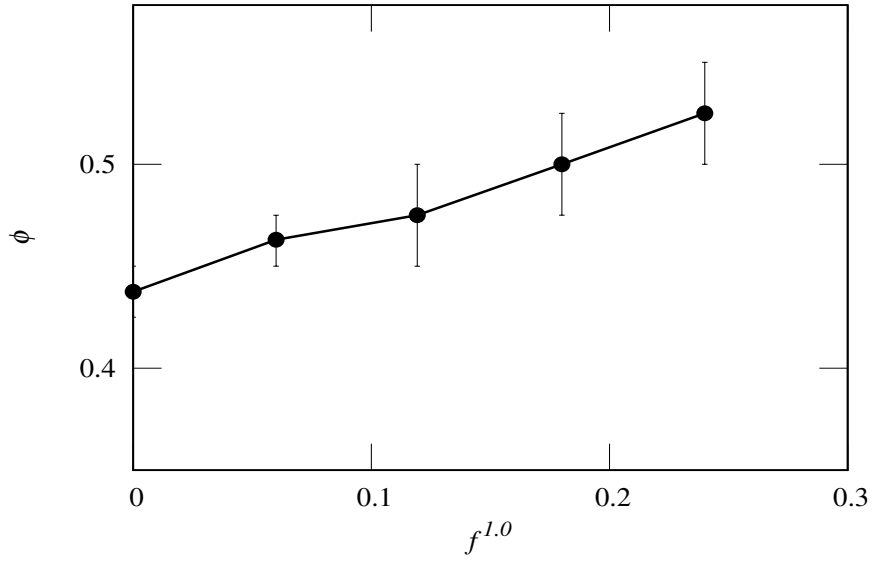


FIGURE 4.5: Variation in the isotropic-nematic coexistence density ϕ with respect to the fraction of sphere $f^{1.0}$, present in the binary mixture of sphere and prolate $p = 4$ system. The upper and lower tick on the error bar indicate the nematic and isotropic phases, respectively, confirmed by nematic-order-parameter calculation in the simulation.

prolate particles. For an ellipsoidal system of one component with $p = 4$, we observe that the isotropic nematic transition occurs at $\phi \sim 0.43$. The isotropic, nematic transition is shown to be weakly first order in nature [163]. As shown by Eppenga et al., the minimum number of particles in the nematic phase should be above 400 to match with the theoretical calculation [164], which we have made sure in the present work. They have shown that the system is in the nematic phase when $S > 0.3$. We have simulated 20 independent configurations for each ϕ and f^p in the present work. When all the configurations give $S > 0.4$ we identify the system to be in the nematic phase. Similarly, when all the 20 configurations have $S < 0.2$, we identify the system to be in the isotropic phase. The upper and lower ticks on the error bar of the phase diagram in Fig. 4.5 correspond to these two volume fractions, and the point is an average of the volume fractions for a particular $f^{1.0}$. For example at $f^{1.0} = 0.12$, we found that $S > 0.4$ for $\phi \geq 0.5$ and $S < 0.2$ for $\phi \leq 0.45$. The phase diagram shows

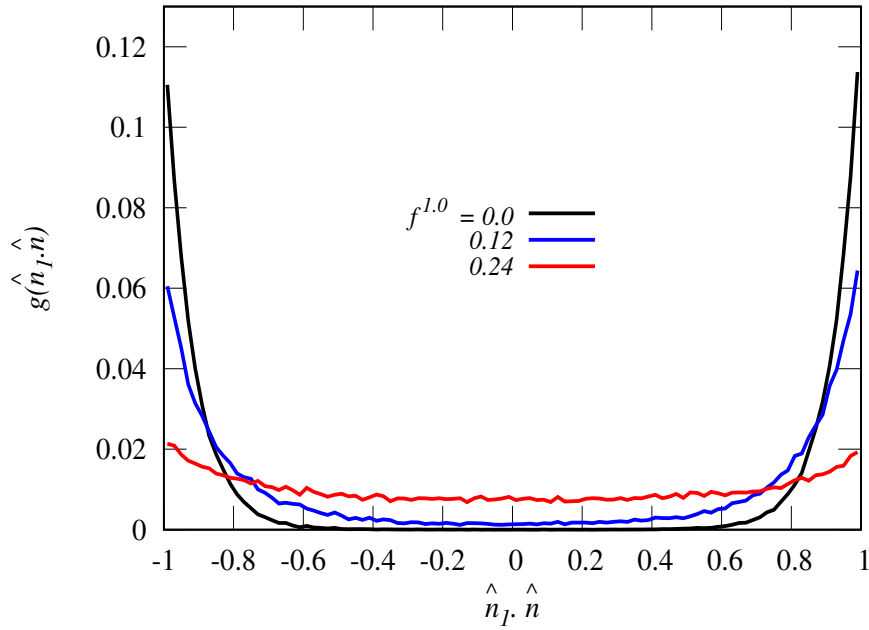


FIGURE 4.6: $g(\hat{n}_I \cdot \hat{n})$ is shown as a function of $\hat{n}_I \cdot \hat{n}$ which is the cosine of the angle made by the director with the symmetry axis of the prolate ellipsoids $p = 4$ at different fractions of spheres as mentioned in the figure.

this point at $\phi = 0.475$ with an error bar of ± 0.025 . As we increase the volume fraction of the spheres, we observe that the isotropic, nematic transition is stable at higher fractions of the sphere. It has already been shown analytically that the glass transition for one component spheres and ellipsoids with $p = 4$ is around $\phi \sim 0.57$ [144]. So, we have restricted this study upto a volume fraction of 0.55 as the main focus is on the diffusional properties of both spheres and ellipsoids.

In order to show the effect of spheres over the alignment of spheroids observed for one component prolate system, we have calculated the angular distribution $g(\hat{n}_I \cdot \hat{n})$, with respect to the nematic-director \hat{n}_I . Where \hat{n} is the unit vector along the symmetry axes of the ellipsoids at equilibrium. In Fig. 4.6, we have plotted $g(\hat{n}_I \cdot \hat{n})$ of the ellipsoids in the binary mixture of prolate $p = 4.0$ and the sphere system at $\phi = 0.5$, for different fraction of spheres. In the nematic phase, the symmetry axis of the ellipsoids is either parallel or anti-parallel to the director. The two peaks

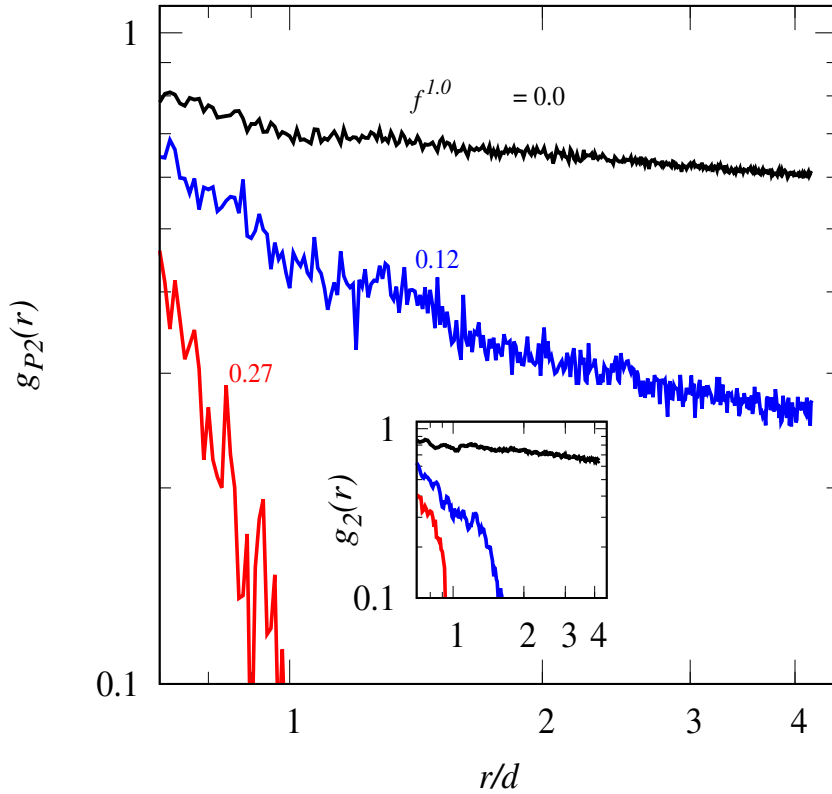


FIGURE 4.7: $g_{P_2}(r)$ is shown as a function of the distance r/d for binary system of spheres and prolate $p = 4.0$, at $\phi = 0.50$, with fraction of sphere as indicated in the figure. The inset shows the $g_2(r)$ calculation for the same configuration as indicated in the figure.

observed for $f^{1.0} = 0.0$ at $\hat{n}_I \cdot \hat{n} = 1$ and -1 , indicating the presence of a high degree of alignment in the one-component system of spheroids as also confirmed by the calculation of the orientational order parameter. When the sphere fraction is 0.12 we observe that the fraction of aligned particles steadily decreases, although we have a nematic phase as confirmed by the S parameter calculation see Fig. 4.5. When the fraction of spheres is further increased, we observe a uniform distribution, which signifies the isotropic distribution of spheroids.

In order to understand the local ordering of the ellipsoidal system, we have calculated $g_{P_2}(r)$ and $g_2(r)$ defined as

$$g_{P_2}(r) = \left\langle \frac{1}{2}(3 \cos^2 \theta_r - 1) \right\rangle \quad (4.2)$$

$$g_2(r) = \langle \cos(2\theta_r) \rangle \quad (4.3)$$

Where θ_r is the angle between the symmetry axes of two ERs at a distance of r from the center of mass of the ER particle, see Fig. 4.7. For the nematic phase, we know that $g_{P_2}(r)$, will not decay to zero as can be observed for the case of one component $f^{1.0} = 0$ and $f^{1.0} = 0.12$. The orientational order for the one-component system can be clearly seen in a typical snapshot of the system at equilibrium in Fig. 4.8. The bounding box shown in the Fig. 4.8(a) shows the area over which we are able to observe the nematic phase consistent with the $g_{P_2}(r)$ calculation of one component ellipsoidal system as shown in Fig. 4.7. In the binary system, when $f^{1.0} = 0.12$ we observe that $g_{P_2}(r)$ relaxes to a constant value, consistent with the phase calculation. While $g_2(r)$ relaxes faster as it only explores the local order between ellipsoidal particles. In $g_2(r)$ calculation at $f^{1.0} = 0.12$ we observe local order up to a distance of $< 2d$, as shown in the inset of Fig. 4.7, also see Fig. 4.8(b). When the fraction is further increased to $f^{1.0} = 0.27$, the ordering decays much faster and is confined to the distance smaller than the value $0.9d$ for both $g_{P_2}(r)$ and $g_2(r)$ calculation. This can be observed in the bounding box in Fig. 4.8(c), where the nematic order around the spheres is destroyed. Thus, we have confirmed that in a binary mixture of sphere-prolate systems, only local order is observed depending on the fraction of spherical particles present in a particular volume fraction.

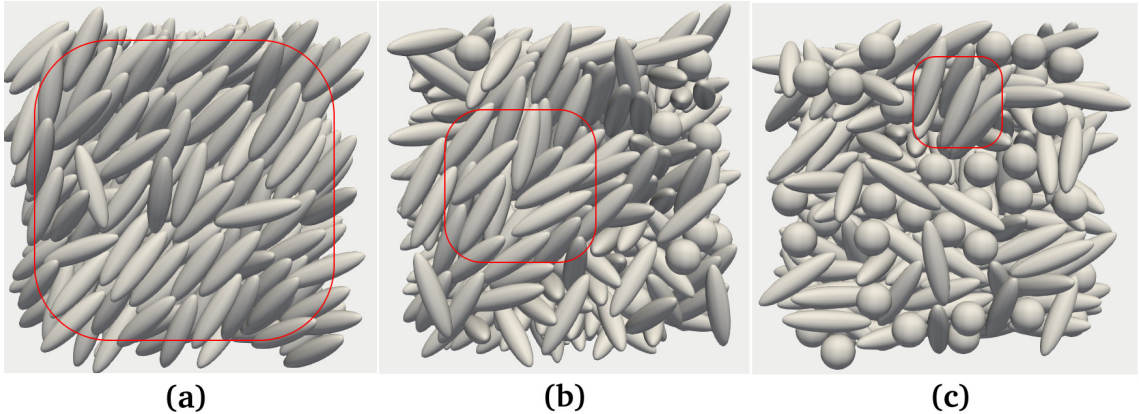


FIGURE 4.8: Snapshot of the binary spheroidal-sphere system with increasing fraction of spherical particle from left to right for $\phi = 0.5$, $p = 4.0$ and at (a) $f^{1.0} = 0.0$, (b) $f^{1.0} = 0.12$, (c) $f^{1.0} = 0.27$. The ordered reason (the bounding box) can be seen decreasing with increasing the number of spheres in the system.

4.3.3 Dynamics in a two-component system of spheroid-sphere

Fig. 4.9 shows D_T/D_T^0 which is the diffusion coefficient of only one species of particle, spheres, or spheroids, in the binary system as a function of ϕ . In the binary mixture, we have studied two combinations, one with spheres and the ER with $p = 4$ see Fig. 4.9(a). The other one with spheres and ERs $p = 0.25$ see Fig. 4.9(b). For the spherical one-component system $f^{1.0} = 1$, we observe that the diffusion coefficient of the sphere goes down monotonically [97]. For the oblate and prolate system of one component ($f^{1.0} = 0$) the diffusion coefficient for a low volume fraction is always smaller than the spherical system, which can also be observed in Fig. 4.3 for an infinitely dilute system. The diffusion coefficient of the spheroidal system goes down as we increase the volume fraction to $\phi < 0.35$, similar to the case of a hard sphere system. For $\phi > 0.35$ we observe that the slope of the diffusion curve of a one-component ellipsoidal particle increases and crosses the one-component spherical system. For the ellipsoidal system of one component, a nematic transition is expected for aspect ratio 4 [165, 166, 167], which is reproduced by the BCD

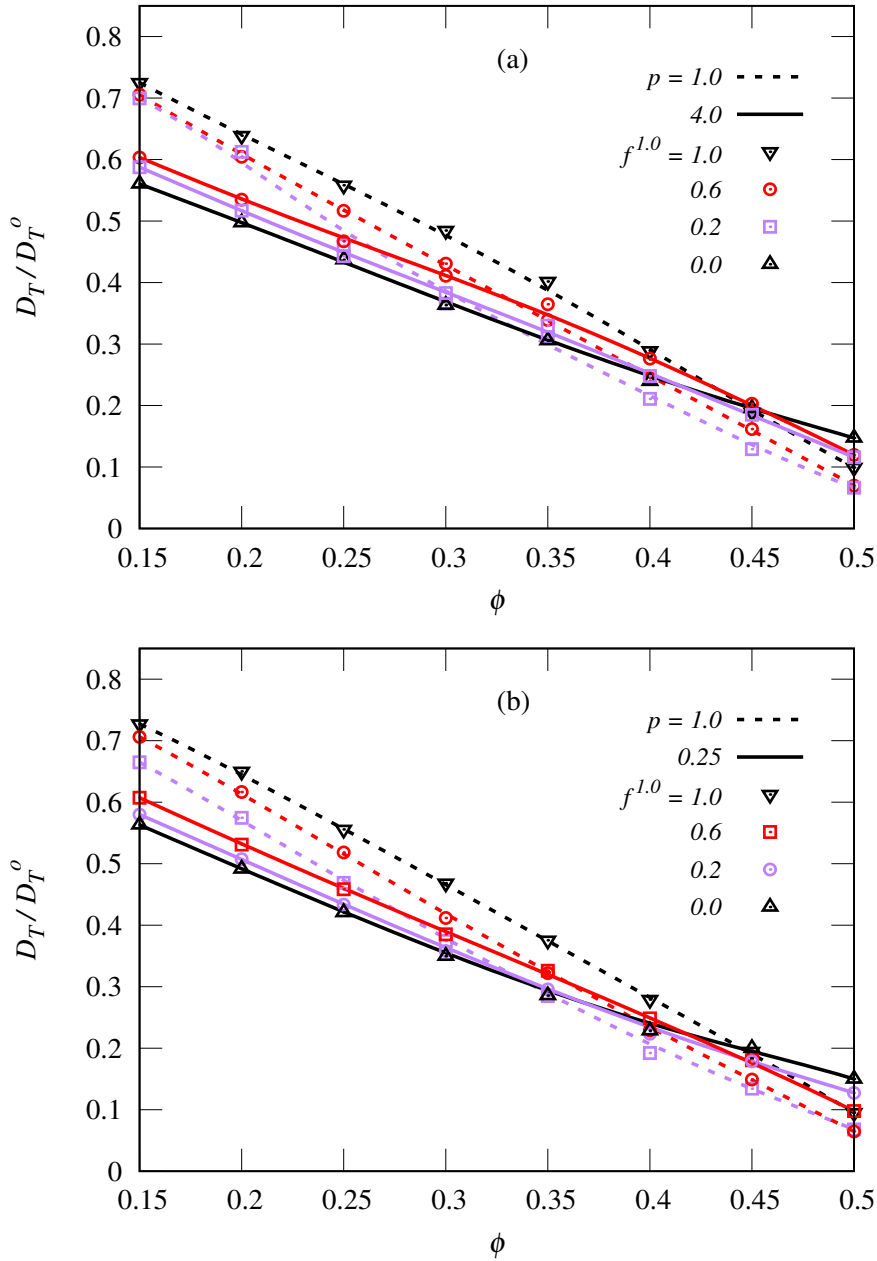


FIGURE 4.9: (a) D_T/D_T^0 shown for the binary system containing particles with sphere $p = 1.0$, prolate $p = 4.0$. The solid symbols represent the diffusion coefficient of only the prolate particles in the binary mixture. The short dashed line represents the diffusion coefficients of only the spherical particles. The fraction of spherical particles is indicated in the figure. (b) D_T/D_T^0 is plotted for an oblate $p = 0.25$ and sphere mixture. Where lines show the diffusion coefficient for $p = 0.25$ (solid) and for spheres (short dash), simulated with the fraction of sphere as indicated in the figure.

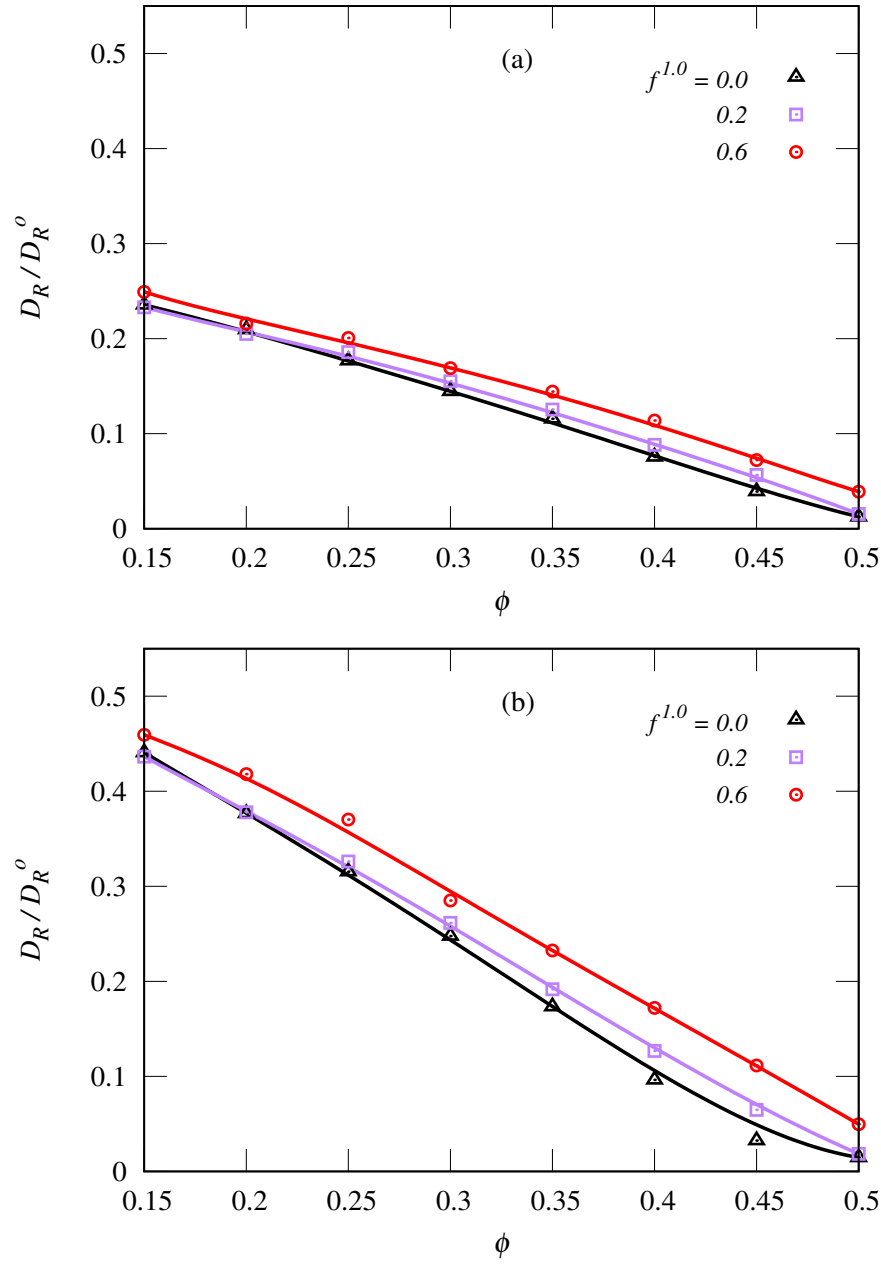


FIGURE 4.10: (a) D_R/D_R^0 is shown for the binary system containing both sphere and prolate $p = 4$ particles at different ϕ . The fractions of the sphere are given in the figure. (b) $D_R^{0.25}/D_R^0$ is shown for the binary system containing both sphere and oblate $p = 0.25$ particles at different ϕ . The fractions of the sphere are given in the figure.

technique. We observe that for $\phi > 0.43$ the translational diffusion coefficient of the one-component ellipsoidal system becomes higher than the spherical system. This effect has already been shown in the case of short-term diffusion coefficient for monomeric rods simulated with hydrodynamic interaction [132, 141]

For the binary mixture with $f^{1.0} = 0.2$, we observe that D_T/D_T° of only the spheres in the mixture decreases compared to the case of one component $f^{1.0} = 1$, due to the presence of ER. For very low ϕ we observe that diffusion is controlled by the friction coefficient, and hence the sphere diffuses faster than ellipsoids. An interesting phenomenon we observe is that the diffusion coefficient of the ellipsoids increases in the presence of spherical particles for higher volume fraction compared to the one-component system of spheres having the same volume fraction. With increasing volume fraction of the binary system, the volume available to the center of mass of both spheres and ellipsoidal particles to diffuse decreases. As the number of spheres increases, the channels of free space available for the ellipsoidal particle to diffuse become narrower. When the average channel width of the free space becomes comparable to the diameter of the sphere, we observe that the diffusion coefficient of the spheres decreases dramatically in the binary system. For the ellipsoidal particles, as the semi-minor axis is smaller than the radius of the sphere, it can squeeze through the channel, which is forbidden for the spheres due to the excluded volume of the binary mixture. As we increase the fraction of spherical particles to $f^{1.0} = 0.6$, we observe that the diffusion coefficient of the spherical particle in the binary mixture is lower compared to the diffusion coefficient at $f^{1.0} = 0.2$. When the fraction of spheres increases for the same volume fraction, the accessible volume becomes smaller for the isotropic spheres compared to that of the anisotropic particle. For the anisotropic particle, there is a competition between the friction coefficient, which reduces the diffusion coefficient compared to the sphere, and exploration of the more

accessible volume due to the anisotropy of the ellipsoidal particles. For the fraction $f^{1.0} = 0.2$ the friction coefficient effect wins $\phi < 0.3$, as the accessible volume available for the binary mixture is large, and thus the sphere diffuses faster. For $\phi > 0.3$ the ellipsoidal particle can squeeze through the free space channels created as the length of the minor axis is smaller than the radius of the sphere. For the case of oblate particles, we also observe a similar trend as for the case of prolate ellipsoidal particles. For the prolate case, the crossover for $f^{1.0} = 0.2$ happens at a lower volume fraction $\phi \sim 0.3$ compared to the case of $f^{1.0} = 0.6$ where it happens at $\phi \sim 0.35$. In the oblate case, the crossover with the diffusion coefficient of the spherical particle occurs at a slightly higher volume fraction. For $\phi > 0.45$, in the binary mixture, the ellipsoidal particles see a decrease in D_T/D_T^o in the presence of spheres, compared to the one-component ellipsoid case. The trend is the opposite, as observed in the low ϕ regime, where diffusion is enhanced in the presence of spheres. At a higher volume fraction, the accessible volume available to the mixture will be smaller, as the average width of the free space channel will become comparable to the semi-minor axis, and thus, the ellipsoidal particles will slow down. In the case of one component, ellipsoidal particles, it undergoes a nematic transition.

The isotropic nematic transition effect is clearly observed in the case of the rotational diffusion coefficient for the mixture with aspect ratios 4 and 1. In Fig. 4.10 we have plotted the D_R/D_R^o as a function of volume fraction for $f^{1.0} = 0$, $f^{1.0} = 0.2$ and $f^{1.0} = 0.6$ for prolate see Fig. 4.10(a) and oblate see Fig. 4.10(b) binary system. The $f^{1.0} = 0$ ellipsoidal system has a minimum rotational diffusion, which is expected as we observe the isotropic nematic transition for $\phi > 0.43$. For the case of $f^{1.0} = 0.2$, the rotational diffusion coefficient increases slightly compared to the case of one component. We also observe that the diffusion coefficient for $f^{1.0} = 0.2$ tends towards the one component case for $\phi \geq 0.5$, as expected for higher volume fraction as the

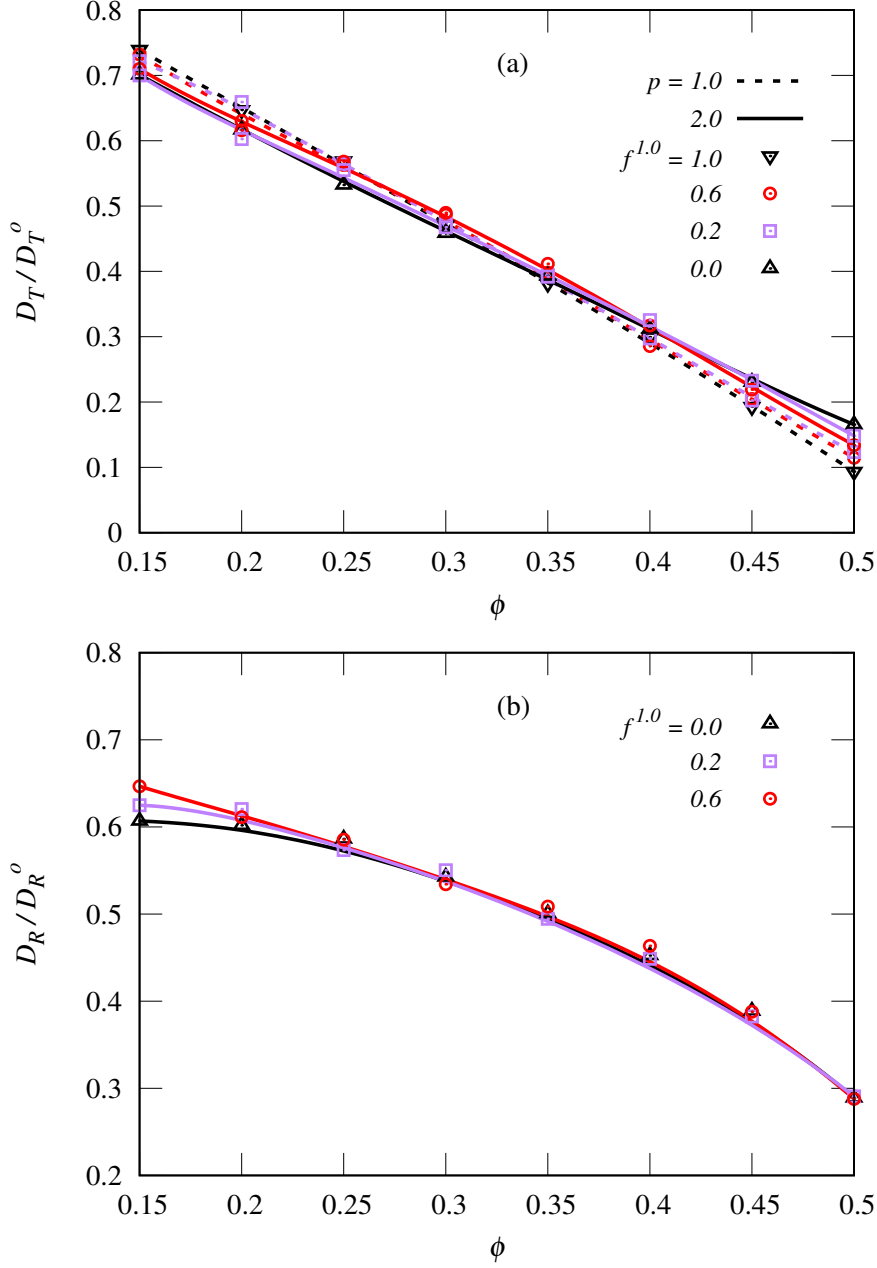


FIGURE 4.11: (a) D_T^e/D_T^o are shown for the spheres (dashed line) and prolate particle (solid line) with aspect ratio 2.0 at different ϕ in the binary mixture. The fraction of the sphere in the system is shown in the figure. (b) D_R^e/D_R^o is shown for the ellipsoidal particles $p = 2$ in the binary mixture with the fraction of sphere as indicated in the figure.

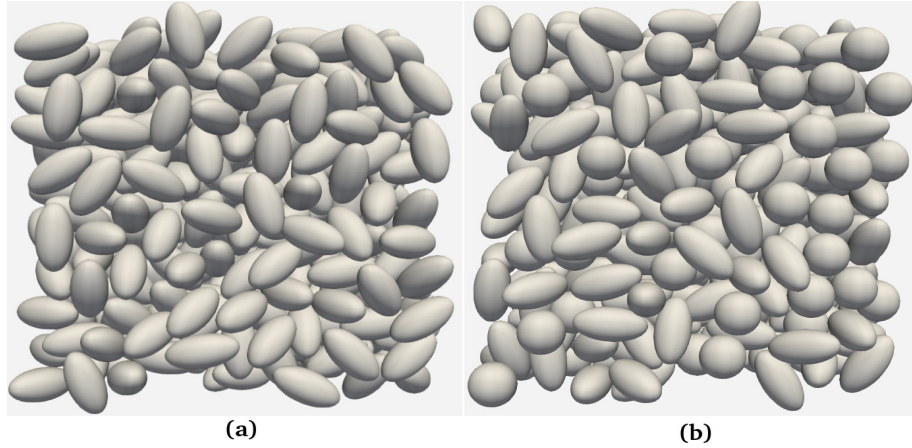


FIGURE 4.12: (a) Snap shot of the monomeric prolate particle with $p = 2$ at $\phi = 0.5$ as obtained from the simulation. (b) The snapshot of a binary mixture of spheres and prolates $p = 2$ with the fraction of sphere $f^{1.0} = 0.40$. In both systems, we do not observe nematic transition.

volume available for the ellipsoidal particle decreases. When the fraction $f^{1.0} = 0.6$, for the prolate and oblate ER in the binary mixture, we observe that the rotational diffusion coefficient is higher than for the system of one component. The reason could be that structurally, there is a change in the system compared to the $f^{1.0} = 0$ case, and it may be the absence of isotropic nematic transition. Note that the glass transition for the one-component ellipsoidal and spherical particles is reported at a volume fraction greater than 0.5 [144, 135].

To verify whether the nematic order is the only reason for the observed enhancement in the diffusion coefficient for the monomeric ER, we performed the simulation of a mixture of spheres and prolate particles at $p = 2$. Note that for $p = 2$ the isotropic-nematic transition is absent [165, 166], which can also be observed in the snapshot shown in Fig. 4.12 (a) for $\phi = 0.5$ and $f^{1.0} = 0$. We have plotted the transnational diffusion coefficient of only the prolate and sphere system in the mixture as a function of the total volume fraction ϕ in Fig. 4.11(a). The translational diffusion coefficient of $p = 2$ of the ellipsoids of one component crosses the corresponding sphere diffusion coefficient for $\phi > 0.35$. We have also confirmed that the nematic order is not

observed in this case. This implies that the enhancement in diffusion coefficient happens due to the anisotropic shape of the particles, and the nematic phase just assists in the enhancement of the diffusion coefficient for the higher volume fractions.

In Fig. 4.11(b), we have plotted the rotational diffusion coefficient for the mixture at $f^{1.0} = 0.2$. Here, we observe that due to the presence of spheres, for low ϕ the rotational diffusion coefficient is higher than the one-component prolate system. As the fraction of spheres increases, the prolate particle will have more free space for rotation, compared to the one component prolate particle, at the same ϕ . When $\phi > 0.25$, we can observe that the rotational diffusion of all fractions agrees with the $f^{1.0} = 0$ case, as the crowding effect of the spheres increases, indicating that the free space to perform rotational diffusion is equivalent to the one component prolate case.

4.4 Discussion and Conclusion

Recently, Roger et al. [135], showed the existence of liquid glass for monomeric ellipsoidal particles. To prevent the system from undergoing an isotropic nematic transition, the walls of the enclosed simulation box were made rough. They observed that the rotational diffusion tends towards zero without the nematic order. In the present work, the ellipsoid-sphere binary system with $f^{1.0} = 0.2$, we observe that the rotational diffusion coefficient tends towards the one component case for $p = 4$ at $\phi = 0.5$. Note that in the one-component case, the nematic transition happens for $\phi > 0.43$, while in the binary system, we have shown that the nematic transition is absent, and the rotational diffusion tends towards zero. Thus, by adding polydispersity in the form of a sphere, we might observe the liquid glass phase proposed by Roger et al. for the dynamics of the ellipsoidal particle in the binary mixture.

When we further increase the fraction of sphere $f^{1.0} = 0.6$, the rotational diffusion is higher than the one component case exhibiting only liquid-like behavior for the ellipsoidal particle.

As we increase the fraction of sphere in the binary mixture, we observe that the nematic phase vanishes for the particular ϕ . Similar kinds of phase behavior have also been observed in sphere-rod mixture [168] as well as for the prolate-sphere mixture [169]. Using the density functional theory, the same effect was observed [170]. They also did not observe any demixing of the sphere and ellipsoidal systems similar to those observed in the present work.

In the present work, we successfully extended the Brownian cluster dynamics method to study ellipsoids, which include both prolate and oblate ellipsoidal particles. The ellipsoidal particle considered has a constant volume $\pi/6$, which is equivalent to a sphere of unit diameter. To identify the overlap between different ellipsoids, we employed the bounding box method where we enclose the ellipsoidal in a rectangular box if and only if the boxes overlap, we employ the ellipsoidal contact function to verify the ellipsoids overlap. If overlap is detected, we reject that particular movement step. The translational dynamics of ellipsoids are implemented by moving the center of mass of the ellipsoids in a random direction. The diffusion along the direction parallel to the symmetry axis and perpendicular to the symmetry axes are chosen according to Perrin's factor, which was solved for the stick boundary condition [103]. In order to mimic the rotational dynamics, we employ the quaternion method to rotate the orientation vector along the long axis of the ER by using Perrin's factor for the rotation. In the present work, one unit of time is defined as the time a sphere of unit diameter and volume $\pi/6$ takes to travel its own diameter.

One of the drawbacks of the method is that the step size we choose should be smaller than the inter-particle distance to define the diffusion properly. For a larger step

size, we induce a lot of collision with the neighboring particle, thereby reducing the diffusion coefficient of the system. For a smaller step size, the physical time over which we can explore the system reduces. We have shown that the diffusion coefficient of the dilute system agrees with the analytical equation given by Perrin et al. [103], confirming our definition of time is correct. The iso-diffusivity line for the ellipsoidal particle as a function of volume fraction was predicted to have a swallow-like shape by event-driven molecular dynamics, which also agrees with our method. However, the absolute values of the diffusion coefficient do not match because of the way the diffusion is defined in both cases, except for the sphere, where both methods yield the same result. We have also extended the BCD method to incorporate the binary ellipsoid and sphere systems. Here, we observe that even though the diffusion of a single sphere is faster than that of ellipsoids, the diffusion coefficient of ellipsoids is higher than that of the corresponding sphere at $p = 4$ and $p = 2$ for a larger volume fraction. It was also shown that the reason for the increase in the diffusion coefficient is particle asymmetry, and the isotropic-nematic transition only enhances the absolute value of the diffusion coefficient. In the binary mixture, we have shown that as the fraction of spheres increases, nematic ordering starts breaking in the region close to the sphere. It leads to a gradual decrease in the order parameter and, finally, to the isotropic phase, as shown in the phase diagram. We also calculated the diagram of the isotropic nematic phase, where we observed that as the fraction of spheres increases, ϕ also has to be increased to maintain the nematic phase. It will be interesting to study the nematic phases of a mixture of ellipsoids, where both particles undergo nematic transition for a range of fractions.

Part II

**Kinetics of growth and structural
properties of spheroidal-colloids
interacting through
anisotropic-attractive-potential**

Chapter 5

Kinetics and phases shown by reversible-aggregation of patchy spheroids

5.1 Kinetics in the reversible aggregation of spheroids

According to Noro-Frenkel's law of corresponding states, the structural and other thermodynamic properties are similar if compared among different spherically symmetric short-range pair potentials having the same reduced density and second virial coefficient. Where the second virial coefficient is defined as,

$$B_2 = \int f(\mathbf{r}_{i,j}) d\mathbf{r}_{1,2} \quad (5.1)$$

with f being Mayer-f function given as $f = 1 - \exp[-\beta V(\mathbf{r}_{1,2})]$. Foffi and Sciortino [171] found the law valid close to the liquid-gas critical point for a system of patchy

particles having short-range directional bonding. In this way, the law found the extension possible for a system of anisotropic attractive potential.

In colloids, particles interact through the short-range potential, where the Noro-Frenkel law can be seen as widely applicable. In this work, we seek further application of the law for the pair potential with anisotropy in terms of interaction and its hardcore.

5.2 Exploring validity of Noro-Frenkel generalized law of corresponding states for anisotropic pair-potential with spheroidal hard-core

We define a pair potential for the spherical particles with the property of directional bonding. For the particles i and j with director $\hat{\mathbf{n}}_i$, $\hat{\mathbf{n}}_j$ and inter-particle distance \mathbf{r}_{ij} the potential is defined as,

$$U_{i,j} = \begin{cases} -u_\circ \cdot \sigma_{i,j}(\mathbf{r}_{i,j}, \hat{\mathbf{n}}_i, \hat{\mathbf{n}}_j) \cdot \chi_{i,j}(\hat{\mathbf{r}}_{i,j}, \hat{\mathbf{n}}_i, \hat{\mathbf{n}}_j) & \\ \infty & \text{Hardcore} \quad \text{overlap} \end{cases} \quad (5.2)$$

Where u is the depth of the square well potential with the interaction range $\epsilon = 0.1$. We define $h_{i,j}(\mathbf{r}_{i,j}, \hat{\mathbf{n}}_i, \hat{\mathbf{n}}_j)$ as the distance between the surfaces of the hard cores, calculated by using ellipsoids contact function (ECF)[172]. $\sigma_{i,j}$ and $\chi_{i,j}$ is defined as,

$$\sigma_{i,j} = \begin{cases} 1 & h_{i,j} < \epsilon \\ 0 & \text{Otherwise} \end{cases} \quad (5.3)$$

$$\chi_{i,j} = \begin{cases} 1 & |\hat{\mathbf{r}}_{ij} \cdot \hat{\mathbf{n}}_i| \geq \cos(\omega), |\hat{\mathbf{r}}_{ji} \cdot \hat{\mathbf{n}}_j| \geq \cos(\omega) \\ 0 & \text{Otherwise} \end{cases} \quad (5.4)$$

Where $\chi_{(i,j)}$ represents patches attached on both sides, along the symmetry axis of spheroidal hard-core. Therefore, we can control the number of bonds per patch by tuning ω .

For the potential defined above, the second Virial coefficient B_2 can be written as,

$$B_2 = \int \frac{1}{4\pi} \int \frac{1}{4\pi} \int (1 - e^{-V(\mathbf{r}_{12}, \hat{\mathbf{n}}_1, \hat{\mathbf{n}}_2)}) d\mathbf{r}_{12} d\hat{\mathbf{n}}_1 d\hat{\mathbf{n}}_2 \quad (5.5)$$

where \hat{n} is the orientation of the particles.

B_2 is a quantity that depends upon the volume of the integral and the temperature. Therefore, it does not contain any information regarding the geometric properties of the potential. Fig. 5.1 shows B_2 for different shapes and patches calculated for prolate-spheroids having the same volume $v = \frac{4}{3}\pi ab^2$. Variation in B_2 with varying patch angle ω (fig.5.1(a)) for the different p , at a constant temperature $k_B T/u_\circ = 0.114$. Fig. 5.1(b) shows variation in B_2 with P calculated for different $k_B T/u_\circ$. For the same patch angle, particles with high anisotropy ($p > 1$) show lower B_2 (higher attractive part of B_2). As for the same patch angle, we have a greater volume of solid angle for the high value of \mathbf{r}_{12} , which corresponds to the more elongated particles.

As seen in Fig 5.1, the B_2 for higher p goes down faster compared to the more isotropic particles. But even if we reduce the solid angle to make the B_2 comparable to the other shape, the geometry of the hardcore will still be there to decide the number of bonds formed per patch. For example, in the case of two patch colloids of spherical particles, with $\omega = 25^\circ$ we will get only chains in all the cases [157].

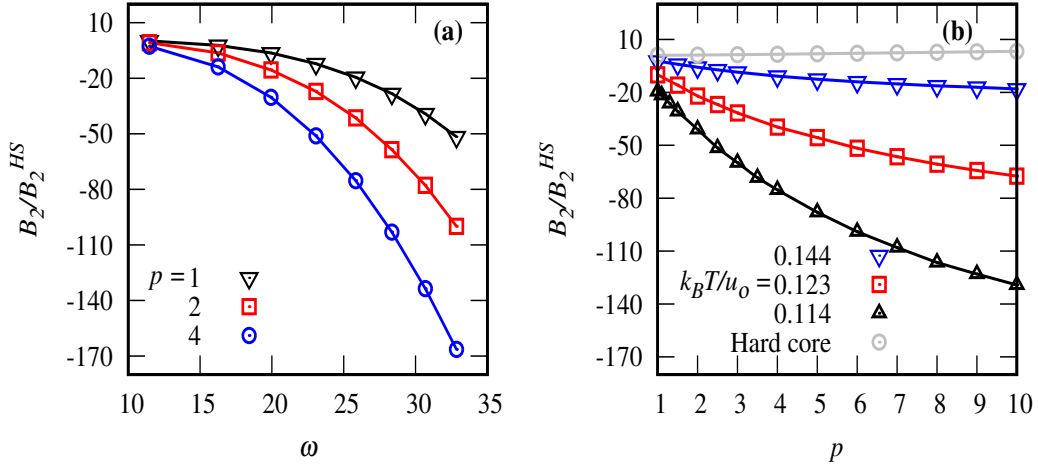


FIGURE 5.1: (a) B_2/B_2^{HS} is shown for different patch angle ω , for a system of prolate spheroidal particles decorated with two patches along the axis of symmetry and aspect ratio $p = 1$ (triangle), 2 (square) and 4 (circle) calculated at $k_B T/u_o = 0.114$. (b) B_2/B_2^{HS} is shown for the different shapes of the prolate particles defined by the aspect ratio p of the particle's semi-minor and the major axis length, calculated at different $k_B T/u_o = 0.114$ (lower triangle), 0.123 (square), and 0.144 (circle). Where the patches have constant $\omega = 25^\circ$. Grey circle points show the B_2/B_2^{HS} of the repulsive hardcore part of the particle at different p .

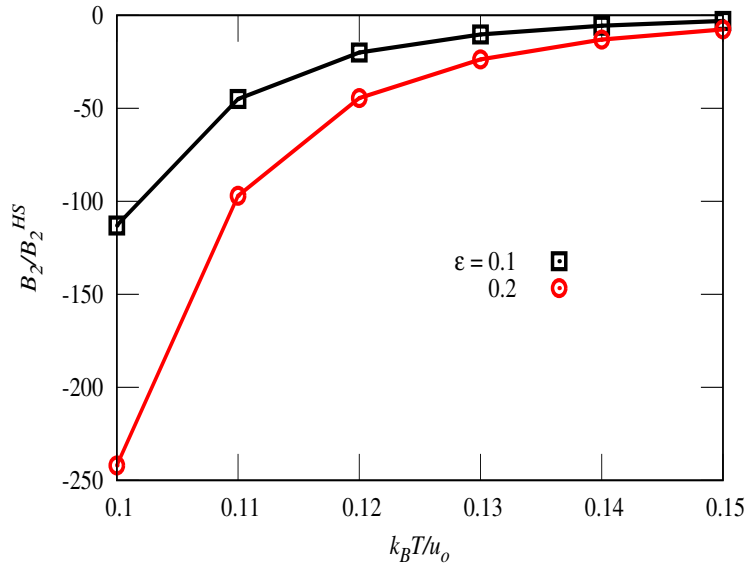


FIGURE 5.2: B_2/B_2^{HS} is shown for different $k_B T/u_o$, calculated at $p = 1.5$, $\omega = 25^\circ$ and two different patch ranges $\epsilon = 0.1$ (square) and 0.2 (circle). Here, the shape of the particles has been kept similar.

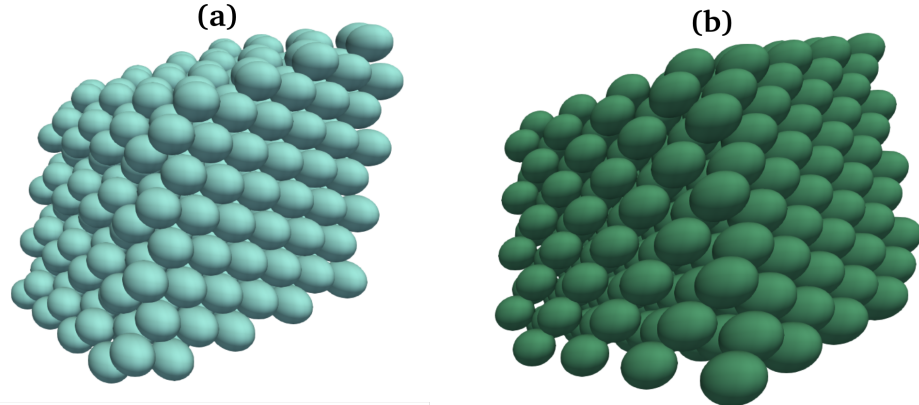


FIGURE 5.3: **HCP** arrangement of spheroids with $p = 1.5$, shown for the two different patch ranges (where patches are attached at the two ends of the particle along the symmetry axis of the particle) (a) $\epsilon = 0.1$, at $k_B T / u_0 = 0.1075$ and (cyan spheroids) (b) $\epsilon = 0.2$, at $k_B T / u_0 = 0.117$ (green spheroids), as predicted by variable shape simulation methods.

However, for the same B_2 in the case of prolate spheroids with $p = 1.5$ (which can be gained by confining the angle and making it $\omega = 22^\circ$), we observe the formation of monolayers (as it has been shown in the later chapters). As B_2 does not depend on the geometry of the potential distribution but only the volume, it also does not care about the number of bonds limited by the same. Therefore, in the case of shape anisotropic particles, the law may find its extension if the particles being compared are similar in geometry. In this way, the law may appear to play the same role in the scaling of equilibrium properties for the different sizes as the diffusivity plays in the dynamics of the Brownian particles, as it has been shown that the diffusion of large Brownian particles suspended in fluid shows the same shallow like iso-diffusivity lines as it has been shown for the fluid particles calculated using Molecular dynamics simulation (4.4).

To compare the two systems with similar geometric shapes, we took two different patch ranges with the same patch angle $\omega = 25^\circ$ and $p = 1.5$. We calculated B_2 at different $k_B T / u_0$ (Fig 5.2) for the two different patch ranges $\epsilon = 0.1$ and 0.2 . We

drew a horizontal line and marked two different temperatures $k_B T/u_0 = 0.1075$ and 0.117 having the same $B_2 = -58.0$ (see Fig 5.2). We simulated the two systems and found the variable shape simulation methods confirming the same minimum energy configuration with three bonded neighbors per patch. We have shown both the structures in Fig 5.3. In the next chapter, we have explored the phase diagram with patch range $\epsilon = 0.1$. By looking at the result predicted by the variable shape simulation method, we can find the possibility of extending the validity of the law even for the shape anisotropic systems with different sizes.

Chapter 6

**Self-assembly of patchy anisotropic
particle forming free-standing
monolayer film**

Abstract

Synthesizing thin films using self-assembly is one of the critical challenges that need to be addressed for making engineered material using colloidal particles, which is necessary for creating novel material for photonics, filtration applications, etc. Here, we present a simple model of the prolate ellipsoidal particle with 2 directional bonds and study the phase behavior using NVT and NpT Monte Carlo simulation. We have observed that for anisotropic particles with patches, two different types of 3 dimensional ordered structures are formed, as well as thermodynamically stable monolayer confirmed using thermodynamic integration. The phase diagram shows us that we can create the desired $2D$ superstructure using a simple self-assembly route.

6.1 Introduction

There has been significant development in the field of template-based engineered materials in colloids [173, 174, 175]. The desired superstructures of colloids can be formed by using anisotropic particles [176], manipulating the interaction between colloidal particles functionalized with DNA [177] or introducing directional bonds between colloidal particles [178, 179]. Various applications have been proposed for the colloidal thin film-like materials with unique photonic [175] or plasmonic sensing [180] properties. For the formation of thin films, a substrate [176, 181] is required, and the drawback of the method is the rupture of mechanically sensitive thin film from the wafer. The free-standing film [182, 183] formed by the self-assembling process can overcome this drawback as it does not require the support of the substrate to grow, although scaling up the structures is very challenging.

To engineer materials with specific properties through self-assembly, the patchy colloidal particles are considered as ideal building blocks [184, 185]. Patchy particles usually have a hardcore component with decorated patches on the surface [184, 186]. The hardcore component can have a symmetric shape like the sphere [184] or asymmetric shape like ellipsoids, rods [187], 2 dimensional structure, etc. Most of the studies have concentrated on spherical patchy particles. They exhibit rich phase properties which include crystals, bundles, chains, etc. [179, 178, 188, 95, 189, 190, 191, 192, 193]. Only a few studies have concentrated on anisotropic hard-core, e.g., spheroids [194, 6, 195].

In the present work, we have performed Monte-Carlo simulation in both NpT as well as NVT ensembles. For the NVT simulation, we have used Brownian Cluster dynamics (BCD) [149, 150, 97, 196, 172]. BCD was originally developed to study both reversible [66, 129] and irreversible [154, 151, 152, 155, 156] aggregation of

spherical particles with square well interaction. The bundle formation of a lysozyme protein was mimicked after incorporation of patchy interaction with the isotropic potential [196, 100, 157, 158] for spherical particles using BCD. Later, the BCD was extended to simulate the structure and dynamics for both prolate and oblate particles [172]. In the present study, we have focused on prolate particles with two patches placed at the opposite ends of the major axis. Here, we control the valency by controlling the patch angle as we have kept the patch width constant. Thermodynamic calculation showed that through the self-assembly of ellipsoidal patchy, the crystals and fluids are the stable structure along with the free-standing ordered monolayer structure.

The paper is arranged the following way: in Sec. 6.2, we have explained the Kern-Frenkel potential applied to anisotropic particles. We have also explained the Brownian cluster dynamic method used to simulate the NVT ensemble, followed by NpT ensemble calculation using the Monte Carlo method. In the Sec. 6.3, we have shown that the ellipsoidal particles with patches at finite temperature and pressure undergo a gas crystal phase transition. The crystals formed have an HCP structure. We have identified two types of HCP crystal structures based on the number of bonds by the system. Surprisingly, we were also able to identify a small range of temperature and pressure, where a free-standing monolayer of thin film was the thermodynamically stable structure. These results were verified using both floppy box simulation as well as free energy calculation. We have also performed thermodynamic integration and have plotted the phase diagram for the system. We have proposed that the self-assembly can be used to produce free-standing film, which is followed by a conclusion in sec. 6.4

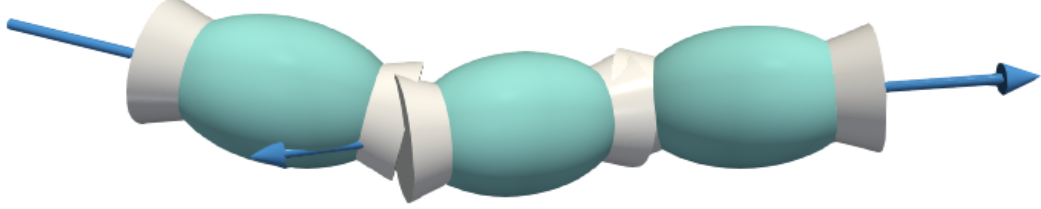


FIGURE 6.1: Three bonded ellipsoidal particles are shown. The arrows represent the orientation vectors (\hat{n}), and the white conic section represents the patches.

6.2 Simulation method

We have used discontinuous potential as an approximation of molecular potential. The shape of the prolate hard core potential is defined by the aspect ratio $p = a/b$, where a and b are the lengths of the semi-major and semi-minor axis, respectively. In the present study, we have kept $p = 1.5$ so that we can avoid nematic transition in these systems. We represent an ellipsoid of revolution (ER) with a unit vector \hat{n} (also called director) along the symmetry axis and the center of mass position vector as shown by the arrows in Fig. 6.1. ER volume is kept at $\pi/6$, which is equal to the volume of a sphere of unit diameter $d = 1$. To simulate the particles with highly directional bonding properties, the hard ellipsoidal particle is superimposed with conical patches, as shown in Fig. 6.1. The pair potential between particle i, j with director $\hat{\mathbf{n}}_i, \hat{\mathbf{n}}_j$ and inter-particle distance \mathbf{r}_{ij} is defined as,

$$U_{i,j} = \begin{cases} -u_\circ \cdot \sigma_{i,j}(\mathbf{r}_{i,j}, \hat{\mathbf{n}}_i, \hat{\mathbf{n}}_j) \cdot \chi_{i,j}(\hat{\mathbf{r}}_{i,j}, \hat{\mathbf{n}}_i, \hat{\mathbf{n}}_j) & \\ \infty & \text{Hardcore} \quad \text{overlap} \end{cases} \quad (6.1)$$

Where u is the depth of the square well potential with the interaction range $\epsilon = 0.1$. We define $h_{i,j}(\mathbf{r}_{i,j}, \hat{\mathbf{n}}_i, \hat{\mathbf{n}}_j)$ as the distance between the surfaces of the hard cores, calculated by using ellipsoids contact function (ECF)[172]. $\sigma_{i,j}$ and $\chi_{i,j}$ is defined as,

$$\sigma_{i,j} = \begin{cases} 1 & h_{i,j} < \epsilon \\ 0 & Otherwise \end{cases} \quad (6.2)$$

$$\chi_{i,j} = \begin{cases} 1 & |\hat{\mathbf{r}}_{ij} \cdot \hat{\mathbf{n}}_i| \geq \cos(\omega), |\hat{\mathbf{r}}_{ji} \cdot \hat{\mathbf{n}}_j| \geq \cos(\omega) \\ 0 & Otherwise \end{cases} \quad (6.3)$$

The patches are located on the opposite end of the major axis, and ω is the patch angle. In the present work, we are not restricting the number of bonds per patch but observed that by tuning ω and p the maximum number of bonds formed per patch can be controlled.

6.2.1 Brownian Cluster Dynamics

Brownian Cluster Dynamics (BCD) is an NVT Monte-Carlo simulation technique, which also reproduces the dynamics and kinetics of molecular dynamics (MD) simulations for square-well potential [196]. BCD consists of 2 steps. The first is the cluster construction step, and the second is the movement step. In the cluster construction step, when 2 patchy ellipsoidal particles are within each other's interaction range, a bond is formed with probability α . If a bond already exists, then they are broken with probability β . Thus, the probability for a bond to exist is given $P = \alpha/(\alpha + \beta)$, such that the potential is given by $u = \ln(1 - P)$. The bond formation and disassociation lead to the formation of clusters, which is identified as the collection of ellipsoidal particles bonded through the patches. For the sake of calculation, a monomer is considered as a cluster of size 1. The movement step of the ellipsoidal particles comprises both translation and rotational motion. In the movement step, the center of mass of every ellipsoidal particle is translated with a small step size s_t .

For the t_{sim} movement steps, the center of mass undergoes a random walk such that the mean squared displacement is given by $t_{sim}s_t^2$. As we make the step size very small, the center of mass undergoes a Brownian motion with physical time given by $t_0 = t_{sim}s_t^2$. Where unit of time t_0 is defined as the time taken by the center of mass of an ellipsoid to travel a unit distance[172]. The orientation of the symmetry axis of the ellipsoid undergoes a random walk on a 2 dimensional plane with a step size s_r in a random direction which mimics rational motion as shown by Varma et al. [172]. If either of the movement steps leads to the hardcore overlapping with each other or breaking an already formed bond, then that movement step of that particular ellipsoid is rejected. We have already shown that if the step size is smaller than $0.005d$, the diffusion coefficient of the ellipsoidal particle obtained from BCD agrees with the analytical calculation of Perrin et al. [172].

6.2.2 NPT simulation in a floppy box

We also performed a Monte-Carlo NPT simulation to calculate the phase diagram accurately. A random distribution of the ellipsoidal particles is taken in a cubic box[197, 198] as the initial configuration. For this configuration, a particle is randomly selected, and an attempt is made to move the center of mass with a step length $\pm\delta s$, which is randomly selected from the range $0.1d - 0.005d$. Similar to the NVT simulation, we also perform rotational movement using a quaternion over \hat{n} , by an angle $\pm\delta\theta$, which is randomly selected within the range $0.02 - 0.01$. After the movement steps, an attempt is made to change the volume and shape of the box by randomly selecting one of the edges of the simulation box and changing its edge vector with some random displacement by $\pm\delta r$, within the range $\pm0.5 - \pm0.005$. The new configuration is accepted using the metropolis Monte-Carlo method. We make sure that the acceptance ratio is always between $30 - 40\%$. When the acceptance

ratio falls below 30%, we reduce the length of the step size by a factor 0.95. In the case the acceptance ratio increases beyond 40%, we increase the step length through the factor 0.95 as well. To avoid any unphysical shape of the simulation box, we use the lattice reduction technique [199] as well as restrict the angles between edges in the range $30^\circ - 150^\circ$ [200]. Simulation starts at a fixed temperature while varying pressure from low to high, up to the desired value.

6.3 Results

6.3.1 Structural properties

To predict equilibrium structures at various temperatures and pressures, we performed floppy box simulation [201] with very few numbers of particles in the range of 2 to 8 as shown in Fig. 6.2. In this method, the shape and volume of the box change at a particular pressure and temperature. We initialize the system with random positional and orientation distribution of the spheroids within a cubic box. At constant temperature, the pressure varies from lower to higher values till the desired pressure is reached. For the equilibration of the ellipsoidal particle, we perform the random translation and rotation of the ellipse for $10^6 - 10^7$ steps until the number of bonded neighbors per particle remains constant. The structures thus formed are replicated in a larger box with particle numbers between $600 - 1000$, and the system is then again equilibrated. To identify different structures formed inside the box, we follow the criteria as proposed by Vissers et al. [202]. Structures with the same number of nearest neighbors are considered identical if the difference in the respective densities of structures is less than 0.05 as well as if the difference between the pair correlation and orientational correlation function is between 0.9 – 1. With this

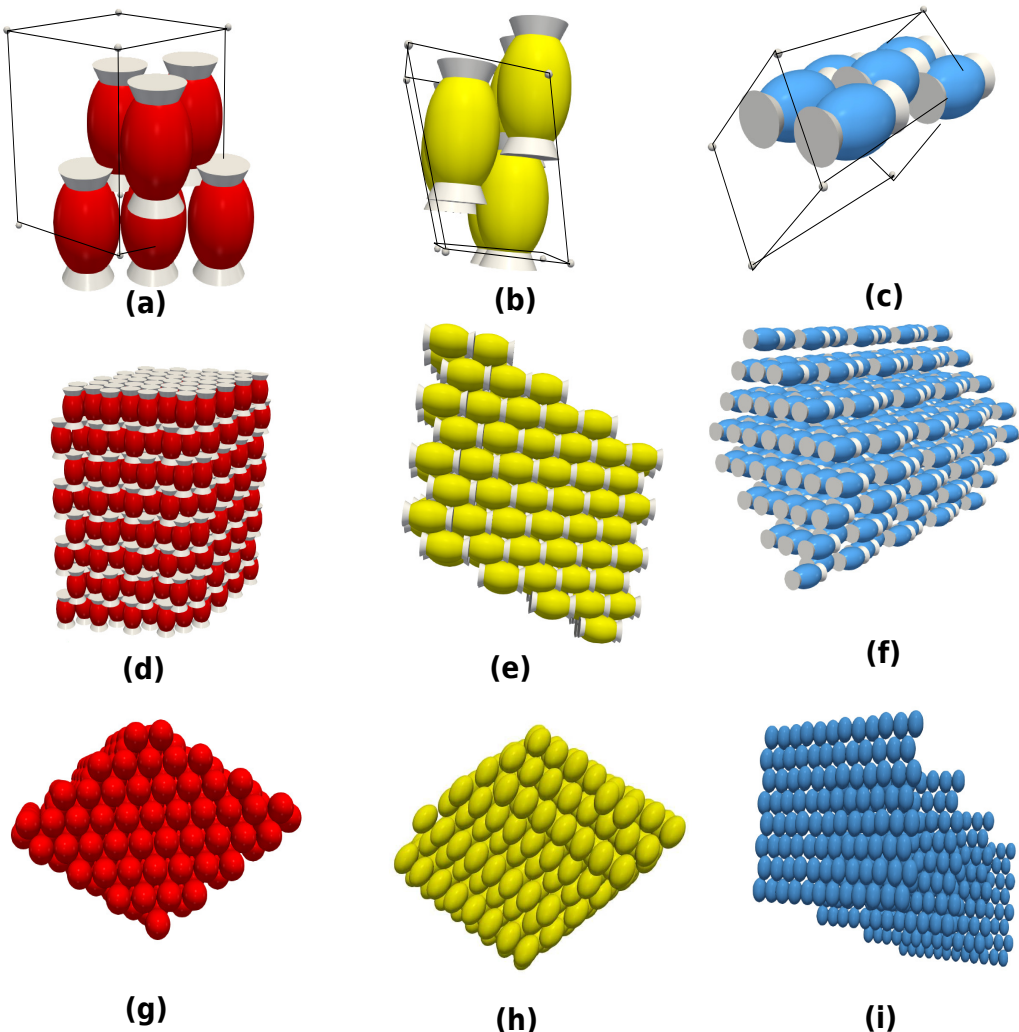


FIGURE 6.2: Unit cell (top row) of different crystal structures as predicted by the floppy simulation and corresponding bulk system (bottom row), with $p = 1.5$ and $\cos(\omega) = 0.9$ (a) Type I crystal (b) Type II crystal and (c) monolayer. (d) Corresponds to the Type-I crystal, at $k_B T/u_o = 0.15$ and $p\sigma^3/k_B T = 0.5$. (e) Type-II crystal at $k_B T/u_o = 0.2$ and $p\sigma^3/k_B T = 10$. (f) The monolayer at $k_B T/u_o = 0.2$ and $p\sigma^3/k_B T = 6$. The corresponding top view of the crystal is shown (g) Type I, (h) Type II, and (i) monolayer. Patches have been shown with white color cones.

criterion, three stable structures (Fig. 6.2) were identified for the relevant range of temperature and pressure.

The unit cell as obtained from the floppy box simulation for Type I Fig. 6.2(a), Type II Fig. 6.2(b) and monolayer Fig. 6.2(c) are shown. The structures formed with

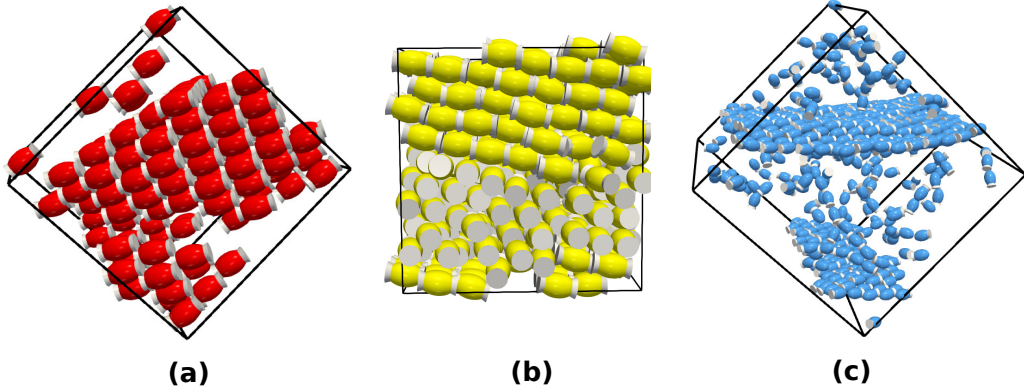


FIGURE 6.3: The structures predicted by floppy simulation, obtained in the NVT simulation for the system with $p = 1.5$ and $\cos(\omega) = 0.9$. From left to right. Red corresponds to the Type-I crystal, at $k_B T/u_o = 0.15$ and $\phi = 0.55$. Yellow: Type-II crystal at $k_B T/u_o = 0.20$ and $\phi = 0.55$. While blue is the monolayer at $k_B T/u_o = 0.114$ and $\phi = 0.06$. Patches have been shown with white color cones along the \hat{n} of spheroids.

a small number of particles are replicated to form bulk crystals, which are further equilibrated using floppy box simulation. The structure thus formed is shown in Fig. 6.2 (d) for Type I crystal, fig. 6.2 (e) for Type II crystal and fig. 6.2 (e) for free-standing monolayer. In type-I crystal, each particle is bonded with its 6 nearest neighbors, and the patch vector is always perpendicular to the plan of stacking. Thus, the bonds are formed with ellipsoidal particles along the layers as well as with adjacent layers of ellipsoids, as can be observed in Fig. 6.2(g). In Type II crystal, particles are bonded only within the layer, with a maximum of 4 bonded nearest neighbors, and the patch vector can be observed aligned along a single layer of stacking see Fig. 6.2(h). The layers are arranged in a periodic manner, and interaction between layers is only through the hardcore repulsion see Fig. 6.3(b). In Type II crystal, we observe that the adjacent layers are shifted in the direction perpendicular to the patch vector compared to Type I crystal. At moderate temperature and relatively smaller volume fraction (low pressure), the periodic stacking of the Type-II crystal breaks, leading to the random orientation of the layers. This

leads to the formation of a stable configuration of monolayer free-standing films, as shown in Fig. 6.2(f) as well as clearly observed in Fig. 6.2(i) (top view). These structures were further simulated using the NVT ensemble, starting from a random distribution of ellipsoidal particles with periodic boundary conditions. Depending on ϕ and the interaction strength, we obtained the same structure as observed in the floppy box simulation. Type-I crystals (Fig. 6.3(a)) are formed when energy is favored over entropy, which happens at low temperatures regime. The coexistence of the free-standing monolayer film with the gas particles can be observed (see Supplementary Materials II) for a system equilibrated in NVT ensemble (Fig. 6.3(c)) at $\phi = 0.06$ and $k_B T/u_o = 0.114$, as expected from the floppy box simulation (Fig. 6.2(b)).

The change in the number of bonded neighbors can be observed in the constant NVT simulation. In Fig. 6.4(a), we have shown the evolution of the average number of bonded neighbors ZPI for $\phi = 0.55$ at $u_o/k_B T = 0.114$. As the system starts to aggregate from a random ellipsoidal distribution, the ZPI increases over time until it reaches a steady state, which in the present case is < 4 . In Fig. 6.4(b), we have shown the evolution of the fraction of particles bonded to a particular ellipsoid n_f^b as a function of time, such that $b = 2$ means 2 particles are bonded to an ellipsoidal particle. We can observe that n_f^b for $b = 2$ and 3 are maximum at initial times, then the fraction of $b = 4$ number of bonds increases, indicating the formation of an ordered structure. After a time of $t/t_0 > 1000$, we observe particles having 5 and 6 bonds increases, leading to the formation of bulk crystals. In Fig. 6.4(c) at $K_B T/u_o = 0.2$ and $\phi = 0.55$ we observe the formation of Type-II crystal, the average number of bonded neighbors is below 4 as Type-I crystal. The evolution of the fraction of particles having 2 and 3 bonds decreases with time, and the fraction of particles having 4 bonds increases with time, similar to Type I crystal. We also

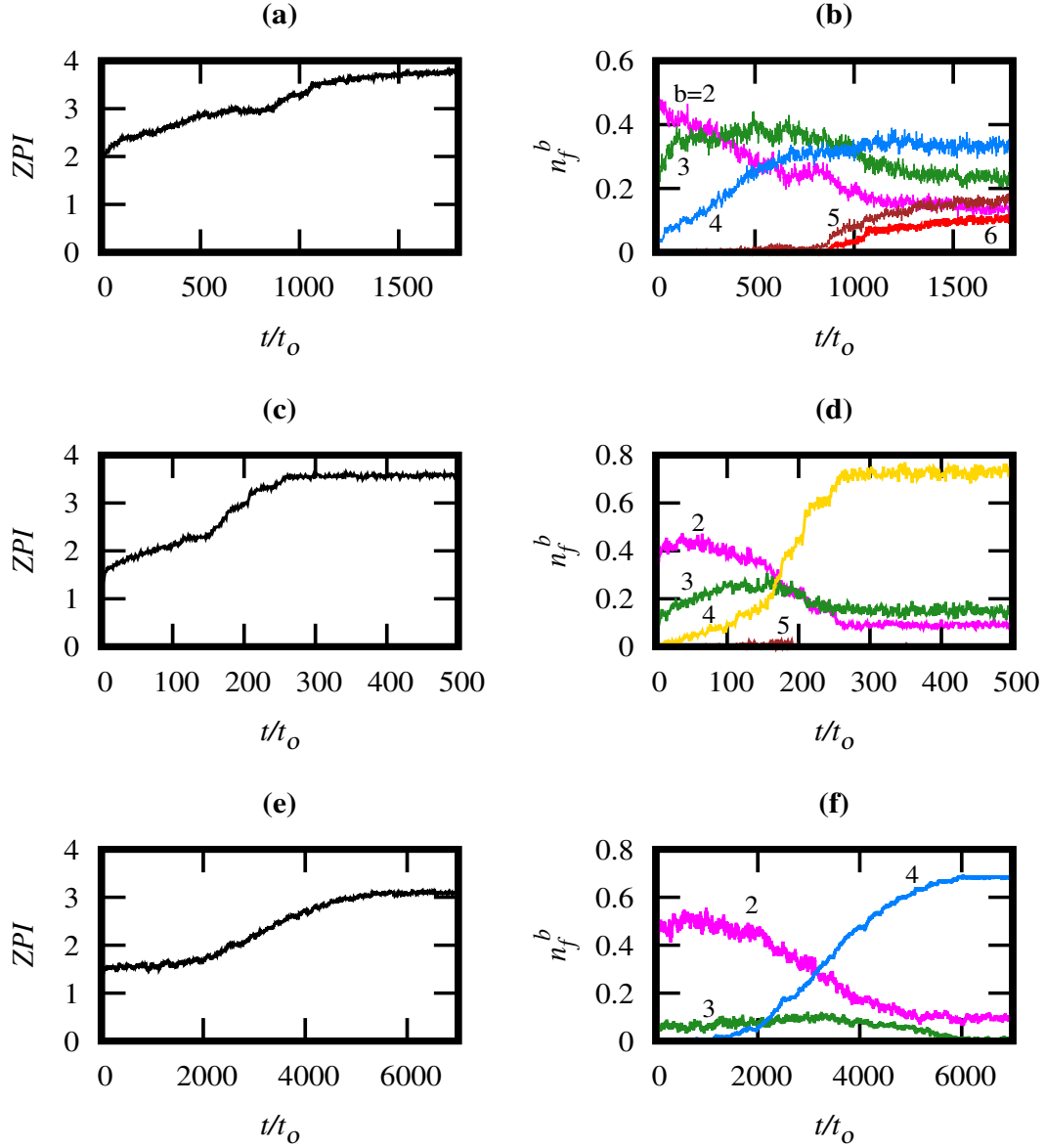


FIGURE 6.4: Average bonded nearest neighbor; ZPI shown as a function of time on the left, and the particle fraction with the given number of bonded neighbors, as indicated in the figure, is shown on the right. (a), (b) Type-I crystal at $k_B T/u_o = 0.15$ and $\phi = 0.55$. (c), (d) Type-II crystal at $k_B T/u_o = 0.20$ and $\phi = 0.55$. (e), (f) Monolayer at $k_B T/u_o = 0.114$ and $\phi = 0.06$.

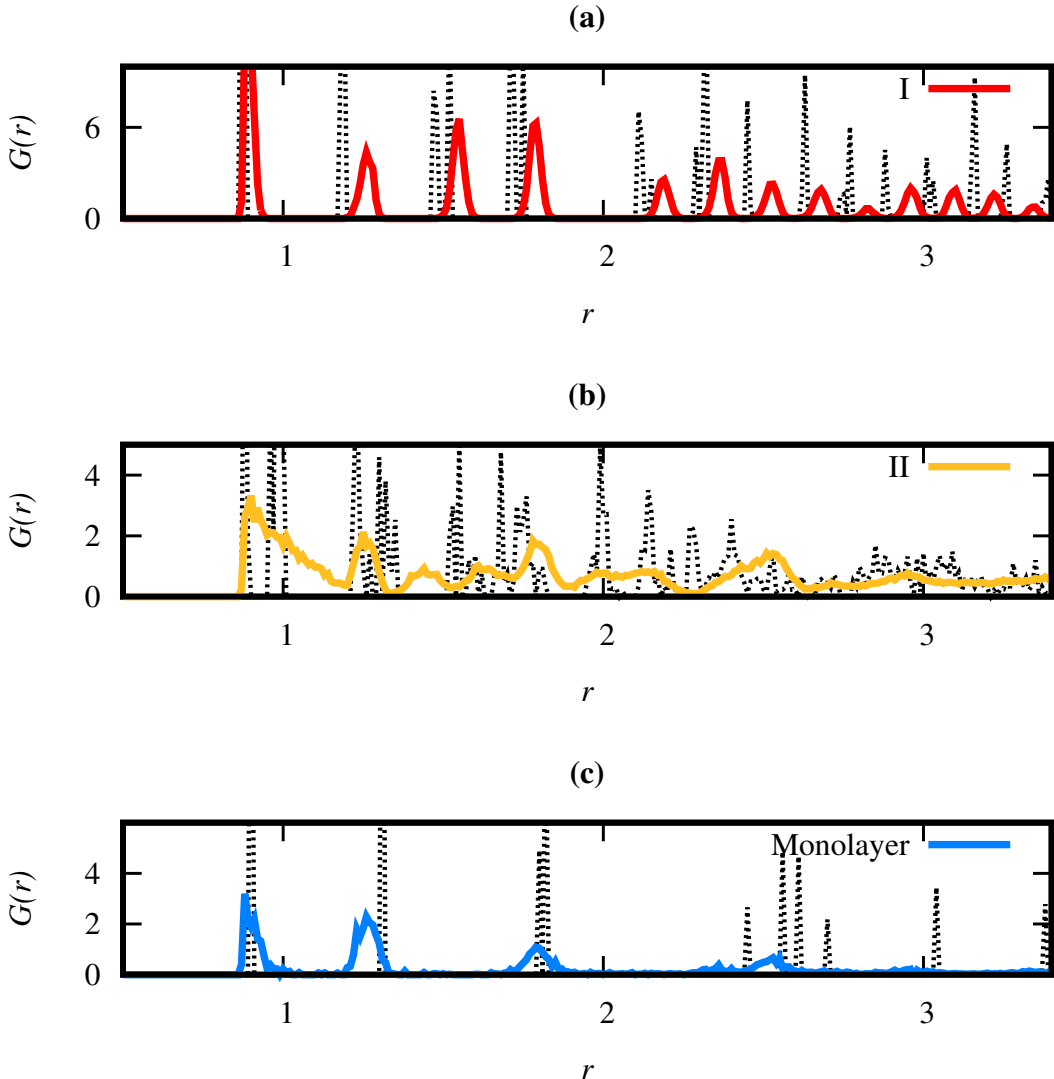


FIGURE 6.5: Pair correlation function $G(r)$ corresponding to the NVT ensemble (solid line) is compared with the structure predicted by the floppy simulation (dotted line). (a) Type I crystal at $k_BT/u_o = 0.15$ and $\phi = 0.55$ (b) Type-II crystal at $k_BT/u_o = 0.20$ and $\phi = 0.55$. (c) Monolayer at $k_BT/u_o = 0.20$ and $\phi = 0.55$.

observe for longer times, the fraction of particles having 5 and 6 bonds are absent (fig.6.4(d))for these crystals, essentially differentiating Type I from Type II crystals. In Fig. 6.4(e), we have shown the evolution of ZPI as a function of time for the case where the monolayer is formed. Here, we also observe that the n_f^4 increases and stagnates while n_f^3 and n_f^2 decrease with time, similar to the Type II crystal.

In Fig. 6.5, we have shown the pair correlation function $G(r)$ as obtained from the floppy box simulation, which is compared with the structure obtained from the NVT simulation. The $G(r)$ obtained from the floppy box simulation shows a sharp peak as there is no presence of gas particles, whereas, from the NVT simulation, we obtained broad peaks. The peaks of the Type-I crystal as obtained from floppy box simulation and NVT simulation, almost agree with each other, confirming that we have reached a near-equilibrium state as shown in Fig. 6.5(a). In an NVT simulation, the crystal coexists with the gas particle, whereas in a floppy box simulation, only the equilibrium crystal will be present. Thus, when we calculate the $G(r)$ of these systems in an NVT ensemble, we observe a shift in the position of peaks due to the presence of gas particles. The Type II crystals are structurally different from the Type I crystals as we can observe more peaks in $G(r)$ see Fig. 6.5. The reason is observed from floppy box simulation, see Fig 6.1(b), as there is a slight shift in the particle position between adjacent layers for Type-II crystals. All the peaks in $G(r)$ of the monolayer can be observed both in Type I and Type II crystals, indicating that the arrangement of a single layer is the same in both the crystal types see Fig. 6.5(c).

For the spherical particle of the 2 patch, it has already been shown that they form the Kagome lattice [203]. For the prolate ellipsoidal particle, we have calculated the distribution $g(\mathbf{n}_i \cdot \mathbf{n}_j)$, where \mathbf{n}_i is the unit vector along the patch for the i^{th} particle. In Fig. 6.6(a), we can observe that in all the three types of crystal, we observe only 2 peaks at ~ 0 and $\sim \pi$, which means that all patch vectors are parallel or antiparallel to each other. We can also observe that the width of the distribution is wider for Type-II and monolayer structures because they have more freedom to move within the bonds as the maximum number of neighbors is ≤ 4 , compared to Type-I crystal, which is ≤ 6 . To distinguish between different crystal structures, we calculated \bar{q}_6

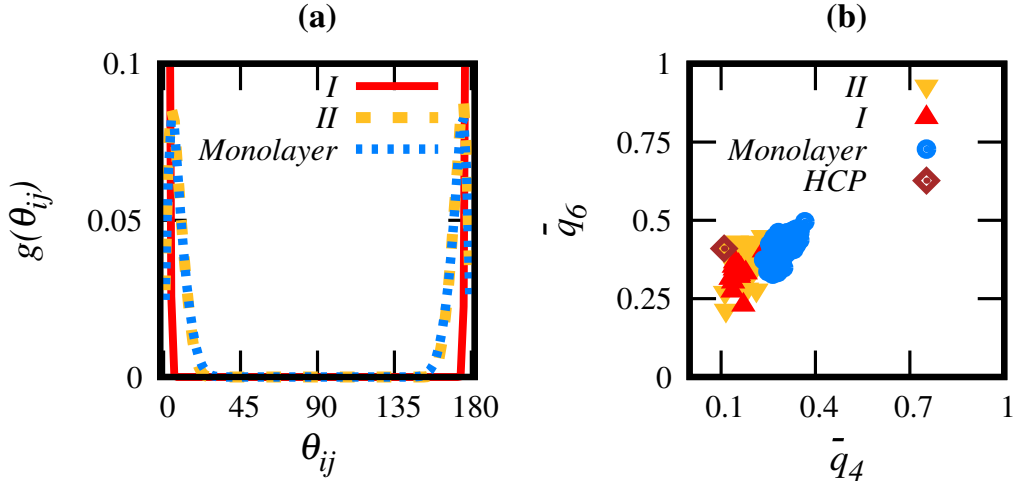


FIGURE 6.6: \bar{q}_6 and \bar{q}_4 have been shown for different structures, indicating the presence of ordered phases obtained in NVT ensembles.

and \bar{q}_4 , as shown in Fig.6.6(b). We observe that all the ordered structures are closer to the HCP crystal value. We believe that as a limited number of directional bonds are formed due to the finite patch width and patch angle, the system prefers the HCP arrangement at a finite temperature.

6.3.2 Phase diagram

To draw the phase diagram, we calculated the chemical potential of the crystal from the free energy calculation using the Einstein crystal method [201, 120, 121, 122]. To calculate the energy of the fluid phase, we used *SGMC*, which is discussed in Chapter 3. We first calculated the equilibrium cluster size distribution and then the free energy. Fig 6.7 shows the equilibrium cluster size distribution ρ_n/ρ (where ρ_n is the density of the cluster with size n such that $\rho = \rho_1 + \rho_2 + \rho_3 \dots + \rho_n \dots$) calculated at different temperatures (as given in the caption) by using *SGMC* (square points) and compared with the result obtained by using *NVT* (solid lines).

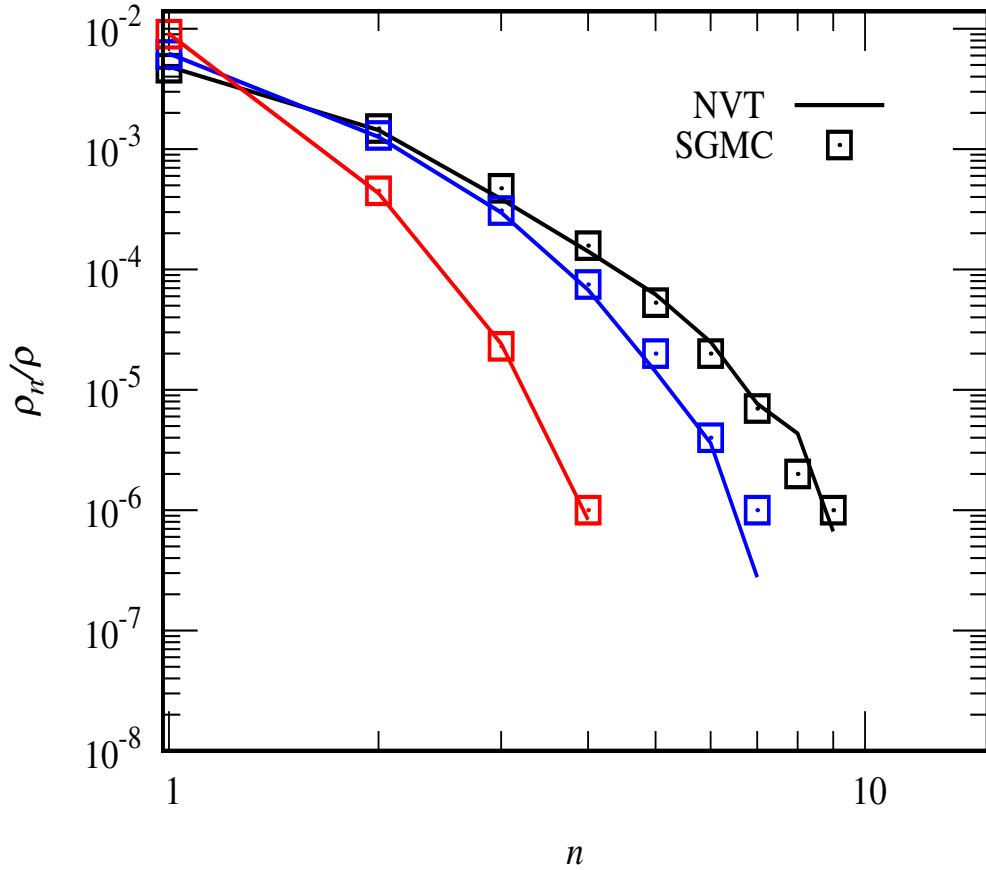


FIGURE 6.7: Equilibrium cluster distribution is shown for *SGMC* calculation (square points) done at $\phi = 0.01$ and temperature $k_B T/u_0 = 0.16$ (red squares), 0.123 (blue squares) and 0.114 (black squares) and compared with the *NVT* (solid lines).

The co-existence point of two states is identified when the different phases (crystal structures and fluid) have the same chemical potentials, pressure, and temperature, as shown in Fig. 6.8(a). At $K_B T/u_0 = 0.22$, we can observe that as the pressure is increased, the chemical potential also increases for the crystal structures. For $pd^3/k_B T \sim 7.2$, we observe that $\mu/k_B T$ of both monolayer crystal and Type II crystal intersect, which is a coexistence point. $pd^3/k_B T < 7.2$, we observe that the monolayer has a minimum chemical potential, thus making it the most stable structure. At $pd^3/k_B T \sim 10$, we observe that $\mu/k_B T$ of both Type I and Type II cross over each other, giving us another coexistence point. We also observe that

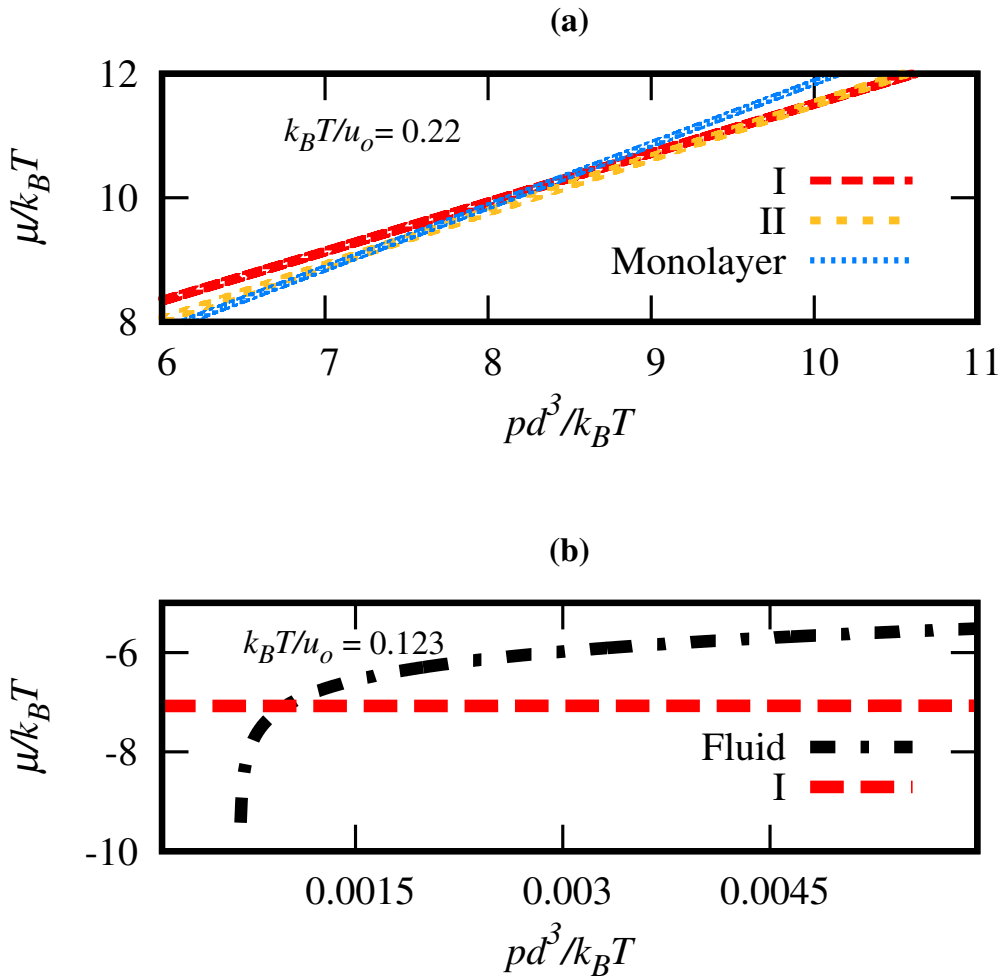


FIGURE 6.8: $p-\mu$ curve shown for different phases at $k_BT/u_o = 0.22$. p have been expressed in the unit of k_BT/d^3 , while μ in the unit of k_BT . (a) The intersection point of the two lines shows the coexistence of Type I crystal and fluid. (b) The intersecting line shows the phase coexistence of Type I, Type II, and monolayer crystals.

$7.2 < pd^3/k_B T < 10$ crystal Type I has the minimum chemical potential, thus making it the most stable structure at these pressures and temperatures. When $pd^3/k_B T > 10$, Type I is the stable structure as it has the minimum chemical potential of all three crystals. In order to calculate the phase diagram through thermodynamic integration [115], the free energy of the fluid was calculated using NVT and semi-grand canonical simulation [117, 118] see Supplementary Material I.

We calculated the chemical potential $\mu/k_B T$ [204] from the free energy calculation shown in Fig. 6.8(b) for $k_B T/u_\circ = 0.123$. The point of intersection of the fluid curve and the crystal Type-I is identified as a coexistence point on the phase diagram.

Fig.6.9(a) shows the phase diagram in the $T - p$ plane calculated by integrating the Clausius-Clapeyron equation using the Kofke method [202, 205, 206] see Supplementary Materials I. At low pressure and temperature regimes, we can observe the coexistence line between the Type I crystal and the fluid. Here, we would like to mention that we always observed the formation of a metastable monolayer when simulated from a random ellipsoidal configuration. In the presence of a seed of Type I, we observed that the growth of the monolayer was suppressed, and the Type I crystal started to grow. Thus, Type-I crystal was the most stable configuration confirmed through our chemical potential calculation in this range. Pressure along the coexistence line of Type-I/fluid increases monotonically with increasing temperature. At temperature $k_B T/u_\circ \sim 0.23$, the fluid co-exists with the monolayer. As we further increase the temperature, the coexistence pressure increases further, leading to the random stacking of monolayers, which ultimately forms Type-II crystal. The co-existence line between Type I / Type II becomes nearly parallel to the pressure axis for the high-temperature region, indicating that for very high temperature $k_B T/u_\circ \geq 0.28$ and $pd^3/k_B T \geq 0.35$ only fluid and Type II can co-exist.

In fig.6.9(b) we have shown the $\phi-T$ phase diagram calculated using thermodynamic integration. We observe the coexistence of the fluid phase and the Type-I crystal at low temperatures and volume fractions. The monolayer, although confined to a very small region in the phase diagram of T and ρ is a stable configuration. Increasing the temperature from ~ 0.22 leads the fluid to coexist with Type-I, monolayer, and Type-II, which we have also confirmed using the chemical potential calculation. Upon further increase in temperature, a coexistence between fluid and Type-II can

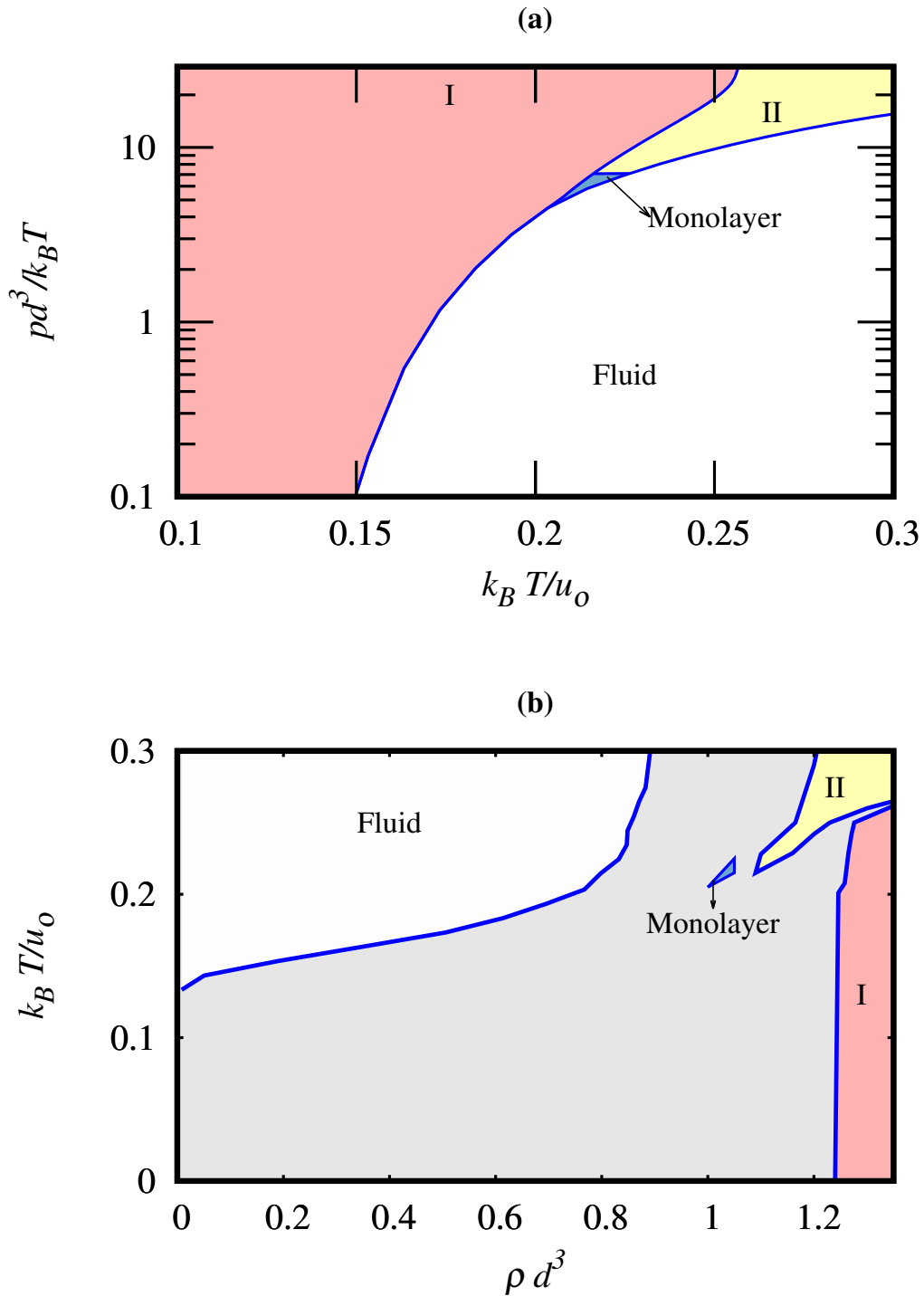


FIGURE 6.9: (a) $p - T$ phase-diagram exhibiting the location of various phases have been shown for the system of spheroids with $p = 1.5$ and $\cos(\omega) = 0.9$. p have been expressed in the unit of $k_B T/d^3$, while $k_B T$ in the unit of u_o . The blue solid line represents the coexistence point among the various phases. (b) $\rho - T$ phase-diagram showing the location of various phases for the system of spheroids with $p = 1.5$ and $\cos(\omega) = 0.9$. ρ have been expressed in the unit of $1/d^3$. The blue solid line represents the coexistence point.

only be observed. As the density increases, we observe that the forbidden region between Type-I and Type-II narrows down as well. We would also like to mention that we did not observe a metastable liquid-gas transition in the present study.

6.4 Discussion and Conclusion

Liu et al. [180] have shown experimentally that by varying the patch angle between $55^\circ - 97^\circ$ of the prolate particle, they obtained $2D$ and quasi $2D$ structures. We have shown for one particular patch angle that thermodynamically stable monolayer free-standing film can be formed. As shown experimentally, the long-range ordered $2D$ [180] structure was seen only for small patch angles consistent with the present work. It was shown that using the metal-organic framework and depletion interaction induced by ionic amphiphiles, a variety of colloidal superstructures were created, which included $1D$ chains, crystalline $2D$ films, and quasi $3D$ supercrystals on a surface. They changed the shape of the anisotropic particle to get the desired structure. In the present work, we have kept the shape of the particle and the interaction range the same while changing the thermodynamics of the systems, obtaining free-standing monolayer $2D$ films and $3D$ super crystal structures without the help of interfaces.

In the present work, we have simulated the aggregation of prolate particles with 2 patches that interact via the Kern-Frenkel potential. The aspect ratio of the particles is 1.5; thus, the system will never undergo a nematic transition. The stability of the crystalline structure was established using the floppy box simulation method, where we observed 2 type of crystal structures. Type I crystal had particles with valency > 4 , while Type II crystal had particles with almost valency 3. Surprisingly,

we also observed the presence of a thermodynamically stable monolayer of free-standing thin film as well. The phase diagram of the system was obtained by using thermodynamic integration, which also confirmed the existence of the monolayer of colloids. The calculation of the bond orientation parameter showed that the crystal is closer to the HCP arrangement. The phase diagram was calculated by thermodynamic integration that confirmed the existence of the monolayer over a small region. It will be interesting to study the phase behavior of different aspect ratios of the prolate and oblate particles to verify the existence of the monolayer with the presence of the nematic phase.

Chapter 7

**Breaking the size constraint for
nanocages using annular patchy
particles**

Abstract

Engineering structures like nanocages, shells, and containers by self-assembly of colloids is a challenging problem. The challenges are to define the shape of the individual subunits and to control the radius of the closed shell structures. In this work, we have proposed a simple model for the subunit, which comprises spheroidal or spherical hardcore decorated with an annular patch. The self-assembly of these building blocks leads to the formation of monodispersed spherical cages (close shells) or containers (curved clusters). The curvature of the shell is analytically related to only the patch angle of the building blocks and independent of the shape of the subunits. This model with only one control parameter can be used to engineer cages with the desired radius, which has also been verified using thermodynamic calculations. In the phase diagram of the system, 4 phases are identified, which include gas, closed shell, partially closed (containers) shell, and percolated structure. When the diameter of the spherical cages formed is small, we observe an icosahedral symmetry similar to virus capsids. We also observed that the kinetics of the cage formation are very similar to the nucleation and growth kinetics of viruses and are key factors in determining the yield of closed shells.

7.1 Introduction

With the advancement in our understanding of nanoscale phenomena, researchers have found ways to synthesize different types of nanocages. The possible use of these cages are in targeted drug delivery [207, 208], nanoreactors [209], nanocontainers [210] etc. Recently it was shown that using nanocages, it is possible to trap viruses, thus giving us a new way of treatment for viral infections [211]. The close nanocluster has been studied experimentally [212, 213, 214] as well as by simulation [215, 216, 217, 218]. Experimentally, nanocages are formed either by biological molecules [219, 220] or through chemical route [221, 222, 223].

The patchy colloidal particle with directional interaction has been used as a model for aggregation of supra molecular structures[157, 158], water molecule, virus capsid [216], engineering super lattices [224, 225] etc. Few studies have focused on patchy particles to mimic the cage formation in nanoscale [226, 227, 228, 229, 230, 231], which lead to highly mono-dispersed structures for a very specific type of anisotropic particles [231]. It is challenging to use different shapes of patchy particles and to control the size of the shell-like structures [232, 233] at the same time. In the present work, we have proposed a simple annular patchy potential leading to the formation of monodisperse spherical shells by tuning only the patch angle, irrespective of the shape of the anisotropic spheroids. The present model of annular patches thus addresses the size constraint challenges of the closed shell irrespective of the shape of the patchy particles. These structures will find application in vaccine production, acting as nanoreactors [209], drug delivery systems, etc. [207, 208]

In the biological world, we know that subunits of certain kinds of viruses aggregate together to form spherical closed structures with icosahedral symmetry. At very low temperatures, the nucleation rates of these subunits are very high, and the yield of

the closed shells falls, leading to partially open shells, as reported in the kinetic study of the shell growth of viral capsids [234] in solution. It was also shown that when the number of subunits being part of the closed structure increases, the size of the shell increases. It was also observed that subunits having six near neighbors increase dramatically compared to the subunits having five near neighbors [235]. Mosayeb et al.[215] studied similar structures, by letting the subunits move on the surface of a sphere whose radius was fixed. They showed that for a small sphere radius, the subunit was distributed on the surface of the sphere with icosahedral symmetry similar to virus capsids, and as the diameter increased, the symmetry vanished. In our present model, we were able to observe that annular patchy particles formed closed structures, similar to spherical viruses, through self-assembly. The closed structure formed in the present model shows icosahedra symmetry if the diameter is comparable to the size of the subunit, and as the diameter increases, the symmetry breaks down.

To study the kinetics and structure of the system, we have used the Brownian cluster dynamics (BCD)[97] method, which is a well-known kinetic Monte Carlo method. Using Brownian cluster dynamics, a variety of colloidal systems have been modeled with discontinuous potential [97, 99, 172] for studying both irreversible [154, 100, 155, 156] and reversible [66, 153, 129, 236] system. It was shown that the structure, kinetics, and dynamics of BCD and event-driven molecular dynamics simulation are the same [153].

In the simulation section, we discuss in detail the proposed annular potential, along with the cluster formation and dynamics undertaken by the subunits in the kinetic Monte Carlo technique (BCD). In the results section, the formation of cages, its dependence on the volume fraction temperature, and various other parameters are explored in detail. The radius of the cages formed in the NVT ensemble is calculated

analytically and compared with the modified Gibbs ensemble Monte Carlo method. The kinetics of the cage formation, along with the local order of the cages, are studied, followed by a conclusion in the last section.

7.2 Model and Simulation method

In the present work, the subunits considered are spheroids (oblate, prolate) and spheres with an aspect ratio $p = a/b$, where a and b are the semi-major and semi-minor axes. All the subunits have the same volume $\pi d^3/6$, where d is the diameter of the sphere, which is kept as unity in the present work.

The subunits interact with each other through a hard-core potential and an annular patch, where patch orientation $\hat{\mathbf{n}}$, is considered along the direction of the symmetry axis of spheroids. We define the annular patch by a modified Kern-Frenkel potential, given as,

$$U_{i,j} = \begin{cases} -u \cdot \sigma_{ij}(\mathbf{r}_{ij}; \hat{\mathbf{n}}_i; \hat{\mathbf{n}}_j) \cdot \chi_{ij}(\hat{\mathbf{r}}_{ij}; \hat{\mathbf{n}}_i; \hat{\mathbf{n}}_j) & \\ \infty & \text{Hardcore} \quad \text{overlap} \end{cases} \quad (7.1)$$

where $\hat{\mathbf{n}}_i$, $\hat{\mathbf{n}}_j$ is the patch vector and \mathbf{r}_{ij} is the distance between the center of mass of subunits i and j respectively. u is the depth of the square well potential with the interaction range ϵ , where we have the energy scaled in terms of $u/k_B T$. We define $h_{i,j}(\mathbf{r}_{ij}, \hat{\mathbf{n}}_i, \hat{\mathbf{n}}_j)$ as the distance from the surface of the spheroid where the patches are attached, which is calculated by using ellipsoids contact function (ECF)[172]. σ_{ij} and χ_{ij} is defined as,

$$\sigma_{ij} = \begin{cases} 1 & h_{i,j} < \epsilon \\ 0 & \text{Otherwise} \end{cases} \quad (7.2)$$

$$\chi_{ij} = \begin{cases} 1 & \cos(\Omega^\circ + \Delta\omega^\circ) \geq \hat{\mathbf{r}}_{ij} \cdot \hat{\mathbf{n}}_i \geq \cos(\Omega^\circ - \Delta\omega^\circ), \\ & \cos(\Omega^\circ + \Delta\omega^\circ) \geq \hat{\mathbf{r}}_{ji} \cdot \hat{\mathbf{n}}_j \geq \cos(\Omega^\circ - \Delta\omega^\circ) \\ 0 & \text{Otherwise} \end{cases} \quad (7.3)$$

where $\Delta\omega^\circ$ is the angular width of the patch located at a semi-conic angle Ω° , along the patch vector of the subunit as shown in Fig. 7.1 (a).

To study the structure and kinetics of the self-assembly, we have used Brownian cluster dynamics (BCD)[97] simulation technique, a kinetic NVT Monte-Carlo(MC) scheme. The simulation starts with N number of particles (subunits), randomly scattered in a cubical box of length L . Volume fraction of the system is defined as, $\phi = \frac{\pi d^3 N}{6L^3}$. A simulation step consists of a movement step and a cluster construction step. For the movement step, we select subunits randomly $2N$ times and then either rotate the subunit with respect to the director or translate the center of mass of the subunit, with equal probability. In this way, on average, every particle has performed one rotational and one translation movement step. For the translational movement, a center of mass of the subunit is displaced through a constant step length S_T , along a random direction. Similarly, for the rotational step, the unit vector \hat{n} is rotated with a fixed step length $S_R = |\hat{n} - \hat{n}'|$, where \hat{n} and \hat{n}' are the orientation of the director of the subunit before and after the rotation step. Prabhu et. al [99] have shown S_R and S_T , follows the relation $S_R^2 = 2S_T^2$. For the spheroidal particle, the translational and rotational step sizes are scaled with respect to the Perrins factor, which has been shown to mimic the single particle diffusion accurately [172]. If the movement of the subunit leads to the overlap of the hardcore particle or breakage of a bond, that movement step is rejected. After the movement step, we perform a cluster construction step. When the annular patches of the subunit are within

each other's range, a bond is formed with a probability α [157]. If the bond already exists, it is broken with a probability β_b , such that the probability for a bond to exist is given by $P = \alpha/(\alpha + \beta_b)$ such that $P = 1 - e^{-u/k_B T}$ [97], where $u/k_B T$ is a positive number. All the subunits connected through the bonds are defined as a cluster such that a monomer is a cluster of size 1. The movement step followed by a cluster construction step is considered as one simulation step. The relation between simulation step t_{sim} and physical time t_{Phy} , is given as $t_{Phy}/t_o = S_T^2 \cdot t_{sim}$ [97]. Such that t_o is the time taken for a single sphere to diffuse through its own diameter. By using bigger S_T , we can achieve larger t_{Phy} for the same number of simulation steps. But bigger S_T can also lead to more rejection, leading to nonphysical diffusivity and kinetics of the system. In the present work, S_T is set at $0.01d$ [172], which keeps the dynamics accurate without compromising on the computational efficiency. The kinetics is explored to the order of 10^4 physical time, with the number of subunits ranging between $N = 1000 - 4000$.

7.3 Results

7.3.1 Structural properties

Fig 7.1 shows the typical structures formed for different parameter ranges along with different kinds of subunits as given in the caption. The red color is used to indicate subunits having less than 5 bonded neighbors. The cyan and yellow-colored subunits have 5 and 6 bonded neighbors, respectively. In fig. 7.1, the grey subunits correspond to small-size clusters (monomers, dimers, trimers). These small clusters have been removed in the following images for better visualization. In Fig. 7.1(b), we observe highly monodispersed clusters having icosahedral symmetry, formed at

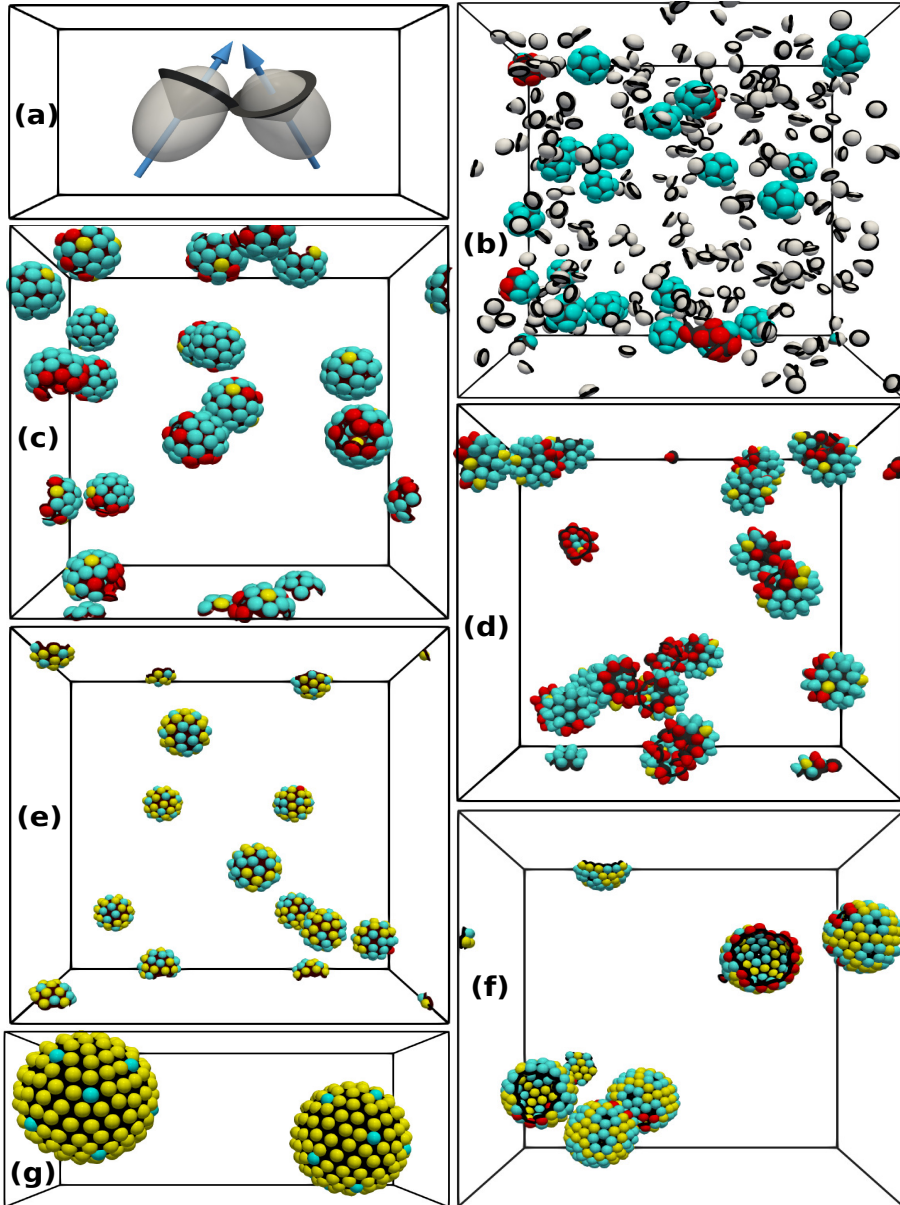


FIGURE 7.1: (a) Subunits with oblate hardcore (gray color), along with annular patches shown as (black) ring-like structure, and the arrows passing through the symmetry axis of the subunits represent the patch vector. All the subunits represented in grey color have less than 4 bonded neighbors. While red subunits have bonded neighbors < 5 . Cyan and yellow subunits have 5 and 6 bonded neighbors, respectively. (b) Oblate hardcore with annular patch forming mono-dispersed structures with icosahedral symmetry, shown at $k_B T/u_o = 0.115$, $\Omega^\circ = 60^\circ$, $\epsilon = 0.25$ and $\Delta\omega^\circ = 3^\circ$. Fully evolved closed shell is shown at $k_B T/u = 0.115$, $\Omega^\circ = 74^\circ$, $\epsilon = 0.25$ and $\Delta\omega^\circ = 3^\circ$, with (c) oblate ellipsoid, (d) prolate ellipsoid and (e) spherical subunits. In these systems, the small disordered clusters (monomers, dimers, trimers) are removed for better visualization. (f) Clusters formed for spherical subunit at, $k_B T/u = 0.137$ for $\Omega^\circ = 79.6^\circ$, $\epsilon = 0.1$ and $\Delta\omega^\circ = 4.5^\circ$, where we can also observe voids at the center of the pentagonally arranged spherical subunits. (g) Very large shells of spherical subunits formed at $k_B T/u = 0.142$ for $\Omega^\circ = 82^\circ$, $\epsilon = 0.4$ and $\Delta\omega^\circ = 3^\circ$.

$\Omega = 60^\circ$. The clusters consist of 12 subunits ($c_s = 12$), where each subunit has five bonded neighbors. As we increase Ω , the cluster size increases, and shells formed have subunits with six bonded neighbors (Fig. 7.1(c), (d), (e), (f), (g)), alongside five bonded neighbors. This is expected, as for the formation of a spherical closed structure, a combination of pentagons (5 bonded subunits) and hexagons (6 bonded subunits) are needed, an example being a virus capsid [215]. For $\Omega = 74.$, the formation of mono-dispersed close shells can be observed, which is shown for the systems having Fig. 7.1 (c) oblate (d)prolate, and (e) spherical-shaped subunits. The shells are closed irrespective of the shape of the hardcore, with the average number of subunits per shell $\bar{c}_S = 42$. Fig. 7.1(f) and (g), the snapshot shows larger closed structures with the number of subunits $c_S = 96$ and $c_S = 165$, formed at $\Omega^\circ = 79.6^\circ$ and 82° respectively. In all the snapshots, it is observed that the close structures formed are monodisperse in nature with respect to the radius of the closed shell structures.

In the present study, we observe four different types of clusters in the system. The clusters having subunits with random orientation of the patch vector are designated as disordered or gas clusters (G), the closed shell structure (C), partially closed shell (COD), and percolated clusters (P). The appearance of these structures at different temperatures and volume fractions ϕ [237], obtained from the simulations, is shown in Fig.7.2(a). A typical system with a particular annular patch having $\Omega^\circ = 74$, $\Delta\omega = 4.5^\circ$, and $\epsilon = 0.25$ is chosen in Fig.7.2. The specific parameters were selected such that the shells formed were neither too large, which would lead to a longer convergence time of the system to the final equilibrium, nor too small (Fig.7.1(b)) such that the diameter of the shell is comparable or bigger than the size of the constituent subunits. The self-assembled closed shell was identified by calculating the distance to the subunit from the center of mass r_{cm} (radius of the

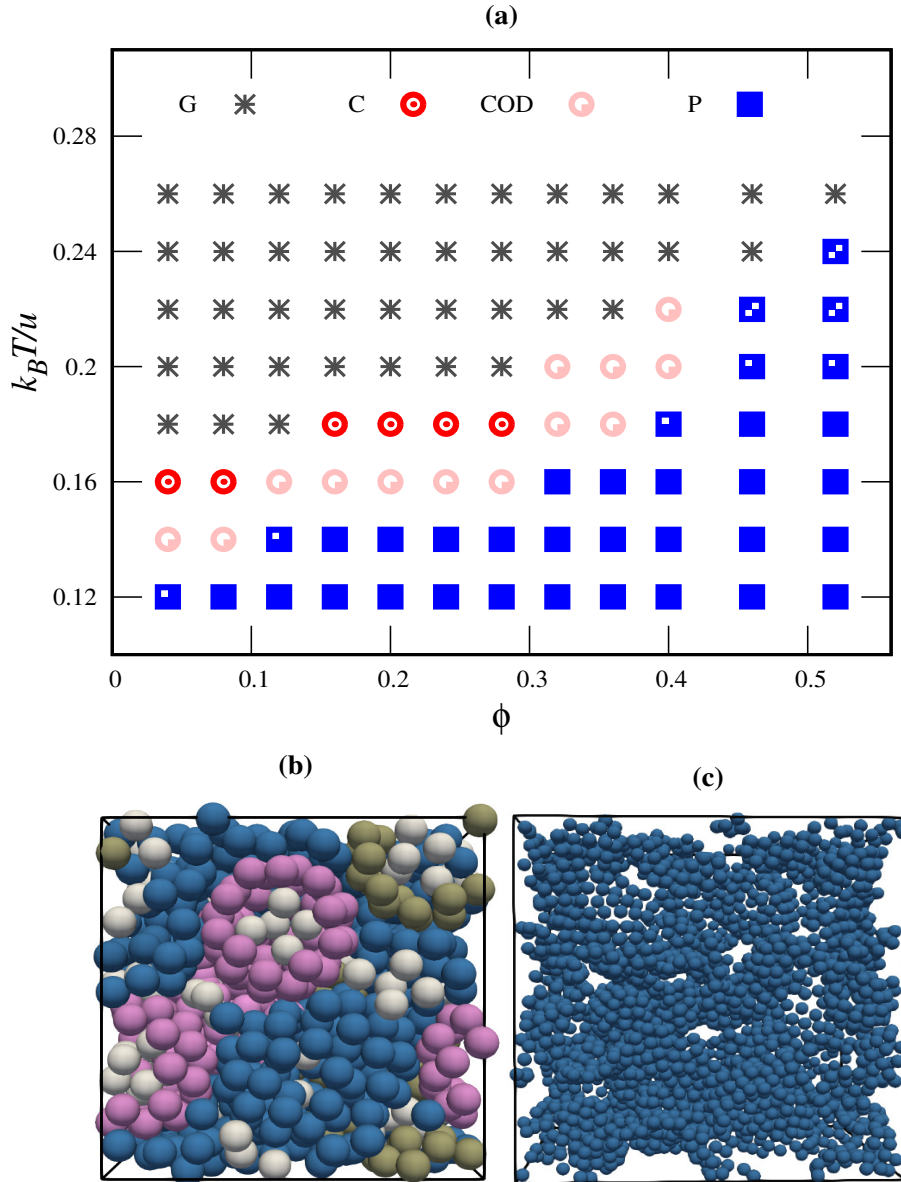


FIGURE 7.2: (a) Different region identified in the $k_BT/u_o - \phi$ plane, obtained in NVT ensemble for spherical ($p = 1$) shaped subunits with patch angle $\Omega^\circ = 74$, width $\Delta\omega^\circ = 4.5$ and range $\epsilon = 0.25$. Here **G** (black lower triangle) represents the region having disordered clusters ranging from small (monomers, dimers, etc) to large size clusters. **C** (red circle) represents the region having closed shells coexisting with the small-size clusters (monomers, dimers, trimers). **COD** (pink square) region is dominated by the presence of open shells along with closed shells and disordered clusters. **P** (blue square) region represents percolated clusters. (b) Snapshot for the system at $\phi = 0.4$ and $k_BT/u = 0.18$ (cyan pentagons), where the pink cluster represents a close shell connected through periodic boundary conditions, blue clusters are percolated partially grown shells, green clusters is partially grown shell which is not part of the percolated cluster, and white clusters are the disordered clusters, which are either freely diffusing or trapped inside the shell. (c) A percolated structure of partially grown shells is shown at $\phi = 0.08$ and $k_BT/u = 0.12$.

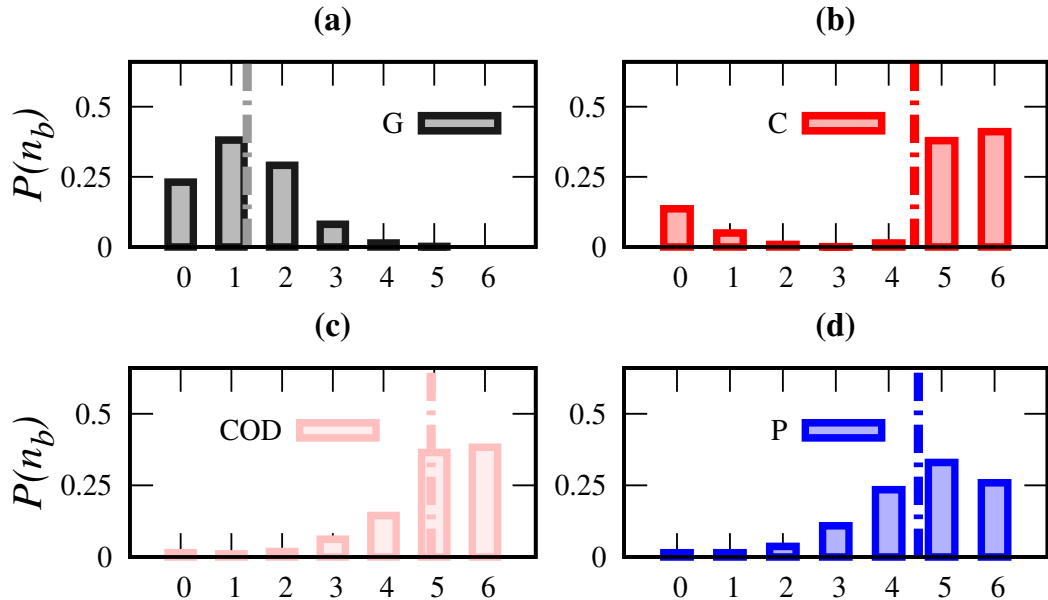


FIGURE 7.3: Probability of distribution of bonds of a subunit $P(n_b)$ and the dashed dotted line are the average bonded neighbors per particles $<n_b>$ are shown for the regions (a) **G** at $k_B T/u = 0.24$, $\phi = 0.4$ with $<n_b> = 1.2$, (b) **C** at $k_B T/u = 0.16$, $\phi = 0.08$ with $<n_b> = 4.7$, (c) **COD** at $k_B T/u = 0.14$, $\phi = 0.08$ with $<n_b> = 4.8$, (d) **P** at $k_B T/u = 0.12$, $\phi = 0.08$ with $<n_b> = 4.7$.

closed shell) and the center of curvature of the curved cluster r_{cc} . If the difference between $|r_{cm} - r_{cc}|/d$ reaches a steady state, we identify the cluster as a closed shell.

In Fig. 7.2(a) for high temperature $k_B T/u_o \leq 0.2$ and low concentration regime $\phi \leq 0.3$, the system is dominantly occupied by the monomers and small size disordered clusters mostly consist of dimers and trimers represented by **G** in the figure. 7.2(a). For $\phi \leq 0.08$ when the temperature is 0.16, along with disordered clusters, we observe the formation of one or two closed structures, which is identified as **C** region in Fig. 7.2(a). When we further reduce the temperature to 0.14, the lifetime of the bond increases and the system tries to form multiple closed structures leading to partially closed structures along with disordered clusters shown as the region **COD**. For $\phi > 0.3$, we have not observed the **C** region. At a low temperature < 0.2 and $\phi \sim 0.4$, we observe disordered percolated clusters **P**, (clusters which extend to the

size of the simulation box [238]) co-existing along with the comparatively smaller disordered clusters. Fig.7.2(b) shows the snapshot of the system at $\phi = 0.4$ at $k_B T/u = 0.18$, where we observe a percolated network (blue spheres), along with closed (pink spheres), partially closed structures (green spheres) and small disordered clusters (grey spheres). For very low volume fraction $\phi = 0.08$ in the **P** we observe only the percolated network along with a very few monomers in the system as shown in the snapshot of the system in Fig.7.2(c).

In figure. 7.3 we have shown $P(n_b)$ the probability distribution of n_b number of bonds of a subunit as obtained from the different regions in the phase space. Figure. 7.3(a) is at $\phi = 0.4$ and $k_B T/u_o = 0.24$ where we observe only disordered clusters, a majority of which are either monomer (0 bond), dimers (1 bond) or trimers (2 bonds) having the average number of bonds $\langle n_b \rangle = 1.2$ representing the **G** region. In the **C** region, we observe that monomers and clusters have 5 and 6 bonds, indicating the formation of completely closed structures. See figure. 7.3(b). Once the nucleated shells are closed, they act as large gaseous particles, interacting only through hardcore regions and coexisting with smaller clusters. In figure. 7.3 (c) the monomer has been exhausted as subunits are part of a cluster, with each having 3 or more bonds. The higher nucleation rate leads to the growth of a large number of shells. Most of the shells remain partially closed as the number of subunits required to form a closed shell becomes greater than N . Similar behavior is observed experimentally for a system of virus capsids, where due to the high nucleation rates, the structure remains partially closed [234]. On further reducing the temperature $k_B T/u_o = 0.08$ and $\phi = 0.08$ (Fig 7.3), we observe percolated structures, which will be a combination of partially closed structures connected to form on system spanning clusters (the **P** region).

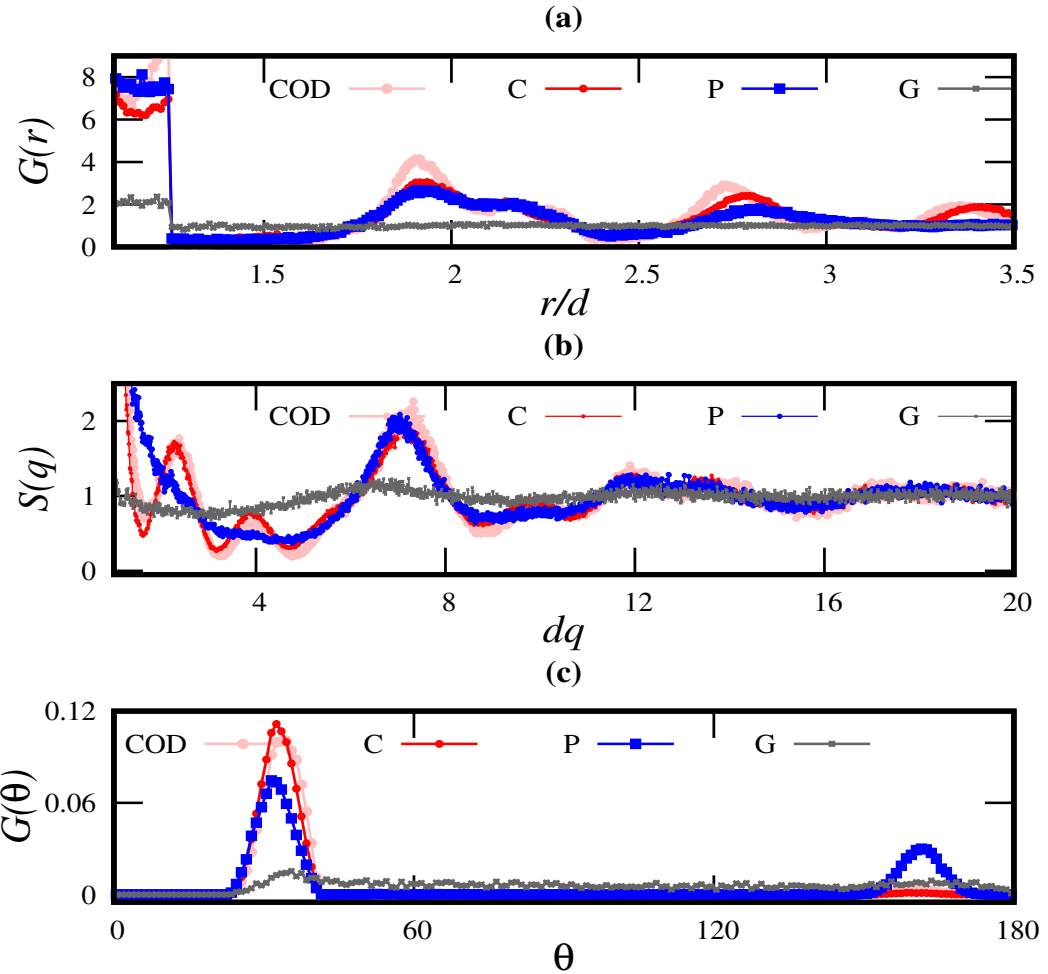


FIGURE 7.4: (a) Radial distribution function $G(r)$ is shown for 4 regions identified in figure. 7.2 where **G** at $k_B T/u = 0.24$, $\phi = 0.4$, **C** at $k_B T/u = 0.16$, $\phi = 0.08$, **COD** at $k_B T/u = 0.16$, $\phi = 0.28$, **P** at $k_B T/u = 0.08$, $\phi = 0.12$) for $\Omega^\circ = 74^\circ$, $\Delta\omega^\circ = 4.5$, $\epsilon = 0.25$ and $p = 1.0$ (spherical hardcore(b) The Structure factor $S(qd)$ is plotted as a function of qd , where q is the wave vector and (c) the angular distribution of bonded neighbor is shown corresponding to the above-mentioned regions.

In Fig. 7.4, we have shown the structural properties calculated for the system corresponding to all the regions categorized in the $T - \phi$ plane of Fig. 7.2(a). The first peak of $G(r)$ in Fig. 7.4(a), is close to $r = d + \epsilon = 1.25$, shows that the number of bonded neighbors is highest for the system in **COD** and **C** region [239], followed by **P** region. We can observe that for the **C** and **COD** region, the local ordering is almost the same as the closed-shell structures are formed. For the **P** region, we

observe that beyond $r/d > 3$ the system behaves liquid-like since the subunits are no longer showing long-range order. The long-range order for the **C** and **COD** region can be observed in the structure factor $S(qd)$ shown in the figure. 7.4(b). For the **P** region, the $S(qd)$ agrees with **C** and **COD** region for $qd > 6$, while for smaller qd behaves very similar to an irreversible DLCA percolated system [154]. In the case of **C** and **COD** region, we can observe oscillations in $S(qd)$ similar to the Fourier transform of a sphere of radius $R_s \sim 1.8$, which is the radius of the closed shell which is formed. For the **G** region, as expected from the $S(qd)$ calculation, we do not observe any long-range order. To understand the orientation of the patch, which plays an important role in deciding the structure of the closed shell, we plotted the distribution of $G(\theta)$ (Fig. 7.4(c)) [157] where θ is the angle made by the patch vector of the subunit with respect to the bonded neighbors patch vector. In the **C** and **COD** region, we have all the patch vectors of the particles aligned in the same direction as we observe only one peak as expected for a closed structure. For the **P** region, we have a peak that agrees with the **C** region and also a peak close to the $\theta = 180^\circ$. This indicates particles are aligned in opposite orientations of each other, thus making the percolated cluster disordered. For the **G** region, we observe the orientation as being uniform over almost all the θ values.

7.3.2 Kinetics of the shell growth

In order to study the shell growth, we have calculated the quantity $|r_{cm} - r_{cc}|$ as a function of time using BCD simulation technique for an individual spherical shell in Fig.7.5(a) and Fig.7.5(b)), having number of particles 166, $\epsilon = 0.4$ and 167, $\epsilon = 0.2$, respectively. Even though both the shells shown are formed for different ϵ , their $\Omega^\circ = 82^\circ$ and thus r_{cc}/b_l of the close shell are the same. Here, we observe that $|r_{cm} - r_{cc}|$ goes down with increasing time because the cluster formed is closing

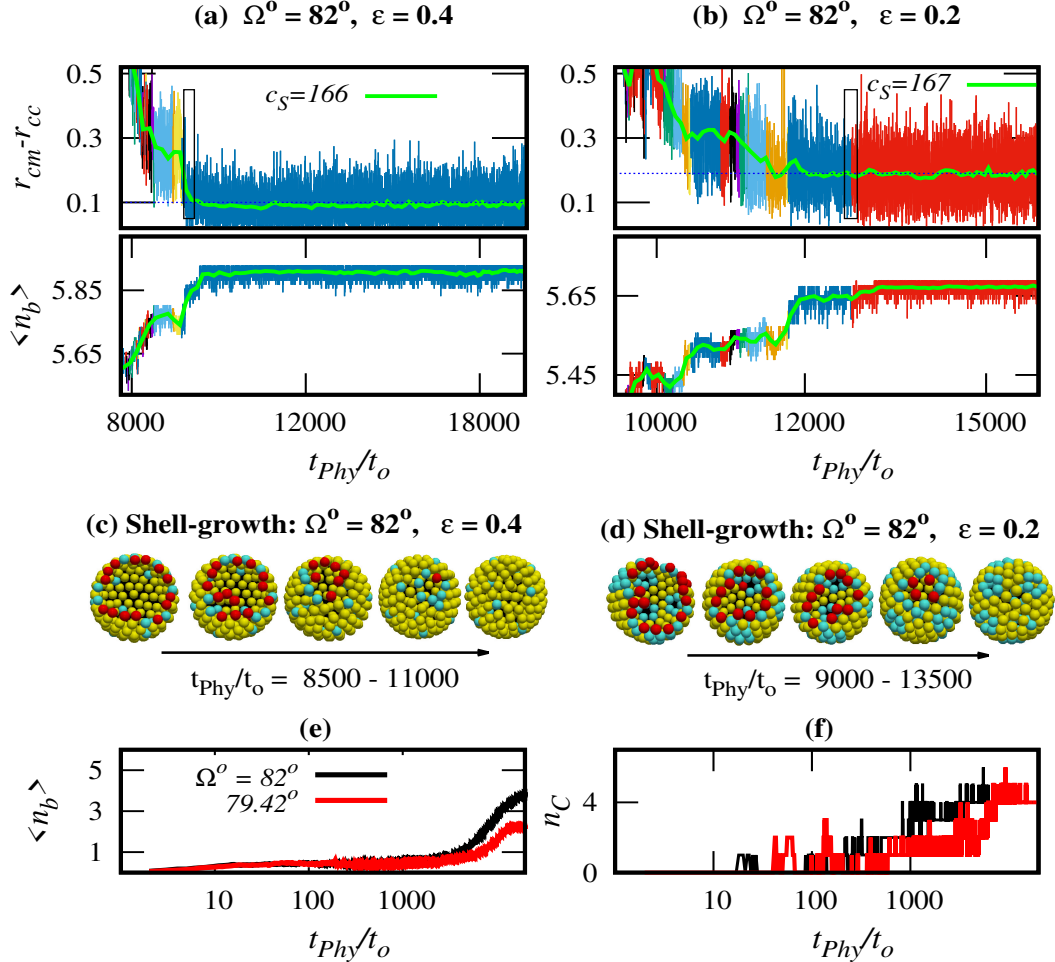


FIGURE 7.5: (a) The growth kinetics of a single shell is studied by measuring the difference of the center of curvature and center of mass of a cluster as a function of time at $c_S = 166$, for $\Delta\omega^\circ = 4.5^\circ$, $\Omega^\circ = 82^\circ$ and $\epsilon = 0.4$. The average $\langle |r_{cm} - r_{cc}| \rangle$ is shown as a solid line. The solid line reaches a steady state value corresponding to the closure of the spherical shell, as the radius of the center of mass and the center of curvature almost becomes the same. The fluctuation represented with different colors corresponds to the addition of subunits to the cluster through diffusion. Below, we show the corresponding change in the number of bond neighbors Z_S per subunit for the cluster, which also reaches a steady state value when the shell closes. (b) Similar observation is shown for the cluster with number of subunits $c_S = 167$ obtained for the system with smaller b_l having $\Delta\omega^\circ = 4.5^\circ$, $\Omega^\circ = 82^\circ$ and $\epsilon = 0.2$ leading to the closing of the shell at higher $\langle |r_{cm} - r_{cc}| \rangle$. (c) The snapshot of shell growth is shown for $\Omega^\circ = 82^\circ$, $\epsilon = 0.4$ with $c_S = 166$. (d) Snapshot of closed shell evolution of $\Omega^\circ = 82^\circ$, $\epsilon = 0.4$ with $c_S = 167$. The red spheres are subunits with the number of bonded neighbors < 5 . The cyan and yellow spheres represent subunits with 5 and 6 bonded neighbors, respectively. (e) Z the average number of bonded neighbors in the complete system is shown as a function of time t_{phys}/t_0 at $\Delta\omega^\circ = 4.5^\circ$ and $\epsilon = 0.2$ for different Ω° as indicated in the figure. The kinetics of aggregation show similarities to nucleation and growth-like phenomena. (f) The number of clusters having at least one subunit with 5 bonds n_C is shown with respect to time, which also grows along with Z .

in to form a spherical shell. Thereby, it reaches a steady state value $< 10^{-3}$, at which point we consider a closed shell is formed in the system. The reason for the fluctuation shown in Fig. 7.5(a) and Fig. 7.5(b) is due to bond rearrangements as well as the addition of new particles to the curved cluster. In Fig.7.5(a) and fig. 7.5(b) the different colors in the fluctuation of $|r_{cm} - r_{cc}|$ indicate the addition of a new subunit through diffusion. We can also observe that without the addition of a new subunit $\langle |r_{cm} - r_{cc}| \rangle$ (shown in the rectangular box) decreases, which is due to the rearrangement of the subunits by forming new bonds. The rearrangements of bonds can be observed by an increasing n_b , which is the average number of bonded neighbors for a subunit. The subunit, which is part of the new bond formation, is shown as red subunits in Fig.7.5(c) and Fig.7.5(d). For the same number of subunits, we can observe that the final structure has pentamers (cyan) distributed over the sphere with hexamers (yellow) close by, while in Fig.7.5(d), we observe pentamers forming subunits arranged together. When the spherical shell forms a closed structure, the fluctuation in $\langle |\mathbf{r}_{cm} - \mathbf{r}_{cc}| \rangle$ is only due to the diffusion of the subunits within the bonds. As soon as the average n_b reaches a steady state, $|\mathbf{r}_{cm} - \mathbf{r}_{cc}|$ also reaches a steady state as the spherical shell has closed. After the closed structure is formed, the subunit with 5 and 6 number of bonds continues to be transient, but the relative position of the subunit does not change, or there is no structural rearrangement in the course of the simulation as shown in Supplementary materials I.

The average number of bonded neighbors n_b , including all the clusters, shows that for the time < 2000 , the aggregation kinetics is the same for different Ω° as shown in Fig.7.5(e). For $\Omega^\circ = 82^\circ$ the number of subunits having 6 bonded neighbors increases faster than $\Omega^\circ = 79^\circ$ as the volume over which the patchy subunits can form bonds also increases. Also, note that $\Omega^\circ = 82^\circ$ forms a bigger closed structure

than 79° . This effect is also observed in Fig. 7.5(e) as a function of time, where we have plotted n_C , which is defined as the number of clusters with at least one subunit having 5 bonded neighbor. When the number of n_c is approximately 4, we observe a sudden proliferation in the number of clusters trying to form a closed structure, which is similar to nucleation and growth kind of phenomena. These phenomena can be observed in the supplementary materials II.

7.3.3 Size, Symmetry, and yield of the closed structures

The local structure over the surface of the shell was quantified using the radial distribution function $G(r)$. In Fig. 7.6(a), $G(r)$ is averaged over the center of mass of the subunits, which are only part of the shells and have the same number of c_S . Apart from the neighboring peak formed due to bonds formed with the neighbors, the surface of the shell is liquid-like or disordered. In fig. 7.6(b), we have plotted the orientational correlation function $g(\theta)$ [100, 236], where θ is the angle between the unit vector associated with the patch of only the bonded neighbors. We observe that as the number of subunits increases $\theta \rightarrow 0$, thus forming a nearly parallel arrangement of the patch vectors. As the number of subunits associated with a shell increases with the same ϵ , the diameter of the shell also increases. We also quantified the number of bonds associated with a subunit in 7.6(c) once the closed shell-like structure was formed. We observe that the majority of the subunits either have 5 (shown by cyan color in Fig. 7.1) or 6 (shown by yellow color in Fig. 7.1) bonded neighbors, which on average corresponds to pentagon and hexagon arrangements of the neighbors. The number of pentagons in a closed shell varies from 8 – 16 in the present study. These pentagons are the reason for closed-shell formation in the system. As the number of hexagonal arrangements increases in a cluster, the diameter of the closed structure also increases. For smaller c_S , the number of

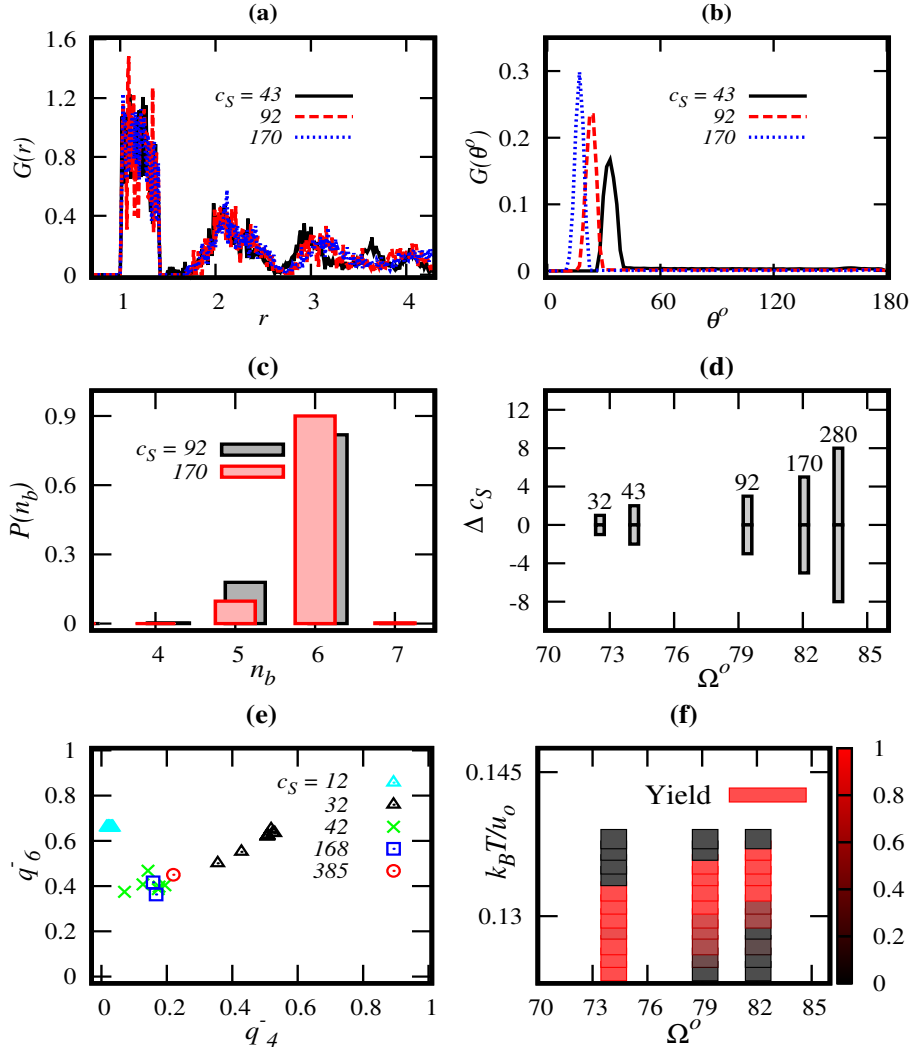


FIGURE 7.6: (a) Radial distribution function $G(r)$ calculated over a closed shell, shown for $\Omega^\circ = 74.12^\circ$ (black), 79.6° (red), 82° (blue) having the same $\Delta\omega^\circ = 3^\circ$ and $\epsilon = 0.4$, corresponding to the different number of subunits for a closed shell as shown in the figure. (b) $G(\theta^\circ)$ the angular distribution of the bonded neighbors for a closed shell with different numbers of subunits as indicated. (c) The distribution of bonded neighbors $P(n_b)$ is calculated over only the subunits that are part of the shell. (d) Subunit number variation in a cluster $\Delta c_s = |c_s - \bar{c}_s|$ for different Ω° values, where the average number of subunits in a cluster c_s is shown in the figure. (e) Steinhardt order parameter is shown for the shell with the different number of subunits as indicated in the figure. (f) Variation in the yield (color coded) of perfectly closed shell, at different $k_B T/u_0$ for varying Ω° is shown at $\phi = 0.06$, $\epsilon = 0.1$ and $\Delta\omega^\circ = 3^\circ$.

hexagons reduces and finally will have only pentagons (fig. 7.6(b)). For 12 subunits, the system self-assembles to form perfect icosahedral symmetry. We know that the structure formed with icosahedral symmetry has a degenerate number of subunits having exactly 12 number of pentagons if the structure is closed. In the present study, we calculated $\Delta c_S = c_S - \bar{c}_S$, where \bar{c}_S is the average number of subunits that are part of the closed structure, and we observe that the number of subunits in a closed structure does not follow icosahedral symmetry as shown in the fig. 7.6(d). Thus, for $\bar{c}_S = 32$ we have $\Delta c_S = \pm 1$ and for $\bar{c}_S = 280$ we have $\Delta c_S = \pm 8$.

Although the $G(r)$ shows that the closed structure has a near liquid-like structure (see Fig.7.6(a)), the bond order orientation parameter shows local order. We calculated Steinhardt bond order orientation parameter \bar{q}_n as defined by Mosayebi et al. [215], which is given by

$$q_n = \left[\frac{4\pi}{2n+1} \sum_{m=-n}^n |\bar{q}_{nm}|^2 \right]^{\frac{1}{2}} \quad (7.4)$$

$$\bar{q}_{nm} = \langle Y_{nm}(\theta(\vec{r}), \phi(\vec{r})) \rangle \quad (7.5)$$

where $Y_{lm}(\theta, \phi)$ are spherical harmonics, and $\theta(\vec{r})$ and $\phi(\vec{r})$ are the polar and azimuthal angles respectively, with respect to the center of the cage.[240]. When the maximum number of subunits being part of the closed shell was 12, we obtained the icosahedral symmetry irrespective of the aspect ratio of the subunit or the number of clusters n_C formed in the simulation box. If the closed shell shows icosahedral symmetry, then it can have only a specific number of subunits like 12, 32, 42, etc. Also, the number of subunits having only 5 neighbors (pentagon) in the system will be 12, followed by particles having 6 neighbors (hexagon). In our system, we observe that the number of subunits forming a closed shell does not degenerate to have an icosahedral symmetric closed shell. The number of particles and the local symmetry

of the system keep on changing, as shown in Fig. 7.6(e). We have shown q_6 as a function of q_4 for a closed shell containing a different number of subunits. Except for the number of subunits, 12, none of the close shells show icosahedral symmetry. The number of pentagons (5 bonded neighbors) in all the closed structures we obtained varies between 8 and 16, and it remains constant after the closed structure is formed. Also, once the closed shell is formed, we have observed transformation from a 5 to 6 bonded neighbors and vice versa in the duration of our simulation. It has already been shown that when perturbations like the flexibility of the bond are introduced to a perfect icosahedral symmetric closed structure, the symmetry is no longer required for the closed structure to be stable [215]. This is very similar to the present system as the structure is formed from a random self-assembly process, and the structure has flexible bonds as well, depending on ϵ .

Yield is defined as the number of closed shells with respect to n_C . Thus, when there is only one spherical shell and the rest of the subunits are monomers, the yield will be unity. Fig. 7.6(f) shows the yield of the closed shell at different temperatures, calculated at $\phi = 0.06$ for different values of Ω° . We observe that when the $\Omega^\circ = 74^\circ$, the yield is zero for $k_B T/u_o > 0.134$, because the clusters formed are smaller and entropy contribution dominates, thereby not allowing closed shells. As we reduce $k_B T/u_o$, they do form many small closed structures. When we increase Ω° the volume of the annular patch over which the subunit can form a bond increases, and thus, at higher $k_B T/u_o$ as well, the system forms many closed structures with the same radius. On reducing $k_B T/u_o$, we observe that enthalpic contribution dominates and many curved clusters are formed, which are not able to aggregate into a closed shell as expected. As we further increase, Ω° , the region of high yield also reduces and also shifts towards higher $k_B T/u_o$. At $\Omega^\circ = 90^\circ$, we will never obtain a closed structure, as the patchy particle will prefer a flat surface instead of a curved surface.

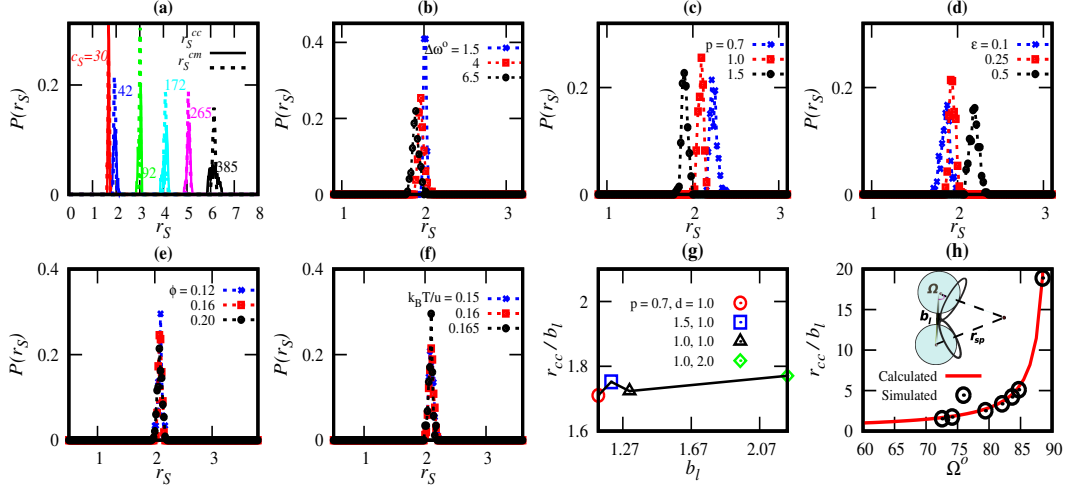


FIGURE 7.7: (a) $P(r_S)$ is shown for different cluster sizes (obtained by different Ω° value, while keeping the rest of the potential parameters as the same), measured from the center of mass (dotted line) and center of curvature of the shell (solid line). The position of the peak represents the radius of the shell, and the width shows the deviation from the spherical shape. (b) $P(r_S)$ is shown for different $\Delta\omega^\circ$ (calculated at $\Omega^\circ = 74^\circ$ and $\epsilon = 0.25$) values, showing the effect of patch width over the size and shape of the shell. (c) $P(r_S)$ is shown for different hard-core shapes as indicated in the figure, calculated for $\Omega^\circ = 74^\circ$, $\epsilon = 0.25$ and $\Delta\omega^\circ = 3^\circ$. (d) The effect of patch range is shown for different ϵ as shown in the figure at $\Omega^\circ = 74^\circ$ and $\Delta\omega^\circ = 4.5^\circ$. (e) $P(r_S)$ is shown for the system at different ϕ (as indicated in the figure) while keeping all the other parameters the same. (f) The effect of temperature over $P(r_S)$ is shown for the shells obtained by using the same parameters. (g) The ratio r_{cc}/b_l where b_l is the distance of the center of mass of a neighboring subunit for different aspect ratios and diameter of the subunit as indicated in the figure for $\Omega^\circ = 74^\circ$. The solid line is a guide to the eye (h) Effect of Ω° over r_{sp}/b_l , showing the latter dominantly controlled by Ω° . The solid line is given by $\frac{1}{2 \cos \Omega^\circ}$.

The radius of the self-assembled closed shell was quantified by calculating the radius from the center of mass and the center of curvature of the curved cluster. Fig. 7.7(a) shows the distribution $P(r_S)$, which is the probability of occurrence of a near-spherical shell with a particular radius r_S , having c_s subunits. The solid lines represent the radius distribution of the spherical shell as calculated from the center of mass calculation, and the dotted line is the radius from the center of curvature calculation. As the number of subunits in the spherical shell increases, the radius of the shell also increases. When the angular width of the patch $\Delta\omega^\circ$ increases, the

radius of the spherical shell decreases for the same temperature because the subunit can diffuse more freely within the bond, thus forming a compact structure as shown in Fig. 7.7(b). The radius of the spherical shell increases with the decrease in the aspect ratio, as the excluded volume close to the annular patches increases when the aspect ratio decreases, such that an oblate spheroid will form a closed shell with a larger radius.

Increasing the interaction range ϵ leads to a larger shell, as shown in Fig. 7.7(d). But it becomes more fluid-like, and larger pores can be observed between subunits as they can diffuse within the bonds easily for higher ϵ . An interesting fact remains that the radius of the shell is independent of the volume fraction, as shown in Fig. 7.7(e). As we increase the volume fraction, the number of shells formed increases while the radius remains constant, and also, a few curved clusters will not be able to form closed structures, see Fig. 7.1(f). The same effect is also observed when we change temperature (see Fig. 7.7(f)). By tuning Ω° , we can control the radius of the shell to any desired radius. In Fig. 7.7(g), we have shown that irrespective of the aspect ratio of the particle, the ratio r_s/b_l remains almost constant for the same $\Omega^\circ = 74$, where b_l is the center of the mass distance between the nearest subunit, deduced from the calculation of $G(r)$ of the closed structure irrespective of the aspect ratio of the subunit. The reason is that the radius of the shell is given by $\frac{r_s}{b_l} \approx \frac{1}{2 \cos \Omega^\circ}$, as can be deduced from the inset of Fig. 7.7(h) where we have assumed the subunits are connected together through the annular patches. The value of b_l is obtained from the simulation, and it will always remain between $1 < b_l < 1 + \epsilon$. When we plot the radius of curvature of the cluster obtained from the simulation as a function of Ω° we observe that it follows the simple relation $1/2 \cos \Omega^\circ$ as shown by the solid line in Fig. 7.7(h), only when $\Omega^\circ < 90^\circ$ the system will form closed structures.

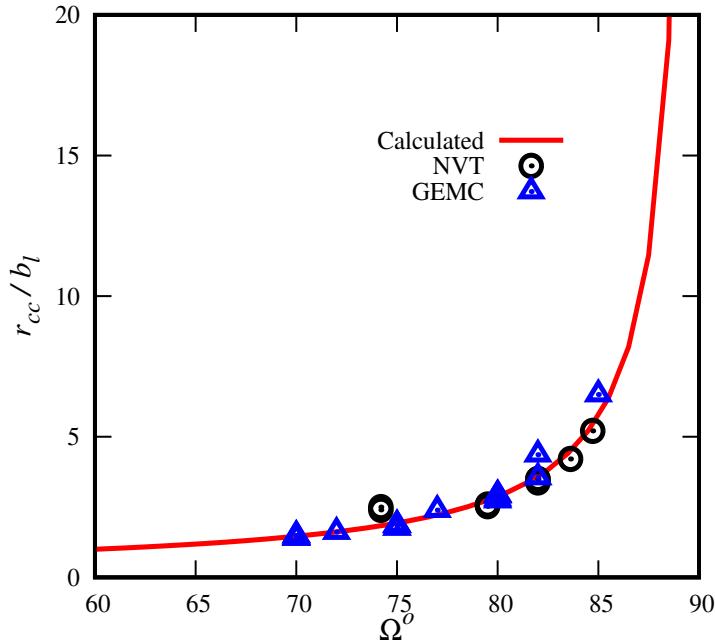


FIGURE 7.8: The size of the shells predicted by *GEMC* (blue triangles) and compared with the same obtained by using *NVT*(black circles). Where the solid line shows the simple relation $1/2 \cos \Omega^\circ$ between the patch angle of ω and the size of the shell.

The closed shells have been found to be monodisperse in terms of the radius. However, the annular patches used in the system have finite width $\Delta\omega$, which gives some degree of flexibility within the bond with directional constraints. To predict the equilibrium radius of the closed structures, we cannot use methods like variable shape simulation[241, 91], as it requires a translational degree of freedom for the subunits. The other way is to use the *NPT* ensemble on the surface of the sphere [242], but it requires prior knowledge of the exact number of particles required to close the shell. One another method can be a μPT ensemble performed over the surface of the sphere, where confinement and a fixed number of particles can ensure the convergence of the system. In this method, there is a finite probability that before reaching the minimum energy configuration, the size of the system in the fluid phase would start diverging to maintain constant μ and P . Thus, making μPT ensemble is not a good method [109] for the present work. To predict the possible

structure, we have used the Gibbs ensemble (GEMC)[243] method on the surface of the sphere. The proposed method does not account for the fluctuation and deviation of the shape away from the sphericity.

To predict the possible structure, we used the Gibbs ensemble Monte Carlo (GEMC) [243] on the surface of the sphere. This method does not account for the fluctuation or deviation in the shape away from the sphericity. In this method, we take two spheres of the same radius and randomly distribute the subunit over the surface of the sphere, which are randomly moved and rotated on the surface of a sphere. This is followed by an attempt to change the surface area of the sphere such that the total surface area of both spheres together remains constant. Each of these steps is accepted by a probability, as given in the later section. When an equilibrium is reached, one sphere will give us the radius as well as the number of subunits of the closed shell at a particular temperature. While the other sphere will contain disordered clusters on the surface as shown in Fig 7.9. We performed Gibbs ensemble simulation over the surface of a sphere for a number of configurations by changing the temperature. We found that the method predicts the r_{cc}/b_l vs Ω° relation as the same (shown as blue triangular points in Fig.7.8) as it has been obtained in the *NVT* simulation(shown as a blue triangular point in Fig.7.8). Here, we observe that even in the GEMC simulation, the size of the cluster is favored, which corresponds to the relation $r_s/b_l = \frac{1}{2\cos\Omega^\circ}$. Although going for the higher value of the Ω° , we observe deviation from the red line (Fig.7.8). It happens due to the finite width of the annular patch ($\Delta\omega = 4.5$). As we increase Ω° , the size of the shell becomes very sensitive with Ω° and diverges close to $\Omega^\circ = 90$.

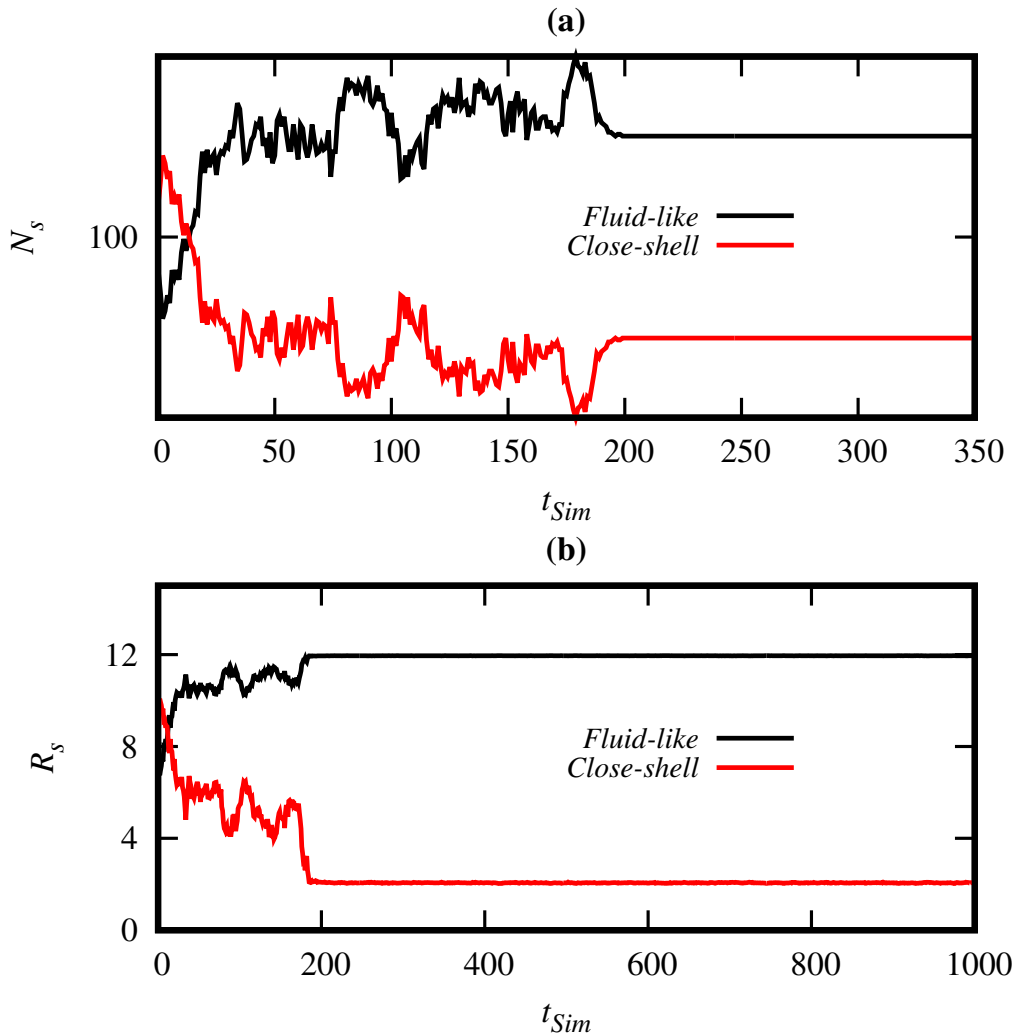


FIGURE 7.9: (a) Variation in N_s and (b) variation in R_s is shown, where red line represents *Sphere1* and black line represents *Sphere2* of a particular ensemble. System is kept at $\phi_A = 0.1$, $k_B T/u = 0.14$ having patch properties $\Omega^\circ = 74^\circ$, $\Delta\omega^\circ = 4.5$, $\epsilon = 0.25$ and $p = 1.0$.

7.4 GEMC Simulation in a closed system

To perform the *GEMC* simulation on the surface of the sphere, we took two spheres of surface area A_1 and A_2 . Then the N number subunits are randomly distributed on the surface of the spheres with area fraction defined by $\phi_A = 4\pi R_s^2$, where R_s is the radius of the spheres. $2N$ particles are randomly chosen such that each particle will undergo one translational movement and one rotational in each simulation step.

The subunit moves on the surface of the sphere in the translational step. In the rotational step, the patch vector of the subunit undergoes a rotation in the random direction. Following the subunit movement, the surface area of the sphere is changed randomly in small steps, such that the total area of the two spheres $A_t = A_1 + A_2$ remains constant throughout the simulation. After changing the area, the position of the particles is re-scaled with the factor R'_s/R_S , where R'_s is the radius of the sphere after the change in the area. The change in radius is accepted according to the Gibbs ensemble criteria [244], given as,

$$\begin{aligned} & \text{acceptance}(A_1 + A_2 \rightarrow A'_1 + A'_2) \\ &= \min [\exp [-\beta(\Delta E)], 1] \end{aligned} \quad (7.6)$$

Such that,

$$\Delta E = \Delta U_1 + \Delta U_2 - N_1 \ln \frac{A'_1}{A_1} - N_2 \ln \frac{A'_2}{A_2} \quad (7.7)$$

Where $\Delta U_1, \Delta U_2$ are the changes in energy of the first and second spheres. Following the volume change movement, we also swap subunits from one spherical surface to the other, such that the total number of the subunit on both spheres together remains constant and equal to N . A subunit is randomly chosen and deleted from one sphere and inserted in another one by assigning a random orientation of the patch vector and at a position randomly chosen over the surface of the sphere on which the subunit is being placed. The change in energy in both the spheres is calculated $(\Delta U_3 + \Delta U_4)$ where the criteria for the acceptance of swapping the particle [244] is given as,

$$\begin{aligned}
& \text{acceptance}(1 \rightarrow 2) \\
&= \min [\exp [-\beta(\Delta E)], 1]
\end{aligned} \tag{7.8}$$

Such that,

$$\Delta E = \Delta U_3 + \Delta U_4 + \ln \frac{A_1.N_2 + 1}{A_2.N_1} \tag{7.9}$$

Note that it is better to start with the number of subunits that is not more than about 5 times the number obtained from the NVT ensemble for a closed shell at the right temperature for faster convergence. To show the convergence, we start the system with $N_1 + N_2 = 200$, at $\phi_A = 0.1$. The system with sphere size close to the final configuration ($N_1 + N_2 = 200$) converges to $N_s \sim 48$ see figure. 7.9(a) and $R_s \sim 1.8$ see figure. 7.9(b) as obtained from the NVT simulation. The second sphere has a higher R_s and N_s , which represents fluid-like behavior with sparsely distributed clusters on the sphere.

7.5 Discussion and Conclusion

Making annular patches is possible through experiments, as patchy interactions have been created by grafting polymers onto complicated asymmetric building blocks at desired locations [245]. Most of the closed structures generated experimentally have been created by tweaking the interaction between protein molecules [246] or virus subunits[247], which restrict the radius of the cages formed. One of the challenges that need to be addressed is the maximum size over which these structures can be formed. In the present model of annular patches, the size constraint challenge is addressed. In addition, the model also creates monodisperse closed shells in terms

of the radius for low concentration. For intermediate concentration, nanocontainers-like structures emerge. These structures will find application in vaccine production, acting as nanoreactors, drug delivery systems, etc. By restricting the number of bonds formed per patch, it is possible to engineer different morphology for clusters formed, including the closed structures of different geometry through the self-assembly route. This simple potential proposed in the present work may also provide insight into understanding more complex structures like the virus.

Chapter 8

Conclusion and future scope

8.1 Conclusions

We simulated different systems of shape anisotropic particles and studied the dynamics and self-assembly by using the approach of BCD. For the purpose of dynamics, we have extensively studied hard-core particles in both the bulk system and the system under the influence of obstacles and confinement. In bulk, we studied the one-component and a two-component system of sphere-prolate and sphere-oblate hard cores. The nematic-isotropic phase was studied in the binary system. Following the study on the dynamics of the system of hardcore, we studied the kinetics, structure, and phases of the system with shape anisotropic attractive square-well potential. We incorporated patches on the elongated particles, which introduced directional interactions. Additionally, we explored the use of annular patches in studying closed systems, which allowed us to gain insights into the behavior and properties of the system under these specific conditions. From the presented work these conclusions can be drawn-

- At high concentrations, the diffusivity of spheroidal colloids is greater than the diffusivity of spheres. While at low concentrations we observed the opposite effect. It happens due to friction dominating at low concentrations and the packing effect at high concentrations.
- Isotropic-nematic phase transition occurs at high concentration in the two-component system of isotropic and anisotropic particles compared to the one-component system.
- Rotational diffusivity of spheroids depends upon the location of isotropic-nematic phase lines, where close to the phase line it freezes. With the introduction of isotropic particles, the rotational diffusivity of anisotropic particles is enhanced.
- At low concentrations, the diffusivity of the spheroids is enhanced in the presence of spherical particles.
- Introducing shape anisotropy in terms of hardcore leads to the highly monodispersed crystal system. For example, when prolate hard-core particles are superimposed with patches, the resulting system exhibits a remarkable property. Where by simply changing the thermodynamic parameters such as temperature and pressure, we can achieve both two-dimensional (2D) and three-dimensional (3D) structures. This ability to manipulate the system's structure through parameter adjustments offers exciting possibilities for controlling the material's properties and behavior.
- We have observed the formation of monolayer kinetically favored over all the other structures.
- Introduction of annular patches, independent of the shape of the hard-core leads to the formation of spherically closed shells.

- Yield of the close shells is dependent upon the temperature and pressure of the system. Where the structural rearrangement happening over the surface of the closed shell at the local level plays an important role which helps to close the shell even at a very high radius in comparison to the size of the building blocks.

8.2 Future scope

Simulations have been a great tool, for the study of the complex system. It serves parallel to the theoretical and experimental approach to studying nature and finding its application for the welfare of the human being. It not only provides a pathway to the new findings and shows the new possibilities but also creates a challenge for the experiments to invent, study, and explain the new findings.

This quest for knowledge can lead us to the exploration in various areas, such as:

- Crystallization in the presence of cylindrical obstacles.
- Dynamics in the random arrangement of obstacles.
- Stability analysis of semi-closed and closed systems.
- Equations of state for binary mixtures.
- Self-assembly and aggregation in irreversible systems of shape-anisotropic particles.
- Fluid-fluid coexistence with short-range and highly directional bonding.
- Study of the dynamics of over-damped active-driven systems, like kinesin motors.

The presented work offers a pathway for studying colloids from multiple perspectives, including thermodynamics, dynamics, and equilibrium properties. Moreover, it finds applications in material modeling and designing effective drug delivery systems using principles of dynamics and material synthesis. Additionally, it enables the fabrication of controllable and optically active materials, investigation of neurodegenerative diseases, exploration of physical properties of viruses, and understanding their self-assembly mechanisms, among other exciting possibilities. Overall, these simulations open up new horizons and contribute significantly to scientific progress in various fields.

References

- [1] Peter H. Santschi. “Marine colloids, agents of the self-cleansing capacity of aquatic systems: Historical perspective and new discoveries”. In: *Marine Chemistry* 207 (2018), pp. 124–135. ISSN: 0304-4203. DOI: <https://doi.org/10.1016/j.marchem.2018.11.003>.
- [2] Mark L Wells and Edward D Goldberg. “Occurrence of small colloids in sea water”. In: *Nature* 353.6342 (1991), pp. 342–344.
- [3] Jin Young Kim et al. “Crack formation and prevention in colloidal drops”. In: *Scientific reports* 5.1 (2015), pp. 1–9.
- [4] F. Javier Montes Ruiz-Cabello et al. “Electric double-layer potentials and surface regulation properties measured by colloidal-probe atomic force microscopy”. In: *Phys. Rev. E* 90 (1 July 2014), p. 012301. DOI: 10.1103/PhysRevE.90.012301.
- [5] Thomas Palberg. “Colloidal crystallization dynamics”. In: *Current Opinion in Colloid Interface Science* 2.6 (1997), pp. 607–614. ISSN: 1359-0294. DOI: [https://doi.org/10.1016/S1359-0294\(97\)80053-2](https://doi.org/10.1016/S1359-0294(97)80053-2).
- [6] Stefano Sacanna and David J. Pine. “Shape-anisotropic colloids: Building blocks for complex assemblies”. In: *Current Opinion in Colloid Interface*

- Science* 16.2 (2011), pp. 96–105. ISSN: 1359-0294. DOI: <https://doi.org/10.1101/j.cocis.2011.01.003>.
- [7] Sujin Babu et al. “The influence of bond rigidity and cluster diffusion on the self-diffusion of hard spheres with square well interaction”. In: *The Journal of Chemical Physics* 128.20 (2008), p. 204504. DOI: 10.1063/1.2925686.
- [8] Clara Weis et al. “Microstructure, local dynamics, and flow behavior of colloidal suspensions with weak attractive interactions”. In: *Scientific reports* 6.1 (2016), pp. 1–15.
- [9] Gernot Schaller and Michael Meyer-Hermann. “Multicellular tumor spheroid in an off-lattice Voronoi-Delaunay cell model”. In: *Phys. Rev. E* 71 (5 May 2005), p. 051910. DOI: 10.1103/PhysRevE.71.051910.
- [10] Mandana T Manzari et al. “Targeted drug delivery strategies for precision medicines”. In: *Nature Reviews Materials* 6.4 (2021), pp. 351–370.
- [11] Hossam S. El-Sawy et al. “Stimuli-Responsive Nano-Architecture Drug-Delivery Systems to Solid Tumor Micromilieu: Past, Present, and Future Perspectives”. In: *ACS Nano* 12.11 (2018). PMID: 30335963, pp. 10636–10664. DOI: 10.1021/acsnano.8b06104.
- [12] Luhui Ning et al. “Diffusion of colloidal particles in model porous media”. In: *Phys. Rev. E* 103 (2 Feb. 2021), p. 022608. DOI: 10.1103/PhysRevE.103.022608.
- [13] F. Paiva et al. “Interfacial aggregation of Janus rods in binary polymer blends and their effect on phase separation”. In: *The Journal of Chemical Physics* 151.11 (2019), p. 114907. DOI: 10.1063/1.5100134.

- [14] Gumhye Jeon et al. “Electrically Actuated Smart Nanoporous Membrane for Pulsatile Drug Release”. In: *Nano Letters* 11.3 (2011). PMID: 21280644, pp. 1284–1288. DOI: [10.1021/nl1104329y](https://doi.org/10.1021/nl1104329y).
- [15] Rouven Stuckert, Claudia Simone Plüisch, and Alexander Wittemann. “Experimental assessment and model validation on how shape determines sedimentation and diffusion of colloidal particles”. In: *Langmuir* 34.44 (2018), pp. 13339–13351.
- [16] John Happel and Howard Brenner. *Low Reynolds number hydrodynamics: with special applications to particulate media*. Vol. 1. Springer Science & Business Media, 1983.
- [17] Peter Bereolos et al. “Transport properties of the hard ellipsoid fluid”. In: *The Journal of chemical physics* 99.8 (1993), pp. 6087–6097.
- [18] Francis Perrin. “Mouvement brownien d’un ellipsoïde-I. Dispersion diélectrique pour des molécules ellipsoidales”. In: *J. phys. radium* 5.10 (1934), pp. 497–511.
- [19] Yun Su et al. “Colloidal diffusion over a quenched two-dimensional random potential”. In: *Soft Matter* 13.27 (2017), pp. 4773–4785.
- [20] Cristiano De Michele, Rolf Schilling, and Francesco Sciortino. “Dynamics of Uniaxial Hard Ellipsoids”. In: *Phys. Rev. Lett.* 98 (26 June 2007), p. 265702. DOI: [10.1103/PhysRevLett.98.265702](https://doi.org/10.1103/PhysRevLett.98.265702).
- [21] Stefano Sacanna, David J. Pine, and Gi-Ra Yi. “Engineering shape: the novel geometries of colloidal self-assembly”. In: *Soft Matter* 9 (34 2013), pp. 8096–8106. DOI: [10.1039/C3SM50500F](https://doi.org/10.1039/C3SM50500F).

- [22] Jörg Roller et al. “Observation of liquid glass in suspensions of ellipsoidal colloids”. In: *Proceedings of the National Academy of Sciences* 118.3 (2021), e2018072118. DOI: 10.1073/pnas.2018072118. eprint: <https://www.pnas.org/doi/pdf/10.1073/pnas.2018072118>.
- [23] Richard Matthews and Christos N. Likos. “Influence of Fluctuating Membranes on Self-Assembly of Patchy Colloids”. In: *Phys. Rev. Lett.* 109 (17 Oct. 2012), p. 178302. DOI: 10.1103/PhysRevLett.109.178302.
- [24] Shenyu Yang et al. “Giant capsids from lattice self-assembly of cyclodextrin complexes”. In: *Nature communications* 8.1 (2017), p. 15856.
- [25] Lubomira Tosheva and Valentin P Valtchev. “Nanozeolites: synthesis, crystallization mechanism, and applications”. In: *Chemistry of materials* 17.10 (2005), pp. 2494–2513.
- [26] George M Whitesides and Bartosz Grzybowski. “Self-assembly at all scales”. In: *Science* 295.5564 (2002), pp. 2418–2421.
- [27] CM Sorensen. “The mobility of fractal aggregates: a review”. In: *Aerosol Science and Technology* 45.7 (2011), pp. 765–779.
- [28] Mitsuo Ataka and Michihiko Asai. “Analysis of the nucleation and crystal growth kinetics of lysozyme by a theory of self-assembly”. In: *Biophysical journal* 58.3 (1990), pp. 807–811.
- [29] Simone Ciarella, Francesco Sciortino, and Wouter G Ellenbroek. “Dynamics of vitrimers: Defects as a highway to stress relaxation”. In: *Physical review letters* 121.5 (2018), p. 058003.
- [30] Zhenli Zhang and Sharon C Glotzer. “Self-assembly of patchy particles”. In: *Nano letters* 4.8 (2004), pp. 1407–1413.

- [31] Yusei Kobayashi, Noriyoshi Arai, and Arash Nikoubashman. “Structure and dynamics of amphiphilic Janus spheres and spherocylinders under shear”. In: *Soft Matter* 16.2 (2020), pp. 476–486.
- [32] Adam J Ellery, Ruth E Baker, and Matthew J Simpson. “Calculating the Fickian diffusivity for a lattice-based random walk with agents and obstacles of different shapes and sizes”. In: *Physical biology* 12.6 (2015), p. 066010.
- [33] R. Klein. “Dynamics of Colloidal Suspensions”. In: *Structure and Dynamics of Polymer and Colloidal Systems*. Ed. by Redouane Borsali and Robert Pecora. Dordrecht: Springer Netherlands, 2002, pp. 83–115. ISBN: 978-94-010-0442-8. DOI: [10.1007/978-94-010-0442-8_4](https://doi.org/10.1007/978-94-010-0442-8_4).
- [34] Navaneeth K Marath and John S Wettlaufer. “Hydrodynamic interactions and the diffusivity of spheroidal particles”. In: *The Journal of Chemical Physics* 151.2 (2019), p. 024107.
- [35] Howard Brenner. “Coupling between the translational and rotational brownian motions of rigid particles of arbitrary shape: II. General theory”. In: *Journal of Colloid and Interface Science* 23.3 (1967), pp. 407–436. ISSN: 0021-9797. DOI: [https://doi.org/10.1016/0021-9797\(67\)90185-3](https://doi.org/10.1016/0021-9797(67)90185-3).
- [36] Felix Roosen-Runge, Peter Schurtenberger, and Anna Stradner. “Self-diffusion of nonspherical particles fundamentally conflicts with effective sphere models”. In: *Journal of Physics: Condensed Matter* 33.15 (Feb. 2021), p. 154002. DOI: [10.1088/1361-648X/abdff9](https://doi.org/10.1088/1361-648X/abdff9).
- [37] Dan S Bolintineanu et al. “Particle dynamics modeling methods for colloid suspensions”. In: *Computational Particle Mechanics* 1 (2014), pp. 321–356.
- [38] Sheng Chen, Wen Yan, and Tong Gao. “Scaling law of Brownian rotation in dense hard-rod suspensions”. In: *Phys. Rev. E* 102 (1 July 2020), p. 012608. DOI: [10.1103/PhysRevE.102.012608](https://doi.org/10.1103/PhysRevE.102.012608).

- [39] Wenxiang Xu et al. “Multiple-inclusion model for the transport properties of porous composites considering coupled effects of pores and interphase around spheroidal particles”. In: *International Journal of Mechanical Sciences* 150 (2019), pp. 610–616. ISSN: 0020-7403. DOI: <https://doi.org/10.1016/j.ijmecsci.2018.10.063>.
- [40] Y. Yin et al. “Three-dimensional pore-scale study of methane gas mass diffusion in shale with spatially heterogeneous and anisotropic features”. In: *Fuel* 273 (2020), p. 117750. ISSN: 0016-2361. DOI: <https://doi.org/10.1016/j.fuel.2020.117750>.
- [41] R. Golestanian and A. Ajdari. “Tracer diffusivity in a time- or space-dependent temperature field”. In: *Europhysics Letters* 59.6 (Sept. 2002), p. 800. DOI: [10.1209/epl/i2002-00113-x](https://doi.org/10.1209/epl/i2002-00113-x).
- [42] Alejandro Cuetos and Alessandro Patti. “Dynamics of hard colloidal cuboids in nematic liquid crystals”. In: *Phys. Rev. E* 101 (5 May 2020), p. 052702. DOI: [10.1103/PhysRevE.101.052702](https://doi.org/10.1103/PhysRevE.101.052702).
- [43] Debra J Audus et al. “Interplay of particle shape and suspension properties: a study of cube-like particles”. In: *Soft matter* 11.17 (2015), pp. 3360–3366.
- [44] Magnus Röding. “Shape-dependent effective diffusivity in packings of hard cubes and cuboids compared with spheres and ellipsoids”. In: *Soft Matter* 13 (46 2017), pp. 8864–8870. DOI: [10.1039/C7SM01910F](https://doi.org/10.1039/C7SM01910F).
- [45] Melissa Hess et al. “Scale-dependent particle diffusivity and apparent viscosity in polymer solutions as probed by dynamic magnetic nanorheology”. In: *Soft Matter* 16.32 (2020), pp. 7562–7575.

- [46] Susheel S. Bhandari, K. Muralidhar, and Yogesh M. Joshi. “Thermal Diffusivity and Viscosity of Suspensions of Disk-Shaped Nanoparticles”. In: *Industrial & Engineering Chemistry Research* 52.43 (2013), pp. 15114–15123. DOI: [10.1021/ie402508x](https://doi.org/10.1021/ie402508x).
- [47] JP Freyer and RM Sutherland. “Determination of diffusion constants for metabolites in multicell tumor spheroids”. In: *Oxygen Transport to Tissue—IV* (1983), pp. 463–475.
- [48] Deshpreny Mukhija and Michael J. Solomon. “Translational and rotational dynamics of colloidal rods by direct visualization with confocal microscopy”. In: *Journal of Colloid and Interface Science* 314.1 (2007), pp. 98–106. ISSN: 0021-9797. DOI: <https://doi.org/10.1016/j.jcis.2007.05.055>.
- [49] Mark M. Panczyk, Norman J. Wagner, and Eric M. Furst. “Short-time diffusivity of dicolloids”. In: *Phys. Rev. E* 89 (6 June 2014), p. 062311. DOI: [10.1103/PhysRevE.89.062311](https://doi.org/10.1103/PhysRevE.89.062311).
- [50] Bennett D Marshall et al. “Rotational and translational diffusivities of germanium nanowires”. In: *Rheologica Acta* 48 (2009), pp. 589–596.
- [51] Adam J Ellery, Ruth E Baker, and Matthew J Simpson. “Calculating the Fickian diffusivity for a lattice-based random walk with agents and obstacles of different shapes and sizes”. In: *Physical Biology* 12.6 (Nov. 2015), p. 066010. DOI: [10.1088/1478-3975/12/6/066010](https://doi.org/10.1088/1478-3975/12/6/066010).
- [52] Matthew J. Simpson and Michael J. Plank. “Simplified calculation of diffusivity for a lattice-based random walk with a single obstacle”. In: *Results in Physics* 7 (2017), pp. 3346–3348. ISSN: 2211-3797. DOI: <https://doi.org/10.1016/j.rinp.2017.08.063>.
- [53] Fumiaki Nakai et al. “Increase in Rod Diffusivity Emerges even in Markovian Nature”. In: *arXiv preprint arXiv:2301.02394* (2023).

- [54] Mohsen Besanjideh, Amir Shamloo, and Siamak Kazemzadeh Hannani. “Evaluating the reliability of tumour spheroid-on-chip models for replicating intra-tumoural drug delivery: considering the role of microfluidic parameters”. In: *Journal of Drug Targeting* (2022), pp. 1–15.
- [55] Song Wu, Jia-Xiang Li, and Qun-Li Lei. “Facilitated dynamics of an active polymer in 2D crowded environments with obstacles”. In: *Soft Matter* 18.48 (2022), pp. 9263–9272.
- [56] Erik Kalz et al. “Collisions Enhance Self-Diffusion in Odd-Diffusive Systems”. In: *Phys. Rev. Lett.* 129 (9 Aug. 2022), p. 090601. DOI: [10.1103/PhysRevLett.129.090601](https://doi.org/10.1103/PhysRevLett.129.090601).
- [57] Mehran Bagheri and Gary W. Slater. “Diffusion in an array of immobile anisotropic obstacles: The influence of local orientation, bottlenecks, and free volume in absence of dead-ends”. In: *Physica A: Statistical Mechanics and its Applications* 539 (2020), p. 122924. ISSN: 0378-4371. DOI: <https://doi.org/10.1016/j.physa.2019.122924>.
- [58] William S. Trimble and Sergio Grinstein. “Barriers to the free diffusion of proteins and lipids in the plasma membrane”. In: *Journal of Cell Biology* 208.3 (Feb. 2015), pp. 259–271. ISSN: 0021-9525. DOI: [10.1083/jcb.201410071](https://doi.org/10.1083/jcb.201410071).
- [59] Da-Jiang Liu and J. W. Evans. “Surface diffusion in mixed overlayers with superlattice ordering: Percolative transport around obstacles and along domain boundaries”. In: *The Journal of Chemical Physics* 113.22 (2000), pp. 10252–10264. DOI: [10.1063/1.1322356](https://doi.org/10.1063/1.1322356).
- [60] Yingchun Liu and Qi Wang. “Transport behavior of water confined in carbon nanotubes”. In: *Phys. Rev. B* 72 (8 Aug. 2005), p. 085420. DOI: [10.1103/PhysRevB.72.085420](https://doi.org/10.1103/PhysRevB.72.085420).

- [61] Zhixiang Zhao, Runfeng Zhou, and Chengzhen Sun. “Molecular dynamics study of water diffusivity in graphene nanochannels”. In: *International Journal of Thermophysics* 41 (2020), pp. 1–12.
- [62] Douwe Jan Bonthuis et al. “Conformation and Dynamics of DNA Confined in Slitlike Nanofluidic Channels”. In: *Phys. Rev. Lett.* 101 (10 Sept. 2008), p. 108303. doi: [10.1103/PhysRevLett.101.108303](https://doi.org/10.1103/PhysRevLett.101.108303).
- [63] Liang Dai et al. “Revisiting Blob Theory for DNA Diffusivity in Slitlike Confinement”. In: *Phys. Rev. Lett.* 110 (16 Apr. 2013), p. 168105. doi: [10.1103/PhysRevLett.110.168105](https://doi.org/10.1103/PhysRevLett.110.168105).
- [64] David W Oxtoby. “Homogeneous nucleation: theory and experiment”. In: *Journal of Physics: Condensed Matter* 4.38 (1992), p. 7627.
- [65] Paul Meakin. “Simulation of the kinetics of aggregation: Fractals and scaling”. In: *Croatica Chemica Acta* 65.2 (1992), pp. 237–267.
- [66] Sujin Babu, Jean Christophe Gimel, and Taco Nicolai. “Phase separation and percolation of reversibly aggregating spheres with a square-well attraction potential”. In: *The Journal of Chemical Physics* 125.18 (2006), p. 184512. doi: [10.1063/1.2378832](https://doi.org/10.1063/1.2378832).
- [67] CN Likos. “Colloidal interactions: From effective potentials to structure”. In: *La Rivista del Nuovo Cimento* 37 (2014), pp. 125–180.
- [68] Francesco Sciortino. “Entropy in self-assembly”. In: *La Rivista del Nuovo Cimento* 42 (2019), pp. 511–548.
- [69] Paul Meakin, Zhong-Ying Chen, and Pierre Evesque. “Aggregation of anisotropic particles”. In: *The Journal of Chemical Physics* 87.1 (1987), pp. 630–635. doi: [10.1063/1.453557](https://doi.org/10.1063/1.453557).

- [70] Kun Zhao and Thomas G Mason. “Assembly of colloidal particles in solution”. In: *Reports on Progress in Physics* 81.12 (Oct. 2018), p. 126601. doi: 10.1088/1361-6633/aad1a7.
- [71] Masahiro Kinoshita. “Importance of Translational Entropy of Water in Biological Self-Assembly Processes like Protein Folding”. In: *International Journal of Molecular Sciences* 10.3 (2009), pp. 1064–1080. ISSN: 1422-0067. doi: 10.3390/ijms10031064.
- [72] Edward Barry and Zvonimir Dogic. “Entropy driven self-assembly of nonamphiphilic colloidal membranes”. In: *Proceedings of the National Academy of Sciences* 107.23 (2010), pp. 10348–10353. doi: 10.1073/pnas.1000406107.
- [73] Ennio Lavagnini et al. “Translation of Chemical Structure into Dissipative Particle Dynamics Parameters for Simulation of Surfactant Self-Assembly”. In: *The Journal of Physical Chemistry B* 125.15 (2021). PMID: 33848165, pp. 3942–3952. doi: 10.1021/acs.jpcb.1c00480.
- [74] Wei Li and James D. Gunton. “Self-Assembly of Janus Ellipsoids II: Janus Prolate Spheroids”. In: *Langmuir* 29.27 (2013). PMID: 23742624, pp. 8517–8523. doi: 10.1021/la4016614.
- [75] Atakan Tevlek et al. “Spheroid Engineering in Microfluidic Devices”. In: *ACS Omega* 8.4 (2023), pp. 3630–3649. doi: 10.1021/acsomega.2c06052.
- [76] Liam J. Ruske and Julia M. Yeomans. “Activity-driven tissue alignment in proliferating spheroids”. In: *Soft Matter* 19 (5 2023), pp. 921–931. doi: 10.1039/D2SM01239A.
- [77] Luís P. Ferreira et al. “Organotypic 3D decellularized matrix tumor spheroids for high-throughput drug screening”. In: *Biomaterials* 275 (2021), p. 120983. ISSN: 0142-9612. doi: <https://doi.org/10.1016/j.biomaterials.2021.120983>.

- [78] Adrien Saint-Sardos et al. “High-Throughput Measurements of Intra-Cellular and Secreted Cytokine from Single Spheroids Using Anchored Microfluidic Droplets”. In: *Small* 16.49 (2020), p. 2002303. DOI: <https://doi.org/10.1002/smll.202002303>.
- [79] Lilian C Hsiao et al. “Metastable orientational order of colloidal discoids”. In: *Nature Communications* 6.1 (2015), p. 8507.
- [80] Xuan Guo and Jianlong Wang. “Modeling of the fractal-like adsorption systems based on the diffusion limited aggregation model”. In: *Journal of Molecular Liquids* 324 (2021), p. 114692. ISSN: 0167-7322. DOI: <https://doi.org/10.1016/j.molliq.2020.114692>.
- [81] Hai Chen et al. “The development of natural and designed protein nanocages for encapsulation and delivery of active compounds”. In: *Food Hydrocolloids* 121 (2021), p. 107004. ISSN: 0268-005X. DOI: <https://doi.org/10.1016/j.foodhyd.2021.107004>.
- [82] Sanaz Panahandeh, Siyu Li, and Roya Zandi. “The equilibrium structure of self-assembled protein nano-cages”. In: *Nanoscale* 10.48 (2018), pp. 22802–22809.
- [83] Meital Reches and Ehud Gazit. “Formation of Closed-Cage Nanostructures by Self-Assembly of Aromatic Dipeptides”. In: *Nano Letters* 4.4 (2004), pp. 581–585. DOI: [10.1021/nl035159z](https://doi.org/10.1021/nl035159z).
- [84] Javad Beheshtian et al. “B12N12 nano-cage as potential sensor for NO₂ detection”. In: *Chinese Journal of Chemical Physics* 25.1 (2012), p. 60.
- [85] Jae-Hyuck Yoo et al. “Facile fabrication of a superhydrophobic cage by laser direct writing for site-specific colloidal self-assembled photonic crystal”. In: *Nanotechnology* 27.14 (Feb. 2016), p. 145604. DOI: [10.1088/0957-4484/27/14/145604](https://doi.org/10.1088/0957-4484/27/14/145604).

- [86] Majid Mosayebi et al. “Beyond icosahedral symmetry in packings of proteins in spherical shells”. In: *Proceedings of the National Academy of Sciences* 114.34 (2017), pp. 9014–9019.
- [87] Michael F Hagan and David Chandler. “Dynamic pathways for viral capsid assembly”. In: *Biophysical journal* 91.1 (2006), pp. 42–54.
- [88] DC Rapaport. “Self-assembly of polyhedral shells: a molecular dynamics study”. In: *Physical Review E* 70.5 (2004), p. 051905.
- [89] Norbert Kern and Daan Frenkel. “Fluid–fluid coexistence in colloidal systems with short-ranged strongly directional attraction”. In: *The Journal of Chemical Physics* 118.21 (2003), pp. 9882–9889. doi: [10.1063/1.1569473](https://doi.org/10.1063/1.1569473).
- [90] Lourdes Vega et al. “Phase equilibria and critical behavior of square-well fluids of variable width by Gibbs ensemble Monte Carlo simulation”. In: *The Journal of Chemical Physics* 96.3 (1992), pp. 2296–2305. doi: [10.1063/1.462080](https://doi.org/10.1063/1.462080).
- [91] Teun Vissers et al. “Predicting crystals of Janus colloids”. In: *The Journal of chemical physics* 138.16 (2013), p. 164505.
- [92] Isha Malhotra and Sujin B Babu. “Phase diagram of two-patch colloids with competing anisotropic and isotropic interactions”. In: *Journal of Physics: Condensed Matter* 32.35 (2020), p. 355101.
- [93] Achille Giacometti et al. “Phase diagram and structural properties of a simple model for one-patch particles”. In: *The Journal of chemical physics* 131.17 (2009), p. 174114.
- [94] Amar B Pawar and Ilona Kretzschmar. “Fabrication, assembly, and application of patchy particles”. In: *Macromolecular rapid communications* 31.2 (2010), pp. 150–168.

- [95] Emanuela Bianchi et al. “Phase Diagram of Patchy Colloids: Towards Empty Liquids”. In: *Phys. Rev. Lett.* 97 (16 Oct. 2006), p. 168301. DOI: [10.1103/PhysRevLett.97.168301](https://doi.org/10.1103/PhysRevLett.97.168301).
- [96] Xiuquan Sun, Teng Lin, and J. Daniel Gezelter. “Langevin dynamics for rigid bodies of arbitrary shape”. In: *J. Chem. Phys.* 128.23 (June 2008), p. 234107. ISSN: 0021-9606. DOI: [10.1063/1.2936991](https://doi.org/10.1063/1.2936991).
- [97] Sujin Babu et al. “The influence of bond rigidity and cluster diffusion on the self-diffusion of hard spheres with square well interaction”. In: *The Journal of Chemical Physics* 128.20 (2008), p. 204504. DOI: [10.1063/1.2925686](https://doi.org/10.1063/1.2925686).
- [98] Daniel ben-Avraham and Shlomo Havlin. *Diffusion and Reactions in Fractals and Disordered Systems*. Cambridge: Cambridge University Press, 2000. DOI: [10.1017/CBO9780511605826](https://doi.org/10.1017/CBO9780511605826).
- [99] A. Prabhu et al. “Brownian cluster dynamics with short range patchy interactions: Its application to polymers and step-growth polymerization”. In: *The Journal of Chemical Physics* 141.2 (2014), p. 024904. DOI: [10.1063/1.4886585](https://doi.org/10.1063/1.4886585).
- [100] Isha Malhotra and Sujin B. Babu. “Aggregation kinetics of irreversible patches coupled with reversible isotropic interaction leading to chains, bundles and globules”. In: *Pure and Applied Chemistry* 90.6 (2018), pp. 1085–1098. DOI: [10.1515/pac-2017-0910](https://doi.org/10.1515/pac-2017-0910).
- [101] Jan K. G. Dhont. “Chapter 2 - Brownian Motion of Non-Interacting Particles”. In: *Studies in Interface Science*. Vol. 2. Elsevier, 1996, pp. 69–105. DOI: [10.1016/S1383-7303\(96\)80004-4](https://doi.org/10.1016/S1383-7303(96)80004-4).

- [102] R. Vasanthi, Sarika Bhattacharyya, and Biman Bagchi. “Anisotropic diffusion of spheroids in liquids: Slow orientational relaxation of the oblates”. In: *The Journal of Chemical Physics* 116.3 (2002), pp. 1092–1096. doi: [10.1063/1.1428343](https://doi.org/10.1063/1.1428343).
- [103] Perrin, Francis. “Mouvement brownien d’un ellipsoïde - I. Dispersion diélectrique pour des molécules ellipsoidales”. In: *J. Phys. Radium* 5.10 (1934), pp. 497–511. doi: [10.1051/jphysrad:01934005010049700](https://doi.org/10.1051/jphysrad:01934005010049700).
- [104] Zhongyu Zheng and Yilong Han. “Self-diffusion in two-dimensional hard ellipsoid suspensions”. In: *J. Chem. Phys.* 133.12 (Sept. 2010), p. 124509. ISSN: 0021-9606. doi: [10.1063/1.3490669](https://doi.org/10.1063/1.3490669).
- [105] J. Happel and H. Brenner. *Low Reynolds number hydrodynamics with special applications to particulate media*. 1st ed. 1. Springer Netherlands, 1983. ISBN: 978-94-009-8352-6. doi: [10.1007/978-94-009-8352-6](https://doi.org/10.1007/978-94-009-8352-6).
- [106] Sujin Babu et al. “The influence of bond rigidity and cluster diffusion on the self-diffusion of hard spheres with square well interaction”. In: *The Journal of Chemical Physics* 128.20 (May 2008), p. 204504. ISSN: 0021-9606. doi: [10.1063/1.2925686](https://doi.org/10.1063/1.2925686).
- [107] Vasilios I Manousiouthakis and Michael W Deem. “Strict detailed balance is unnecessary in Monte Carlo simulation”. In: *The Journal of chemical physics* 110.6 (1999), pp. 2753–2756.
- [108] Kazem V. Edmond et al. “Decoupling of rotational and translational diffusion in supercooled colloidal fluids”. In: *Proceedings of the National Academy of Sciences* 109.44 (2012), pp. 17891–17896. doi: [10.1073/pnas.1203328109](https://doi.org/10.1073/pnas.1203328109).
- [109] Daan Frenkel and Berend Smit. *Understanding molecular simulation*. Vol. 1. Elsevier, 2001.

- [110] John W. Perram and M.S. Wertheim. “Statistical mechanics of hard ellipsoids. I. Overlap algorithm and the contact function”. In: *Journal of Computational Physics* 58.3 (1985), pp. 409–416. ISSN: 0021-9991. DOI: [https://doi.org/10.1016/0021-9991\(85\)90171-8](https://doi.org/10.1016/0021-9991(85)90171-8).
- [111] Christer Ericson. *Real-time collision detection*. Crc Press, 2004.
- [112] Laura Filion et al. “Efficient Method for Predicting Crystal Structures at Finite Temperature: Variable Box Shape Simulations”. In: *Phys. Rev. Lett.* 103 (18 Oct. 2009), p. 188302. DOI: 10.1103/PhysRevLett.103.188302.
- [113] Daniela J Kraft et al. “Surface roughness directed self-assembly of patchy particles into colloidal micelles”. In: *Proceedings of the National Academy of Sciences* 109.27 (2012), pp. 10787–10792.
- [114] Matthew Dennison and Andrew J Masters. “High-level virial theory of hard spheroids”. In: *Physical Review E* 84.2 (2011), p. 021709.
- [115] Daan Frenkel and Berend Smit. *Understanding Molecular Simulation*. 1st. USA: Academic Press, Inc., 1996. ISBN: 0122673700.
- [116] Matthew Dennison and Andrew J. Masters. “High-level virial theory of hard spheroids”. In: *Phys. Rev. E* 84 (2 Aug. 2011), p. 021709. DOI: 10.1103/PhysRevE.84.021709.
- [117] Daniela J. Kraft et al. “Surface roughness directed self-assembly of patchy particles into colloidal micelles”. In: *Proceedings of the National Academy of Sciences* 109.27 (2012), pp. 10787–10792. DOI: 10.1073/pnas.1116820109.
- [118] René Pool and Peter G. Bolhuis. “Accurate Free Energies of Micelle Formation”. In: *The Journal of Physical Chemistry B* 109.14 (2005). PMID: 16851747, pp. 6650–6657. DOI: 10.1021/jp045576f.

- [119] Teun Vissers et al. “Predicting crystals of Janus colloids”. In: *The Journal of Chemical Physics* 138.16 (2013), p. 164505. DOI: 10.1063/1.4801438.
- [120] Daan Frenkel and Anthony J. C. Ladd. “New Monte Carlo method to compute the free energy of arbitrary solids. Application to the fcc and hcp phases of hard spheres”. In: *The Journal of Chemical Physics* 81.7 (1984), pp. 3188–3193. DOI: 10.1063/1.448024.
- [121] C Vega et al. “Determination of phase diagrams via computer simulation: methodology and applications to water, electrolytes and proteins”. In: *Journal of Physics: Condensed Matter* 20.15 (Mar. 2008), p. 153101. DOI: 10.1088/0953-8984/20/15/153101.
- [122] Teun Vissers et al. “Predicting crystals of Janus colloids”. In: *The Journal of Chemical Physics* 138.16 (2013), p. 164505. DOI: 10.1063/1.4801438.
- [123] Jade Taffs and C. Patrick Royall. “The role of fivefold symmetry in suppressing crystallization”. In: *Nature Communications* 7.1 (2016), p. 13225. ISSN: 2041-1723. DOI: 10.1038/ncomms13225.
- [124] P. N. Pusey et al. “Hard spheres: crystallization and glass formation”. In: *Philosophical Transactions of the Royal Society A: Mathematical, Physical and Engineering Sciences* 367.1909 (Dec. 2009), pp. 4993–5011. DOI: 10.1098/rsta.2009.0181.
- [125] Tatjana Sentjabrskaja et al. “Anomalous dynamics of intruders in a crowded environment of mobile obstacles”. In: *Nature Communications* 7.1 (2016), p. 11133. ISSN: 2041-1723. DOI: 10.1038/ncomms11133.
- [126] S. Babu et al. “Flocculation and percolation in reversible cluster-cluster aggregation”. In: *The European Physical Journal E* 19.2 (2006), pp. 203–211. ISSN: 1292-895X. DOI: 10.1140/epje/e2006-00022-7.

- [127] S. O. Morgan et al. “Adsorption trajectories of nonspherical particles at liquid interfaces”. In: *PRE* 103.4 (Apr. 2021), p. 042604. DOI: [10.1103/PhysRevE.103.042604](https://doi.org/10.1103/PhysRevE.103.042604).
- [128] Emanuela Zaccarelli and Wilson C. K. Poon. “Colloidal glasses and gels: The interplay of bonding and caging”. In: *Proc Natl Acad Sci USA* 106.36 (Sept. 2009), p. 15203. DOI: [10.1073/pnas.0902294106](https://doi.org/10.1073/pnas.0902294106).
- [129] Sujin Babu, Jean-Christophe Gimel, and Taco Nicolai. “Crystallization and dynamical arrest of attractive hard spheres”. In: *The Journal of Chemical Physics* 130.6 (2009), p. 064504. DOI: [10.1063/1.3074310](https://doi.org/10.1063/1.3074310).
- [130] Néstor E. Valadez-Pérez, Yun Liu, and Ramón Castañeda-Priego. “Reversible Aggregation and Colloidal Cluster Morphology: The Importance of the Extended Law of Corresponding States”. In: *Phys. Rev. Lett.* 120 (24 June 2018), p. 248004. DOI: [10.1103/PhysRevLett.120.248004](https://doi.org/10.1103/PhysRevLett.120.248004).
- [131] Theodore Hueckel, Glen M. Hocky, and Stefano Sacanna. “Total synthesis of colloidal matter”. In: *Nature Reviews Materials* (2021). ISSN: 2058-8437. DOI: [10.1038/s41578-021-00323-x](https://doi.org/10.1038/s41578-021-00323-x).
- [132] Jin Suk Myung et al. “Weak Shape Anisotropy Leads to a Nonmonotonic Contribution to Crowding, Impacting Protein Dynamics under Physiologically Relevant Conditions”. In: *J. Phys. Chem. B* 122.51 (Dec. 2018), pp. 12396–12402. ISSN: 1520-6106. DOI: [10.1021/acs.jpcb.8b07901](https://doi.org/10.1021/acs.jpcb.8b07901).
- [133] Pal Antara et al. “Anisotropic dynamics and kinetic arrest of dense colloidal ellipsoids in the presence of an external field studied by differential dynamic microscopy”. In: *Science Advances* 6.3 (Sept. 2021), eaaw9733. DOI: [10.1126/sciadv.aaw9733](https://doi.org/10.1126/sciadv.aaw9733).

- [134] Kazem V. Edmond et al. “Decoupling of rotational and translational diffusion in supercooled colloidal fluids”. In: *Proc Natl Acad Sci USA* 109.44 (Oct. 2012), p. 17891. DOI: 10.1073/pnas.1203328109.
- [135] Jörg Roller et al. “Observation of liquid glass in suspensions of ellipsoidal colloids”. In: *Proceedings of the National Academy of Sciences* 118.3 (2021), pp. 1–8. ISSN: 0027-8424. DOI: 10.1073/pnas.2018072118.
- [136] Alejandro Cuetos and Alessandro Patti. “Dynamics of hard colloidal cuboids in nematic liquid crystals”. In: *Phys. Rev. E* 101 (5 May 2020), p. 052702. DOI: 10.1103/PhysRevE.101.052702.
- [137] Wen Sheng Xu et al. “Hard ellipses: Equation of state, structure, and self-diffusion”. In: *The Journal of Chemical Physics* 139.2 (2013), p. 024501. DOI: 10.1063/1.4812361. eprint: <https://doi.org/10.1063/1.4812361>.
- [138] Zhongyu Zheng et al. “Translational and rotational critical-like behaviors in the glass transition of colloidal ellipsoid monolayers”. In: *Science Advances* 7.3 (2021). DOI: 10.1126/sciadv.abd1958. eprint: <https://advances.sciencemag.org/content/7/3/eabd1958.full.pdf>.
- [139] S. Davatolhagh and S. Foroozan. “Structural origin of enhanced translational diffusion in two-dimensional hard-ellipse fluids”. In: *Phys. Rev. E* 85 (6 June 2012), p. 061707. DOI: 10.1103/PhysRevE.85.061707.
- [140] Yi Peng et al. “Diffusion of Ellipsoids in Bacterial Suspensions”. In: *Phys. Rev. Lett.* 116 (6 Feb. 2016), p. 068303. DOI: 10.1103/PhysRevLett.116.068303.
- [141] Anna Stradner and Peter Schurtenberger. “Potential and limits of a colloid approach to protein solutions”. In: *Soft Matter* 16 (2 2020), pp. 307–323. DOI: 10.1039/C9SM01953G.

- [142] Y. Han et al. “Brownian Motion of an Ellipsoid”. In: *Science* 314.5799 (2006), pp. 626–630. DOI: [10.1126/science.1130146](https://doi.org/10.1126/science.1130146).
- [143] Cristiano De Michele et al. “Molecular correlation functions for uniaxial ellipsoids in the isotropic state”. In: *J. Chem. Phys.* 124.10 (Mar. 2006), p. 104509. ISSN: 0021-9606. DOI: [10.1063/1.2176679](https://doi.org/10.1063/1.2176679).
- [144] M. Letz, R. Schilling, and A. Latz. “Ideal glass transitions for hard ellipsoids”. In: *PRE* 62.4 (Oct. 2000), pp. 5173–5178. DOI: [10.1103/PhysRevE.62.5173](https://doi.org/10.1103/PhysRevE.62.5173).
- [145] Avishek Das and David T. Limmer. “Variational design principles for nonequilibrium colloidal assembly”. In: *J. Chem. Phys.* 154.1 (Jan. 2021), p. 014107. ISSN: 0021-9606. DOI: [10.1063/5.0038652](https://doi.org/10.1063/5.0038652).
- [146] Peter Bereolos et al. “Transport properties of the hard ellipsoid fluid”. In: *The Journal of Chemical Physics* 99.8 (1993), pp. 6087–6097. DOI: [10.1063/1.466221](https://doi.org/10.1063/1.466221).
- [147] Norbert Kern and Daan Frenkel. “Fluid–fluid coexistence in colloidal systems with short-ranged strongly directional attraction”. In: *The Journal of Chemical Physics* 118.21 (2003), pp. 9882–9889. DOI: [10.1063/1.1569473](https://doi.org/10.1063/1.1569473). eprint: <https://doi.org/10.1063/1.1569473>.
- [148] D. Frenkel and B. M. Mulder. “The hard ellipsoid-of-revolution fluid”. In: *Molecular Physics* 55.5 (Aug. 1985), pp. 1171–1192. ISSN: 0026-8976. DOI: [10.1080/00268978500101971](https://doi.org/10.1080/00268978500101971).
- [149] Jean Christophe Gimel, Dominique Durand, and Taco Nicolai. “Transition between flocculation and percolation of a diffusion-limited cluster-cluster aggregation process using three-dimensional Monte Carlo simulation”. In: *PRB* 51.17 (May 1995), pp. 11348–11357. DOI: [10.1103/PhysRevB.51.11348](https://doi.org/10.1103/PhysRevB.51.11348).

- [150] J. C. Gimel, T. Nicolai, and D. Durand. “3D Monte Carlo Simulations of Diffusion Limited Cluster Aggregation up to the Sol-Gel Transition: Structure and Kinetics”. In: *Journal of Sol-Gel Science and Technology* 15.2 (1999), pp. 129–136. ISSN: 1573-4846. DOI: 10.1023/A:1008735404991.
- [151] M. Rottereau et al. “Monte Carlo simulation of particle aggregation and gelation: I. Growth, structure and size distribution of the clusters”. In: *The European Physical Journal E* 15.2 (2004), pp. 133–140. ISSN: 1292-895X. DOI: 10.1140/epje/i2004-10044-x.
- [152] M. Rottereau et al. “Monte Carlo simulation of particle aggregation and gelation: II. Pair correlation function and structure factor”. In: *The European Physical Journal E* 15.2 (2004), pp. 141–148. ISSN: 1292-895X. DOI: 10.1140/epje/i2004-10045-9.
- [153] Sujin Babu, Jean Christophe Gimel, and Taco Nicolai. “Self-diffusion of reversibly aggregating spheres”. In: *J. Chem. Phys.* 127.5 (Aug. 2007), p. 054503. ISSN: 0021-9606. DOI: 10.1063/1.2756838.
- [154] S. Babu, J. C. Gimel, and T. Nicolai. “Diffusion limited cluster aggregation with irreversible slippery bonds”. In: *The European Physical Journal E* 27.3 (2008), pp. 297–308. ISSN: 1292-895X. DOI: 10.1140/epje/i2008-10381-8.
- [155] Zakiya Shireen and Sujin B. Babu. “Lattice animals in diffusion limited binary colloidal system”. In: *J. Chem. Phys.* 147.5 (Aug. 2017), p. 054904. ISSN: 0021-9606. DOI: 10.1063/1.4996739.
- [156] Zakiya Shireen and Sujin B. Babu. “Cage dynamics leads to double relaxation of the intermediate scattering function in a binary colloidal system”. In: *Soft Matter* 14.45 (2018), pp. 9271–9281. ISSN: 1744-683X. DOI: 10.1039/C8SM01474D.

- [157] I. Malhotra and S. B. Babu. “Mobile obstacles accelerate and inhibit the bundle formation in two-patch colloidal particle”. In: *J. Chem. Phys.* 151.8 (Aug. 2019), p. 084901. ISSN: 0021-9606. DOI: [10.1063/1.5110777](https://doi.org/10.1063/1.5110777).
- [158] Isha Malhotra and Sujin B. Babu. “Phase diagram of two-patch colloids with competing anisotropic and isotropic interactions”. In: *Journal of Physics: Condensed Matter* 32.35 (2020), p. 355101. ISSN: 1361-648X. DOI: [10.1088/1361-648x/ab8c8e](https://doi.org/10.1088/1361-648x/ab8c8e).
- [159] R. Vasanthi, Sarika Bhattacharyya, and Biman Bagchi. “Anisotropic diffusion of spheroids in liquids: Slow orientational relaxation of the oblates”. In: *The Journal of Chemical Physics* 116.3 (2002), pp. 1092–1096. DOI: [10.1063/1.1428343](https://doi.org/10.1063/1.1428343).
- [160] Witold Dzwinel, Jacek Kitowski, and Jacek Mościński. ““Checker Board” Periodic Boundary Conditions in Molecular Dynamics Codes”. In: *Molecular Simulation* 7 (May 1991), pp. 171–179. DOI: [10.1080/08927029108022151](https://doi.org/10.1080/08927029108022151).
- [161] Cristiano De Michele. “Simulating Hard Rigid Bodies”. In: *Journal of Computational Physics* 229 (Mar. 2009), pp. 3276–3294. DOI: [10.1016/j.jcp.2010.01.002](https://doi.org/10.1016/j.jcp.2010.01.002).
- [162] Shuang Tang et al. “Shear viscosity for fluids of hard ellipsoids: A kinetic theory and molecular dynamics study”. In: *The Journal of Chemical Physics* 102.9 (1995), pp. 3794–3811. DOI: [10.1063/1.468561](https://doi.org/10.1063/1.468561).
- [163] B. Van Roie et al. “Weakly first-order character of the nematic-isotropic phase transition in liquid crystals”. In: *PRE* 72.4 (Oct. 2005), p. 041702. DOI: [10.1103/PhysRevE.72.041702](https://doi.org/10.1103/PhysRevE.72.041702).
- [164] R. Eppenga and D. Frenkel. “Monte Carlo study of the isotropic and nematic phases of infinitely thin hard platelets”. In: *Molecular Physics* 52.6 (1984), pp. 1303–1334. DOI: [10.1080/00268978400101951](https://doi.org/10.1080/00268978400101951).

- [165] Gerardo Odriozola. “Revisiting the phase diagram of hard ellipsoids”. In: *The Journal of Chemical Physics* 136.13 (2012), p. 134505. doi: 10.1063/1.3699331.
- [166] Gustavo Bautista-Carbajal, Arturo Moncho-Jordá, and Gerardo Odriozola. “Further details on the phase diagram of hard ellipsoids of revolution”. In: *The Journal of Chemical Physics* 138.6 (2013), p. 064501. doi: 10.1063/1.4789957.
- [167] Michael P. Allen. “Diffusion coefficient increases with density in hard ellipsoid liquid crystals”. In: *Phys. Rev. Lett.* 65 (23 Dec. 1990), pp. 2881–2884.
- [168] Dmytro Antypov and Douglas J. Cleaver. “Orientational and phase-coexistence behaviour of hard rod-sphere mixtures”. In: *Chemical Physics Letters* 377.3 (2003), pp. 311–316. ISSN: 0009-2614. doi: 10.1016/S0009-2614(03)01157-6.
- [169] Carlos E. Alavrez and Martial Mazars. “Mixtures of hard ellipsoids and spheres: Stability of the nematic phase”. In: *arXiv:1405.2357* (2014).
- [170] Adam Samborski and Glenn T. Evans. “Binary hard sphere, hard ellipsoid liquid crystal mixtures”. In: *J. Chem. Phys.* 101.7 (Oct. 1994), pp. 6005–6012. ISSN: 0021-9606. doi: 10.1063/1.467315.
- [171] Giuseppe Foffi and Francesco Sciortino. “On the possibility of extending the noro- frenkel generalized law of correspondent states to nonisotropic patchy interactions”. In: *The Journal of Physical Chemistry B* 111.33 (2007), pp. 9702–9705.
- [172] Vikki Anand Varma, Isha Malhotra, and Sujin B. Babu. “Enhancement in the diffusivity of Brownian spheroids in the presence of spheres”. In: *PRE* 106.1 (July 2022), p. 014602. doi: 10.1103/PhysRevE.106.014602.

- [173] Michael A. Boles, Michael Engel, and Dmitri V. Talapin. “Self-Assembly of Colloidal Nanocrystals: From Intricate Structures to Functional Materials”. In: *Chem. Rev.* 116.18 (Sept. 2016), pp. 11220–11289. ISSN: 0009-2665. DOI: [10.1021/acs.chemrev.6b00196](https://doi.org/10.1021/acs.chemrev.6b00196).
- [174] Nuno M. Silvestre et al. “Towards Template-Assisted Assembly of Nematic Colloids”. In: *PRL* 112.22 (June 2014), p. 225501. DOI: [10.1103/PhysRevLett.112.225501](https://doi.org/10.1103/PhysRevLett.112.225501).
- [175] Antti-Pekka Hynninen et al. “Self-assembly route for photonic crystals with a bandgap in the visible region”. In: *Nature Materials* 6.3 (2007), pp. 202–205. ISSN: 1476-4660. DOI: [10.1038/nmat1841](https://doi.org/10.1038/nmat1841).
- [176] Dengping Lyu et al. “Low-dimensional assemblies of metal-organic framework particles and mutually coordinated anisotropy”. In: *Nature Communications* 13.1 (2022), p. 3980. ISSN: 2041-1723. DOI: [10.1038/s41467-022-31651-3](https://doi.org/10.1038/s41467-022-31651-3).
- [177] Mingzhu Liu et al. “Two-Dimensional (2D) or Quasi-2D Superstructures from DNA-Coated Colloidal Particles”. In: *Angew. Chem. Int. Ed.* 60.11 (Mar. 2021), pp. 5744–5748. ISSN: 1433-7851. DOI: [10.1002/anie.202014045](https://doi.org/10.1002/anie.202014045).
- [178] Mingxin He et al. “Colloidal diamond”. In: *Nature* 585.7826 (2020), pp. 524–529. ISSN: 1476-4687. DOI: [10.1038/s41586-020-2718-6](https://doi.org/10.1038/s41586-020-2718-6).
- [179] Frank Smallenburg and Francesco Sciortino. “Liquids more stable than crystals in particles with limited valence and flexible bonds”. In: *Nature Physics* 9.9 (2013), pp. 554–558. ISSN: 1745-2481. DOI: [10.1038/nphys2693](https://doi.org/10.1038/nphys2693).
- [180] Yang Liu et al. “Assembly of Colloidal Clusters Driven by the Polyhedral Shape of Metal-Organic Framework Particles”. In: *J. Am. Chem. Soc.* 143.33 (Aug. 2021), pp. 12943–12947. ISSN: 0002-7863. DOI: [10.1021/jacs.1c05363](https://doi.org/10.1021/jacs.1c05363).

- [181] Hossein Zargartalebi, S. Hossein Hejazi, and Amir Sanati-Nezhad. “Self-assembly of highly ordered micro- and nanoparticle deposits”. In: *Nature Communications* 13.1 (2022), p. 3085. ISSN: 2041-1723. DOI: [10.1038/s41467-022-30660-6](https://doi.org/10.1038/s41467-022-30660-6).
- [182] Civan Avci et al. “Template-Free, Surfactant-Mediated Orientation of Self-Assembled Supercrystals of Metal-Organic Framework Particles”. In: *Small* 15.31 (Aug. 2019), p. 1902520. ISSN: 1613-6810. DOI: [10.1002/smll.201902520](https://doi.org/10.1002/smll.201902520).
- [183] Luke A. Galuska et al. “SMART transfer method to directly compare the mechanical response of water-supported and free-standing ultrathin polymeric films”. In: *Nature Communications* 12.1 (2021), p. 2347. ISSN: 2041-1723. DOI: [10.1038/s41467-021-22473-w](https://doi.org/10.1038/s41467-021-22473-w).
- [184] Yu-Wei Sun et al. “Colloidal cubic diamond photonic crystals through cooperative self-assembly”. In: *Soft Matter* 18.13 (2022), pp. 2654–2662. ISSN: 1744-683X. DOI: [10.1039/D1SM01770E](https://doi.org/10.1039/D1SM01770E).
- [185] You-Jin Kim et al. “Advances in Colloidal Building Blocks: Toward Patchy Colloidal Clusters”. In: *Adv. Mater.* n/a.n/a (Aug. 2022), p. 2203045. ISSN: 0935-9648. DOI: [10.1002/adma.202203045](https://doi.org/10.1002/adma.202203045).
- [186] Srinivas Mushnoori et al. “Controlling morphology in hybrid isotropic/patchy particle assemblies”. In: *J. Chem. Phys.* 156.2 (Dec. 2021), p. 024501. ISSN: 0021-9606. DOI: [10.1063/5.0076914](https://doi.org/10.1063/5.0076914).
- [187] Katarina Gvozden et al. “Self-Assembly of All-DNA Rods with Controlled Patchiness”. In: *Small* 18.5 (Feb. 2022), p. 2104510. ISSN: 1613-6810. DOI: [10.1002/smll.202104510](https://doi.org/10.1002/smll.202104510).
- [188] Shunzhi Wang et al. “The emergence of valency in colloidal crystals through electron equivalents”. In: *Nature Materials* 21.5 (2022), pp. 580–587. ISSN: 1476-4660. DOI: [10.1038/s41563-021-01170-5](https://doi.org/10.1038/s41563-021-01170-5).

- [189] Flavio Romano and Francesco Sciortino. “Two dimensional assembly of tri-block Janus particles into crystal phases in the two bond per patch limit”. In: *Soft Matter* 7 (12 2011), pp. 5799–5804. DOI: [10.1039/C0SM01494J](https://doi.org/10.1039/C0SM01494J).
- [190] Zdenek Preisler et al. “Phase Diagram of One-Patch Colloids Forming Tubes and Lamellae”. In: *The Journal of Physical Chemistry B* 117.32 (2013). PMID: 23902159, pp. 9540–9547. DOI: [10.1021/jp404053t](https://doi.org/10.1021/jp404053t).
- [191] Liang Hong et al. “Clusters of Charged Janus Spheres”. In: *Nano Letters* 6.11 (2006). PMID: 17090082, pp. 2510–2514. DOI: [10.1021/nl061857i](https://doi.org/10.1021/nl061857i).
- [192] Yufeng Wang et al. “Colloids with valence and specific directional bonding”. In: *Nature* 491.7422 (2012), pp. 51–55.
- [193] Alicia M Jackson, Jacob W Myerson, and Francesco Stellacci. “Spontaneous assembly of subnanometre-ordered domains in the ligand shell of monolayer-protected nanoparticles”. In: *Nature materials* 3.5 (2004), pp. 330–336.
- [194] Wei Li and James D. Gunton. “Self-Assembly of Janus Ellipsoids II: Janus Prolate Spheroids”. In: *Langmuir* 29.27 (2013). PMID: 23742624, pp. 8517–8523. DOI: [10.1021/la4016614](https://doi.org/10.1021/la4016614).
- [195] Gerardo Odriozola. “Revisiting the phase diagram of hard ellipsoids”. In: *The Journal of Chemical Physics* 136.13 (2012), p. 134505. DOI: [10.1063/1.3699331](https://doi.org/10.1063/1.3699331).
- [196] A. Prabhu et al. “Brownian cluster dynamics with short range patchy interactions: Its application to polymers and step-growth polymerization”. In: *The Journal of Chemical Physics* 141.2 (2014), p. 024904. DOI: [10.1063/1.4886585](https://doi.org/10.1063/1.4886585).

- [197] R. Martoňák, A. Laio, and M. Parrinello. “Predicting Crystal Structures: The Parrinello-Rahman Method Revisited”. In: *Phys. Rev. Lett.* 90 (7 Feb. 2003), p. 075503. DOI: [10.1103/PhysRevLett.90.075503](https://doi.org/10.1103/PhysRevLett.90.075503).
- [198] Laura Filion et al. “Efficient Method for Predicting Crystal Structures at Finite Temperature: Variable Box Shape Simulations”. In: *Phys. Rev. Lett.* 103 (18 Oct. 2009), p. 188302. DOI: [10.1103/PhysRevLett.103.188302](https://doi.org/10.1103/PhysRevLett.103.188302).
- [199] Dieter Gottwald, Gerhard Kahl, and Christos N. Likos. “Predicting equilibrium structures in freezing processes”. In: *The Journal of Chemical Physics* 122.20 (2005), p. 204503. DOI: [10.1063/1.1901585](https://doi.org/10.1063/1.1901585).
- [200] Emanuela Bianchi et al. “Predicting patchy particle crystals: Variable box shape simulations and evolutionary algorithms”. In: *The Journal of Chemical Physics* 136.21 (2012), p. 214102. DOI: [10.1063/1.4722477](https://doi.org/10.1063/1.4722477).
- [201] Zdenek Preisler et al. “Phase Diagram of One-Patch Colloids Forming Tubes and Lamellae”. In: *J. Phys. Chem. B* 117.32 (Aug. 2013), pp. 9540–9547. ISSN: 1520-6106. DOI: [10.1021/jp404053t](https://doi.org/10.1021/jp404053t).
- [202] Teun Vissers et al. “Predicting crystals of Janus colloids”. In: *J. Chem. Phys.* 138.16 (Apr. 2013), p. 164505. ISSN: 0021-9606. DOI: [10.1063/1.4801438](https://doi.org/10.1063/1.4801438).
- [203] Qian Chen, Sung Chul Bae, and Steve Granick. “Directed self-assembly of a colloidal kagome lattice”. In: *Nature* 469.7330 (2011), pp. 381–384. ISSN: 1476-4687. DOI: [10.1038/nature09713](https://doi.org/10.1038/nature09713).
- [204] R. Eppenga and D. Frenkel. “Monte Carlo study of the isotropic and nematic phases of infinitely thin hard platelets”. In: *Molecular Physics* 52.6 (1984), pp. 1303–1334. DOI: [10.1080/00268978400101951](https://doi.org/10.1080/00268978400101951).

- [205] David A. Kofke. “Direct evaluation of phase coexistence by molecular simulation via integration along the saturation line”. In: *The Journal of Chemical Physics* 98.5 (1993), pp. 4149–4162. DOI: [10.1063/1.465023](https://doi.org/10.1063/1.465023).
- [206] David A. Kofke. “Gibbs-Duhem integration: a new method for direct evaluation of phase coexistence by molecular simulation”. In: *Molecular Physics* 78.6 (1993), pp. 1331–1336. DOI: [10.1080/00268979300100881](https://doi.org/10.1080/00268979300100881).
- [207] Yang Hsia et al. “Design of a hyperstable 60-subunit protein icosahedron”. In: *Nature* 535.7610 (2016), pp. 136–139. ISSN: 1476-4687. DOI: [10.1038/nature18010](https://doi.org/10.1038/nature18010).
- [208] Dmitriy N. Shurpik et al. “Towards Universal Stimuli-Responsive Drug Delivery Systems: Pillar[5]arenes Synthesis and Self-Assembly into Nanocontainers with Tetrazole Polymers”. In: *Nanomaterials* 11.4 (2021), p. 947.
- [209] Jordan H. Swisher et al. “Nanoreactors for particle synthesis”. In: *Nature Reviews Materials* 7.6 (2022), pp. 428–448. ISSN: 2058-8437. DOI: [10.1038/s41578-021-00402-z](https://doi.org/10.1038/s41578-021-00402-z).
- [210] E. Shchukina and D. G. Shchukin. “Nanocontainer-Based Active Systems: From Self-Healing Coatings to Thermal Energy Storage”. In: *Langmuir* 35.26 (July 2019), pp. 8603–8611. ISSN: 0743-7463. DOI: [10.1021/acs.langmuir.9b00151](https://doi.org/10.1021/acs.langmuir.9b00151).
- [211] Christian Sigl et al. “Programmable icosahedral shell system for virus trapping”. In: *Nature Materials* 20.9 (2021), pp. 1281–1289. ISSN: 1476-4660. DOI: [10.1038/s41563-021-01020-4](https://doi.org/10.1038/s41563-021-01020-4).
- [212] Ruimin Gao et al. “A prototype protein nanocage minimized from carboxysomes with gated oxygen permeability”. In: *Proceedings of the National Academy of Sciences* 119.5 (Feb. 2022), e2104964119. DOI: [10.1073/pnas.2104964119](https://doi.org/10.1073/pnas.2104964119).

- [213] Kaori Kamata, Yu Lu, and Younan Xia. “Synthesis and Characterization of Monodispersed CoreShell Spherical Colloids with Movable Cores”. In: *Journal of the American Chemical Society* 125.9 (2003). PMID: 12603113, pp. 2384–2385. DOI: [10.1021/ja0292849](https://doi.org/10.1021/ja0292849).
- [214] Andrei S Susha et al. “Formation of luminescent spherical core-shell particles by the consecutive adsorption of polyelectrolyte and CdTe(S) nanocrystals on latex colloids”. In: *Colloids and Surfaces A: Physicochemical and Engineering Aspects* 163.1 (2000), pp. 39–44. ISSN: 0927-7757. DOI: [https://doi.org/10.1016/S0927-7757\(99\)00428-8](https://doi.org/10.1016/S0927-7757(99)00428-8).
- [215] Majid Mosayebi et al. “Beyond icosahedral symmetry in packings of proteins in spherical shells”. In: *Proceedings of the National Academy of Sciences* 114.34 (2017), pp. 9014–9019. DOI: [10.1073/pnas.1706825114](https://doi.org/10.1073/pnas.1706825114).
- [216] D. C. Rapaport. “Self-assembly of polyhedral shells: A molecular dynamics study”. In: *Phys. Rev. E* 70 (5 Nov. 2004), p. 051905. DOI: [10.1103/PhysRevE.70.051905](https://doi.org/10.1103/PhysRevE.70.051905).
- [217] Roya Zandi et al. “Origin of icosahedral symmetry in viruses”. In: *Proceedings of the National Academy of Sciences* 101.44 (2004), pp. 15556–15560. DOI: [10.1073/pnas.0405844101](https://doi.org/10.1073/pnas.0405844101).
- [218] Sarah Schyck et al. “Self-assembly of colloidal superballs under spherical confinement of a drying droplet”. In: *JCIS Open* 5 (2022), p. 100037. ISSN: 2666-934X. DOI: <https://doi.org/10.1016/j.jciso.2021.100037>.
- [219] Ankit Gangrade, Nicholas Stephanopoulos, and Dhiraj Bhatia. “Programmable, self-assembled DNA nanodevices for cellular programming and tissue engineering”. In: *Nanoscale* 13.40 (2021), pp. 16834–16846. ISSN: 2040-3364. DOI: [10.1039/D1NR04475C](https://doi.org/10.1039/D1NR04475C).

- [220] Swarup Dey et al. “DNA origami”. In: *Nature Reviews Methods Primers* 1.1 (2021), p. 13. ISSN: 2662-8449. DOI: [10.1038/s43586-020-00009-8](https://doi.org/10.1038/s43586-020-00009-8).
- [221] Heng Wang et al. “Double-Layered Supramolecular Prisms Self-Assembled by Geometrically Non-equivalent Tetratopic Subunits”. In: *Angew. Chem. Int. Ed.* 60.3 (Jan. 2021), pp. 1298–1305. ISSN: 1433-7851. DOI: [10.1002/anie.202010805](https://doi.org/10.1002/anie.202010805).
- [222] Aaron Michelson et al. “Three-dimensional visualization of nanoparticle lattices and multimaterial frameworks”. In: *Science* 376.6589 (Apr. 2022), pp. 203–207. DOI: [10.1126/science.abk0463](https://doi.org/10.1126/science.abk0463).
- [223] Eyal Golub et al. “Constructing protein polyhedra via orthogonal chemical interactions”. In: *Nature* 578.7793 (2020), pp. 172–176. ISSN: 1476-4687. DOI: [10.1038/s41586-019-1928-2](https://doi.org/10.1038/s41586-019-1928-2).
- [224] Zhenli Zhang and Sharon C. Glotzer. “Self-Assembly of Patchy Particles”. In: *Nano Lett.* 4.8 (Aug. 2004), pp. 1407–1413. ISSN: 1530-6984. DOI: [10.1021/nl0493500](https://doi.org/10.1021/nl0493500).
- [225] Mingzhu Liu et al. “Tunable assembly of hybrid colloids induced by regioselective depletion”. In: *Nature Materials* 19.12 (2020), pp. 1354–1361. ISSN: 1476-4660. DOI: [10.1038/s41563-020-0744-2](https://doi.org/10.1038/s41563-020-0744-2).
- [226] Sangmin Lee, Thi Vo, and Sharon C. Glotzer. “Entropy compartmentalization stabilizes open host-guest colloidal clathrates”. In: *Nature Chemistry* (2023). ISSN: 1755-4349. DOI: [10.1038/s41557-023-01200-6](https://doi.org/10.1038/s41557-023-01200-6).
- [227] Diogo E. P. Pinto et al. “Design strategies for the self-assembly of polyhedral shells”. In: *Proceedings of the National Academy of Sciences* 120.16 (Apr. 2023), e2219458120. DOI: [10.1073/pnas.2219458120](https://doi.org/10.1073/pnas.2219458120).

- [228] Emanuela Bianchi et al. “Inverse patchy colloids: Synthesis, modeling and self-organization”. In: *Current Opinion in Colloid & Interface Science* 30 (2017), pp. 8–15. ISSN: 1359-0294. DOI: [10.1016/j.cocis.2017.03.010](https://doi.org/10.1016/j.cocis.2017.03.010).
- [229] Pedro Buzón et al. “Virus self-assembly proceeds through contact-rich energy minima”. In: *Science Advances* 7.45 (2021), eabg0811. DOI: [10.1126/sciadv.abg0811](https://doi.org/10.1126/sciadv.abg0811).
- [230] Jianhua Rong et al. “Self-assembly of viral particles”. In: *Current Opinion in Colloid Interface Science* 16.6 (2011), pp. 441–450. ISSN: 1359-0294. DOI: <https://doi.org/10.1016/j.cocis.2011.09.001>.
- [231] Pedro Buzón, Sourav Maity, and Wouter H. Roos. “Physical virology: From virus self-assembly to particle mechanics”. In: *WIREs Nanomedicine and Nanobiotechnology* 12.4 (2020), e1613. DOI: <https://doi.org/10.1002/wnnan.1613>.
- [232] Kai Wu et al. “Systematic construction of progressively larger capsules from a fivefold linking pyrrole-based subcomponent”. In: *Nature Synthesis* (2023), pp. 1–9.
- [233] Wei Li et al. “Encapsulation by Janus spheroids”. In: *Soft Matter* 8.22 (2012), pp. 6027–6032.
- [234] Rees F Garmann, Aaron M Goldfain, and Vinothan N Manoharan. “Measurements of the self-assembly kinetics of individual viral capsids around their RNA genome”. In: *Proceedings of the National Academy of Sciences* 116.45 (2019), pp. 22485–22490.
- [235] Roya Zandi et al. “Origin of icosahedral symmetry in viruses”. In: *Proceedings of the National Academy of Sciences* 101.44 (2004), pp. 15556–15560.

- [236] Vikki Anand Varma et al. “Self Assembly of Patchy Anisotropic Particle Forming Free Standing Monolayer Film”. In: *Adv. Theory Simul.* n/a.n/a (Jan. 2023), p. 2200666. ISSN: 2513-0390. DOI: 10.1002/adts.202200666.
- [237] David Richard, C Patrick Royall, and Thomas Speck. “Communication: Is directed percolation in colloid-polymer mixtures linked to dynamic arrest?” In: *The Journal of Chemical Physics* 148.24 (2018), p. 241101.
- [238] H He and Michael F Thorpe. “Elastic properties of glasses”. In: *Physical Review Letters* 54.19 (1985), p. 2107.
- [239] W.G.T. Kranendonk and D. Frenkel. “Simulation of the adhesive-hard-sphere model”. In: *Molecular Physics* 64.3 (1988), pp. 403–424. DOI: 10.1080/00268978800100303.
- [240] Paul J Steinhardt, David R Nelson, and Marco Ronchetti. “Bond-orientational order in liquids and glasses”. In: *Physical Review B* 28.2 (1983), p. 784.
- [241] Laura Filion et al. “Efficient method for predicting crystal structures at finite temperature: variable box shape simulations”. In: *Physical review letters* 103.18 (2009), p. 188302.
- [242] Yao Li et al. “Topological defects of tetratic liquid-crystal order on a soft spherical surface”. In: *Soft Matter* 9.48 (2013), pp. 11461–11466.
- [243] Athanassios Z Panagiotopoulos et al. “Phase equilibria by simulation in the Gibbs ensemble: alternative derivation, generalization and application to mixture and membrane equilibria”. In: *Molecular Physics* 63.4 (1988), pp. 527–545.
- [244] A. Z. Panagiotopoulos et al. “Phase equilibria by simulation in the Gibbs ensemble”. In: *Molecular Physics* 63.4 (Mar. 1988), pp. 527–545. ISSN: 0026-8976. DOI: 10.1080/00268978800100361.

- [245] Ahyoung Kim et al. “Symmetry-breaking in patch formation on triangular gold nanoparticles by asymmetric polymer grafting”. In: *Nature Communications* 13.1 (2022), p. 6774. ISSN: 2041-1723. DOI: [10.1038/s41467-022-34246-0](https://doi.org/10.1038/s41467-022-34246-0).
- [246] Neil P. King et al. “Accurate design of co-assembling multi-component protein nanomaterials”. In: *Nature* 510.7503 (2014), pp. 103–108. ISSN: 1476-4687. DOI: [10.1038/nature13404](https://doi.org/10.1038/nature13404).
- [247] Giuliana Indelicato, Paolo Cermelli, and Reidun Twarock. “Local rules for the self-assembly of a non-quasi-equivalent viral capsid”. In: *Physical Review E* 105.6 (June 2022), p. 064403. DOI: [10.1103/PhysRevE.105.064403](https://doi.org/10.1103/PhysRevE.105.064403).

Appendix A

List of Publications

Journals

1. "Dynamics and nematic alignment of uniaxial colloids in the presence of obstacles and confinement",
Vikki Anand Varma and Sujin B. Babu Communicated
2. "Breaking the size constraint for nanocages using annular patchy particles",
Vikki Anand Varma, Simmie Jaglan, Mohd. Yasir Khan and Sujin B. Babu
Phys. Chem. Chem. Phys., 26, 138, 2024
3. "Self Assembly of Patchy Anisotropic Particle Forming Free Standing Monolayer Film",
Vikki Anand Varma, Kritika, Jaskaran and Sujin B. Babu *Advanced Theory and Simulations.* 6.3, 2200666, 2023
4. "Enhancement in the diffusivity of Brownian spheroids in the presence of spheres",

Vikki Anand Varma, Isha Malhotra and Sujin B. Babu *Phys. Rev. E* **106**,
014602, 2022

Presentations and proceedings in International/National Conferences

1. "Breaking the size constraint of the nanocages", **Vikki Anand Varma** and Sujin B. Babu Mesoscale modelling of driven disordered materials, CECAM-HQ- EPFL, Lausanne, Switzerland, May- 2023
2. "Self-assembly of patchy spheroids", **Vikki Anand Varma** and Sujin B. Babu 16th Complex Fluids Symposium IIT Kharagpur Dec- 2022
3. "Dynamics in the binary system of spheroids", **Vikki Anand Varma**, Isha Malhotra and Sujin B. Babu 5th International Conference on Soft Materials , Jaipur Dec-2022